THESIS FOR THE DEGREE OF DOCTOR OF PHILOSOPHY IN
THERMO AND FLUID DYNAMICS

Unsteady aerodynamic effects on the driving stability of passenger vehicles

ADAM BRANDT

Department of Mechanics and Maritime Sciences

CHALMERS UNIVERSITY OF TECHNOLOGY

Gothenburg, Sweden 2023

Unsteady aerodynamic effects on the driving stability of passenger vehicles
ADAM BRANDT
ISBN 978-91-7905-805-0

Doktorsavhandlingar vid Chalmers tekniska högskola
Ny serie nr. 5271
ISSN 0346-718X
Department of Mechanics and Maritime Sciences
Chalmers University of Technology
SE-412 96 Gothenburg
Sweden
Telephone: +46 (0)31-772 1000

Chalmers Digitaltryck
Gothenburg, Sweden 2023

Unsteady aerodynamic effects on the driving stability of passenger vehicles
ADAM BRANDT
Department of Mechanics and Maritime Sciences
Chalmers University of Technology

Abstract

The passenger car is a vital part of modern society, giving people the freedom of flexible travel. As technology advances, customers increase their demand for future products. The automotive industry must therefore adapt to society's requirements for energy-efficient travel, where developing low-drag vehicles is key. However, if not designed with care, streamlined bodies of low drag might impair the driving stability. In addition, raised customer demands of perceived control and stability elevate the research needs on driving stability.

Vehicles travelling on open roads are continuously exposed to changing crosswind conditions. Most road vehicles have the aerodynamic centre of pressure located at the front, making them sensitive to these unsteady crosswinds. Strong winds and sensitive vehicle designs degrade the driving stability perceived by drivers and passengers. Furthermore, as aerodynamic loads increase with flow velocity, the sensitivity becomes greater at high speeds. High speeds affect stability performance even without variations in crosswind. The balance of the time-averaged lift forces between the front and rear axles influences understeering and, consequently, vehicle handling. However, the averaged forces cannot always predict the stability performance, which increases the need to explore the unsteady aerodynamic effects on vehicle handling.

The assessment of driving stability for a vehicle in development is often done on test tracks in late design phases when prototype vehicles are available. However, the current demands of faster development times require robust virtual tools for earlier assessment. This thesis aims to develop virtual tools for assessing straight-line driving stability and to gain insights into the interdisciplinary physics between aerodynamics and vehicle dynamics.

By conducting on-track measurements, it was demonstrated that crosswinds deteriorate driving stability and that the vehicle motions of lateral acceleration and yaw velocity correlate with the drivers' subjective assessment. A driving simulator study confirmed these lateral motions, and the path curvature, as significant measures. To reduce the lateral vehicle response to crosswinds, the centre of gravity should move forward, while the aerodynamic yaw moment should be reduced (moving the centre of pressure rearward). For high speed stability, without varying crosswinds, it was demonstrated that the unsteady base wake also plays an important role. Stability issues on the test track correlated with bi-stable wake dynamics, primarily affecting the fluctuating rear lift force. Configurations that stabilised the wake led to subjective improvements on the test track, highlighting the importance of unsteady wake aerodynamics.

Keywords: aerodynamics, vehicle dynamics, driving stability, high speed, wake dynamics, crosswinds

"I'm not superstitious, but I am a little stitious."

-Michael Scott

Acknowledgements

First of all, I would like to thank my supervisors Prof. Simone Sebben and Prof. Bengt Jacobson for all the guidance and support throughout the years, improving the quality of my work. I would also like to thank Ingemar Johansson for his dedication and initialisation of this research project. The project includes colleagues from CEVT (China Euro Vehicle Technology), namely Dr. John Bergström, Jan Hellberg, Dr. Jesper Marklund, Dr. Robert Moestam and Jörgen Sjöström, who have given valuable support and showed great willingness to collaborate interdisciplinarily. To my previous and current managers, who always believed in me and supported me when needed, Erik Preihs and Lars Nilsson – respectfully thank you, respectively.

Much of the experimental work would not have been possible without the kind people at VCC (Volvo Car Corporation) and Hällered Proving Ground, lending me experimental equipment. Next, I would like to thank my colleagues all over CEVT for providing me with support when needed. Special thanks to Samuel Gabriel, Anders Karlsson and Mattias Olander, for their discussions and advice regarding CFD and fluid dynamics.

Furthermore, I want to show appreciation to my former and present colleagues and friends at VEAS for creating an excellent work environment incorporating both valued academic discussions and entertaining activities. I would also like to thank Sonja, for always caring and bringing us together at VEAS.

Last but not least, I want to thank my friends and especially my family for supporting and encouraging me from the start. To Fanny, thank you for always being there and supporting me on this challenging journey.

Adam Brandt
Göteborg, March 2023

Nomenclature

Abbreviations

CAE	Computer-Aided Engineering
CEVT	China Euro Vehicle Technology
CFD	Computational Fluid Dynamics
CoG	Centre of Gravity
CP	Centre of Pressure
DMD	Dynamic Mode Decomposition
DoF	Degree of Freedom
DSM	Dynamic Smagorinsky model (sub-grid scale turbulence)
EPAS	Electronic Power-Assisted Steering
GPS	Global Positioning System
HPG	Hällered Proving Ground
IMU	Inertial Measurement Unit
K&C	Kinematics and Compliance
LES	Large Eddy Simulations
MBD	Multi-Body Dynamic
MRF	Moving Reference Frame
NSP	Neutral Steering Point
PDF	Probability Density Function
PSD	Power Spectral Density
PVT	Volvo Cars aerodynamic wind tunnel
QS	Quasi-Steady (aerodynamic model)
QSD	Quasi-Steady with axle Delay (aerodynamic model)
RANS	Reynolds-Averaged Navier-Stokes
RTK	Real-Time Kinematic
SBES	Stress-Blended Eddy Simulation
SUV	Sports Utility Vehicle
tCFD	Transient CFD (aerodynamic simulation technique)
TI	Turbulence Intensity
VCC	Volvo Car Corporation

Symbols

α	Lateral tyre slip angle	[rad]

β	Vehicle body slip angle	[rad]
Δ	Change	
δ_{SW}	Steering wheel angle	[deg]
δ_f	Front axle steer angle	[rad]
δ_r	Rear axle steer angle	[rad]
λ	Crosswinds length scale	[m]
Ω_x	x-normal vorticity	[1/s]
ω_x	Roll velocity	[deg/s]
ω_y	Pitch velocity	[deg/s]
ω_z	Yaw velocity	[deg/s]
ω_z/v_x	Path trajectory curvature	[1/m]
$\overline{\xi}$	Time-average of ξ	[N.A]
ϕ_z	Global vehicle yaw angle	[rad]
ψ	Relative flow angle	[deg]
ρ	Density of air	[kg/m^3]
St	Stroughal number	[-]
$\vec{\omega}$	Vehicle body angular velocity vector	[deg/s]
$\vec{a}$	Vehicle body acceleration vector	[m/s^2]
$\vec{F}_{aero}$	Aerodynamic loads	[N & Nm]
$\vec{s}$	Vehicle body position relative ground vector	
$\vec{V}$	Relative flow vector	[m/s]
$\vec{w}$	Wind vector	[m/s]
$\vec{z}_t$	Road vertical wheel input vector	[m]
$\xi^{'}$	Fluctuating component of ξ	[N.A]
$\xi_{,rms}$	Root-mean-square of ξ	[N.A]
A	Vehicle frontal area	[m^2]
a_x	Longitudinal acceleration	[m/s^2]
a_y	Lateral acceleration	[m/s^2]
a_z	Vertical acceleration	[m/s^2]
C_{rest}	Aerodynamic coefficients except rear lift	[-]
C_D	Aerodynamic coefficient of drag force	[-]
C_f	Front axle lateral tyre cornering stiffness	[N/rad]
C_{lf}	Aerodynamic coefficient of front lift force	[-]
C_{lr}	Aerodynamic coefficient of rear lift force	[-]
C_p	Aerodynamic pressure coefficient	[-]

C_r	Rear axle lateral tyre cornering stiffness	[N/rad]
C_S	Aerodynamic coefficient of side force	[-]
$C^{norm}_{v'_x v'_x}$	Two-point correlation coefficient	[-]
C_{ym}	Aerodynamic yaw moment coefficient	[-]
C_y	Lateral tyre cornering stiffness	[N/rad]
d_{fRC}	Front axle roll damping	[Nm/(deg/s)]
d_{rRC}	Rear axle roll damping	[Nm/(deg/s)]
f	Frequency	[Hz]
F_D	Aerodynamic drag force	[N]
F_{flz}	Front left normal tyre force	[N]
F_{frz}	Front right normal tyre force	[N]
F_{fyw}	Front axle lateral tyre force	[N]
F_L	Aerodynamic lift force	[N]
F_{rlz}	Rear left normal tyre force	[N]
F_{rrz}	Rear right normal tyre force	[N]
F_{ryw}	Rear axle lateral tyre force	[N]
F_{sf}	Aerodynamic front axle side force	[N]
F_{sr}	Aerodynamic rear axle side force	[N]
F_S	Aerodynamic side force	[N]
F_{yt}	Lateral tyre forces	[N]
h	Centre of gravity height	[m]
h_{fRC}	Front axle roll centre height	[m]
h_{rRC}	Rear axle roll centre height	[m]
J_s	Vehicle sprung mass moment of roll inertia	[kgm^2]
J_z	Vehicle mass moment of yaw inertia	[kgm^2]
K	Reduced frequency	[-]
$K_1 = \frac{1}{2}\rho A$	Constant for simplification	[kg/m]
K_2	Aerodynamic side force coefficient gradient	[1/deg]
k_{fRC}	Front axle roll stiffness	[N/deg]
k_{rRC}	Rear axle roll stiffness	[N/deg]
L	Wheel base	[m]
l	Vehicle length	[m]
l_{CP}	Distance between mid-axle reference and CP	[m]
l_{NSP}	Distance between mid-axle reference and NSP	[m]
l_f	Distance between CoG and front axle	[m]

l_r	Distance between CoG and rear axle	[m]
l_s	Distance between CoG and NSP	[m]
m	Vehicle mass	[kg]
M_x	Aerodynamic roll moment (ref. at ground mid-axles)	[Nm]
M_y	Aerodynamic pitch moment (ref. at ground mid-axles)	[Nm]
M_z	Aerodynamic yaw moment (ref. at ground mid-axles)	[Nm]
t	Time	[s]
t_0	Gust start time	[s]
t_{gust}	Gust duration	[s]
T_{SW}	Steering wheel torque	[Nm]
t_b	Gust build-up time	[s]
t_d	Gust drop time	[s]
t_p	Gust pause time	[s]
u	Flow velocity	[m/s]
V_∞	Freestream velocity	[m/s]
V_{mag}	Relative flow magnitude	[m/s]
v_v	Vehicle motion vector	[m/s]
v_x	Vehicle longitudinal velocity	[m/s]
W	Track width	[m]
w_x	Longitudinal wind component	[m/s]
w_y	Crosswind component	[m/s]
w_y^{end}	Gust end amplitude	[m/s]
w_y^{max}	Gust maximum amplitude	[m/s]
w_y^{min}	Gust minimum amplitude	[m/s]
w_y^{start}	Gust start amplitude	[m/s]
x	Longitudinal distance	[m]
Y	Combined proxy measure for crosswind sensitivity	
y	Lateral distance	[m]
y^+	Non-dimensional wall distance	[-]
z	Vertical distance	[m]

Definitions

High speed	>100 km/h

Thesis

This thesis consists of an extended summary and the following appended papers:

Paper A Brandt, A., Sebben, S., Jacobson, B., Preihs, E., and Johansson, I. "Quantitative High Speed Stability Assessment of a Sports Utility Vehicle and Classification of Wind Gust Profiles". *SAE Technical Paper Series*. 2020. DOI: 10.4271/2020-01-0677

Paper B Brandt, A., Jacobson, B., and Sebben, S. "High speed driving stability of road vehicles under crosswinds: an aerodynamic and vehicle dynamic parametric sensitivity analysis". *Vehicle System Dynamics* **60**.7 (2021), 1–24. DOI: 10.1080/00423114.2021.1903516

Paper C Brandt, A., Sebben, S., and Jacobson, B. "Base wake dynamics and its influence on driving stability of passenger vehicles in crosswind". *Journal of Wind Engineering and Industrial Aerodynamics* **230** (2022). DOI: 10.1016/j.jweia.2022.105164

Paper D Brandt, A., Sebben, S., and Jacobson, B. "Wake dynamics of passenger vehicles and its influence on high speed stability". *Submitted for Publication* (2023)

Paper E Brandt, A., Jacobson, B., and Sebben, S. "Drivers' perceived sensitivity to crosswinds and to low-frequency aerodynamic lift fluctuations". *Accepted for SAE WCX Conference*. 2023

Patent application by the author:

Brandt A. and Bergström J., "A spoiler arrangement for controlling the aerodynamic wake after a driving vehicle", Zhejiang Geely Holding Group Co., Ltd.,
European Patent 23158709.8 (filing date: February 27, 2023)

Division of work

A All instrumentation setup, data acquisition and analysis for Paper A was done by Brandt. The high speed driving at the test track was performed by Brandt and two professional test drivers. The first manuscript was written by Brandt and then discussed, reviewed and revised by all authors.

B The aerodynamic simulations and quasi-steady modelling were performed by Brandt. The vehicle dynamic reference model (high-fidelity) was created by the Vehicle Dynamics CAE team at CEVT. Brandt constructed the low- and mid-fidelity models, performed the coupled simulations and constructed the parametric sensitivity study. The first manuscript was written by Brandt and then discussed, reviewed and revised by all authors.

C The unsteady aerodynamic simulations and the coupled vehicle dynamic analyses were performed by Brandt. The first manuscript was written by Brandt and then discussed, reviewed and revised by all authors.

D Brandt designed the three diffusers and the three side spoilers used in the numerical analysis. The out-washed side spoiler was manufactured by Prototal GTP. The test track evaluations were performed by Brandt and one professional test driver. Brandt performed the wind tunnel experiments with the help of Josefsson and Marklund. The first manuscript was written by Brandt and then discussed, reviewed and revised by all authors.

E The driving simulator study on crosswind gusts was conducted by Mohankumar and Sawanth, under the supervision of Brandt. Brandt performed the data analysis and conducted the high speed stability study in the driving simulator. The first manuscript was written by Brandt and then discussed, reviewed and revised by all authors.

Contents

Part I

Extended summary

1

Introduction[1]

This thesis is focused on the stability of passenger vehicles during high speed driving. The work is interdisciplinary, focusing on the aerodynamic and vehicle dynamic performance related to driving stability.

The passenger car has become a vital part of modern society over the last century. Its flexibility enables decentralised transportation for a large part of the population, seen as a freedom by many. As technology advances, customers acclimatise to modern solutions and increase their demands for future products. The automotive industry must therefore adapt to the new customer and societal demands. Today, society requires more energy-efficient travel to reduce the transport sector's negative environmental impact. For this, developing vehicles with low aerodynamic drag is key. However, low drag streamlined bodies with balanced base wakes might impair the driving stability, if not designed with care. This, coupled with the increasing customer demands for perceived control and stability has increased research needs on aerodynamic and vehicle dynamic driving stability.

Vehicles having issues with driving stability are often described as *nervous* by drivers. When driving on the highway, this will force the driver to correct the vehicle to remain in the lane. If this becomes difficult or is required too often, it classifies as a significant driving stability issue. In contrary, vehicles with excellent driving stability performance will not require any corrections and are perceived as stable even in crosswind conditions. This thesis focuses on *straight-line driving stability* at high speeds (>100 km/h), as increased vehicle speed tends to deteriorate the stability performance. A subtopic of straight-line driving stability is *crosswind sensitivity*, where the stability performance related to crosswind gusts is assessed. Another subtopic discussed in this work is *high speed stability*. High speed stability defines self-induced aerodynamic and/or vehicle dynamic driving stability effects. These effects may exist in (but are not limited to) yawed flow conditions. Both subtopics of straight-line driving stability will be discussed in the thesis.

When developing a passenger vehicle, the evaluation of straight-line driving stability at high speeds is often done subjectively using prototypes. Unfortunately, prototype vehicles are only available at late stages in the development process, and changes in these phases are costly and hard to implement. Issues with driving stability are therefore difficult to deal with and require balanced compromises with other vehicle attributes. A way to resolve this would be to move the assessment from the on-track testing to virtual testing, using numerical tools. A virtual

[1]Parts of this thesis have been carried over from the Licentiate thesis [6]

assessment of driving stability can be used in early design phases, enabling improvements when the cost of change is lower and removing most issues before the prototype vehicles are built. Still, it is foreseen that the final evaluations will be performed on the test tracks.

1.1 Research objectives

This research project aims to increase the knowledge on driving stability performance of passenger vehicles and to understand how virtual simulation tools can be used to develop more stable vehicles. Three research questions have been formulated for the project:

1. How do vehicle dynamics, vehicle aerodynamics and their coupled effect influence vehicle straight-line driving stability at high speeds?
2. What quantities can objectively rate the vehicle straight-line driving stability, and how can they be considered in the development process?
3. Which virtual methods can be used to develop and evaluate the straight-line driving stability performance of a passenger vehicle?

The first question aims at understanding the interdisciplinary physics, while the second focuses on setting better engineering requirements to prevent issues with driving stability. The last question elaborates on how to move the assessment of driving stability from the road to the virtual environment using simulation tools.

1.2 Limitations

- Only one vehicle has been used as a research object in this thesis. The vehicle details are described in Section 3.1.
- The research on subjective perception only focused on the driver, and not the passengers.
- The influence of traffic and overtaking aerodynamics on driving stability has not been studied.

1.3 Outline

Chapter 1 provided the context of driving stability and stated the objectives and limitations of the research project. Chapter 2 covers relevant background and theory, particularly on realistic on-road wind conditions, crosswinds aerodynamics, wake aerodynamics and straight-line vehicle dynamic handling. Chapter 3 presents the methodology used in the appended papers. Chapters 4 and 5 discuss the most relevant results related to crosswind sensitivity and high speed stability, respectively. Chapter 6 gives some concluding remarks and outlook into possible future work, followed by a summary of the appended papers in Chapter 7.

An overview of the papers included in this thesis is given in Figure 1.1. The two subtopics of straight-line driving stability (crosswind sensitivity and high speed stability) are shown with the experimental and numerical methodologies used. The arrows indicate the knowledge flow gained throughout the project and applied to the subsequent papers.

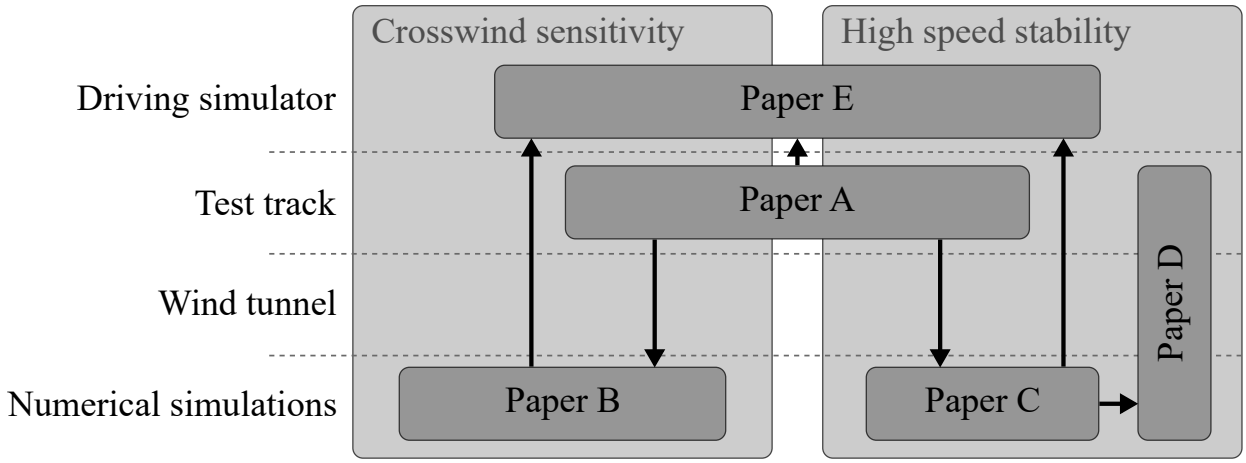

Figure 1.1: *The paper contents and knowledge flow (indicated by arrows) for the research conducted on the subtopics of crosswind sensitivity and high speed stability using numerical simulations and experimental work in a driving simulator, on a test track and in a wind tunnel.*

2

Background

Driving stability at high speeds is an interdisciplinary topic. A system overview and is presented in Figure 2.1 together with the aerodynamic [7] (red) and vehicle dynamic (blue) [8] coordinate systems used in this work. The on-road environment affects the system via wind and road unevenness (traffic effects are disregarded). The horizontal wind components (w_x and w_y) together with the vehicle velocity and body slip (v_x and β) form the flow velocity and angle (V_{mag} and ψ) relative to the travelling vehicle. In turn, aerodynamic forces and moments ($\vec{F}_{aero}$) affect the vehicle dynamic response ($\vec{a}$ and $\vec{\omega}$) which influence the driver's steering reaction (δ_{SW} or T_{SW}) and subjective assessment. This overview visualises the complexity of the system and guides the reader to the different formulations of the problems discussed in the thesis.

This chapter describes typical on-road flow conditions in contrast to the controlled test environment in wind tunnels. The physics of the dynamic system is then introduced, focusing on straight-line handling, crosswind aerodynamics and vertical aerodynamics, continued by a review of previous work related to unsteady wake aerodynamics. Finally, a background on driver behaviour and subjective assessment during straight-line handling is given.

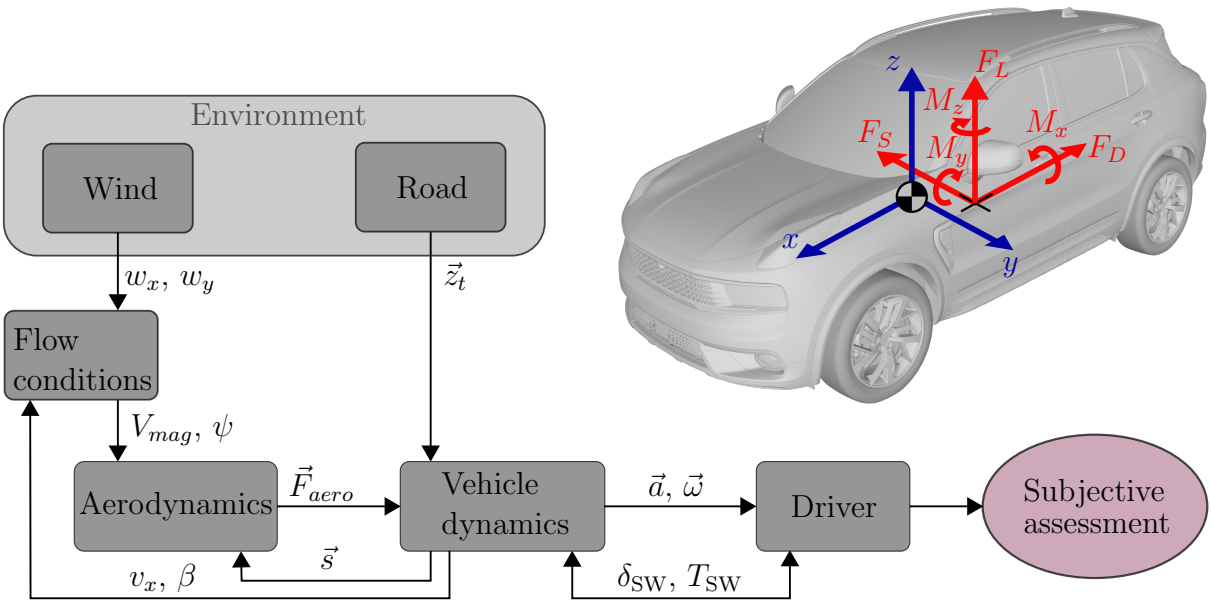

Figure 2.1: *An systematic overview of driving stability, along with the aerodynamic (red) and vehicle dynamic (blue) coordinate systems.*

2.1 On-road wind conditions

Crosswind disturbances are, in principle, always present on open roads and extreme crosswinds have even been shown to increase road accidents [9]. A review by Sims-Williams [10] highlighted that the unsteady flow conditions are caused by the turbulence in the natural wind, flow disturbances by other vehicles and obstacles at the roadside. These flow disturbances are formulated below in Equation 2.1 [10].

$$\frac{d\vec{V}}{dt} = \frac{\partial v_x}{\partial t} + \frac{\partial \vec{w}}{\partial t} + v_x \frac{\partial \vec{w}}{\partial x} \tag{2.1}$$

The left-hand side of Equation 2.1 shows the flow transients locally at the vehicle. The right-hand side contains three terms representing the vehicle acceleration, the changing wind conditions (in time) and the flow variation from driving into different wind conditions along the road (Figure 2.2). Sims-Williams [10] argued that the last term is the most influential for a travelling vehicle, meaning that most crosswind gusts originate from driving into different wind conditions ($v_x \frac{\partial \vec{w}}{\partial x}$) rather than local variations in the wind ($\frac{\partial \vec{w}}{\partial t}$).

The gustiness of the flow is often quantified as turbulence intensity, TI, which is a standard deviation measure using the root-mean-square of the flow fluctuations, $u^{'}$, and the mean velocity, $\overline{u}$, as in,

$$TI = \frac{u^{'}}{\overline{u}}. \tag{2.2}$$

The turbulence intensity can differ drastically between the controlled environment of traditional wind tunnels ($TI < 1\,\%$) and the highway traffic which can be up to $TI = 15\,\%$ [11, 12]. Watkins and Cooper [13, 14] presented work on the effects of the atmospheric boundary layer turbulence for road vehicles, based on the theoretical groundwork of wind engineering. Their experimental data showed good agreement with the von Karman spectrum of homogeneous, isotropic turbulence. The majority of the driving occurred in the turbulence intensity range of 2 % to 10 % [14, 15]. The effects of turbulence intensity have further been studied using

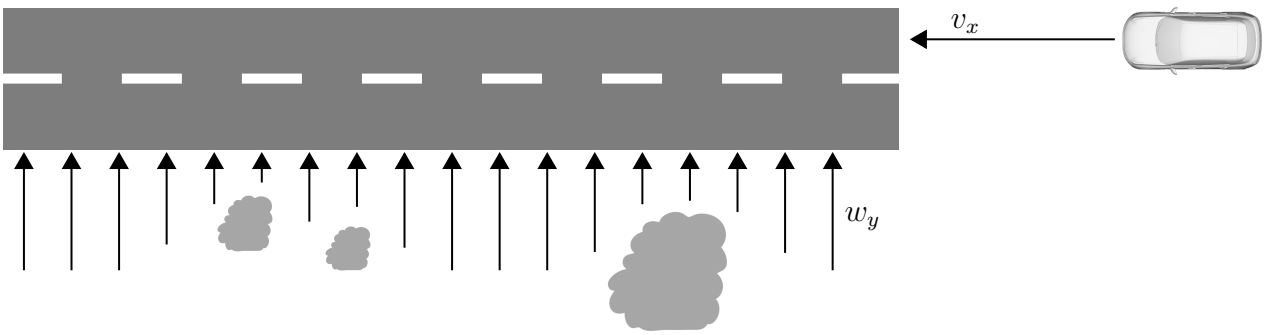

Figure 2.2: *Illustration of the unsteady flow disturbances experienced by a travelling vehicle in temporally steady wind, without traffic (inspired by [10]).*

transient wind tunnels [16, 17] and a review showed that the turbulence intensity could alter the optimum design of the backlight angle of a vehicle [13]. Moreover, the literature review by Sims-Williams [10] concluded that crosswind scales of 2-20 vehicle lengths are the most critical for vehicle stability, since there is a significant amount of road spectral energy at these scales and that the vehicle motion response frequencies can not be considered quasi-steady.

Traditional wind tunnels, originating from aerospace engineering, were intentionally designed with low turbulence intensity to increase the experiments' reproducibility. Similarly, to increase the reproducibility of on-road crosswind experiments, test track facilities with fans to control the external crosswind conditions have been used [18–22]. To standardise experiments at these facilities, the International Standard ISO 12021:2010 [23] was formulated. The guidelines in the ISO 12021:2010 standard include a methodology where a vehicle is driven at 100 km/h into a zone of 20 m/s crosswind, resulting in a flow angle of $\psi = 35.8$ deg. The resulting crosswind gust profile has been adopted in several numerical studies of crosswind sensitivity [24–28]. These extreme winds of 20 m/s create high aerodynamic forces and a distinct motion response of the vehicle, helpful in measuring differences between vehicles and configurations. However, it has also been shown that these crosswinds are too extreme to represent most real driving scenarios [1, 11, 12, 14, 29–31], and are more likely investigations of extreme crosswind sensitivity, rather than driving stability performance at high speeds. For example, when conducting on-road measurements of crosswind gusts in Germany, Theissen and Wojciak [29, 30] found that the typical magnitude of the crosswind resulted in flow angles of ± 10 deg. Similar results were found by Jessing et al. [15] and Lawson et al. [32].

Wojciak [29] focused on aerodynamics during crosswind gusts. The first part of [29] focused on quantifying the crosswind gust profiles using a probe setup similar to Wordley and Saunders [11]. Wojciak measured the flow conditions during 163 gust events and classified the crosswinds into three different gust profiles. It was also noted that 72 % of the gust events had a zero crossing of the relative incoming flow angle, which was found to have a significant impact on the aerodynamic response to the crosswind by Theissen [30]. Furthermore, Wojciak showed that most of the gust events had peak values of the incoming flow angle of 5 to 9 deg, at a vehicle velocity of 140 km/h.

2.2 Road vehicle dynamics

The overview of the system (Figure 2.1) demonstrates the interdisciplinary physics applied in this thesis. This section introduces the physics of the dynamic system, starting with a description of the theory and previous work on vehicle dynamic straight-line handling. After that, the essential aspects of crosswind aerodynamics and vertical aerodynamics are established.

2.2.1 Vehicle dynamic straight-line handling

The lateral tyre forces, F_{yt}, determine the road plane dynamics of the vehicle. Lateral tyre forces are generated when the angle of the wheel differs from its velocity vector. This differing angle (the lateral tyre slip angle, α) is small during normal driving, but can generate high forces depending on the cornering stiffness, C_y. ISO 8855:2011 [8] defines cornering stiffness as,

$$C_y = -\frac{\partial F_{yt}}{\partial \alpha}\bigg|_{\alpha=0}. \tag{2.3}$$

Hence, the lateral slip angle multiplied by the cornering stiffness of the tyre defines the generated lateral tyre force. Furthermore, the cornering stiffness can be defined for each axle (C_f and C_r) and it should be noted that it is not constant, as it is affected by the normal load and other varying driving conditions. The balance between front and rear axle cornering stiffness determines how the vehicle rotates (yaw) when a lateral force is applied, e.g. centrifugal force or aerodynamic side force, F_S. At some longitudinal position along the vehicle, the lateral force will not rotate the vehicle in any direction. This can be described as a *cornering stiffness centre* or a neutral steering point (NSP). Figure 2.3 visualises the NSP along with the aerodynamic centre of pressure (CP), the centre of gravity (CoG) and a geometric reference point midway between the axles. If the NSP is behind the CoG, the centrifugal force will understeer the vehicle in a steady-state cornering scenario. The distance between CoG and NSP, l_s, (Equation 2.4) is, therefore, a measure of understeering. However, since the cornering stiffness varies during driving, l_s will also vary.

$$l_s = \frac{C_r l_r - C_f l_f}{C_f + C_r} \tag{2.4}$$

By defining the NSP with respect to the fixed geometric reference point, it can be observed that the NSP is not directly dependent on the CoG positioning (l_f or l_r), see the derivation in Equation 2.5. It only depends on the axle cornering stiffness balance and the wheel base.

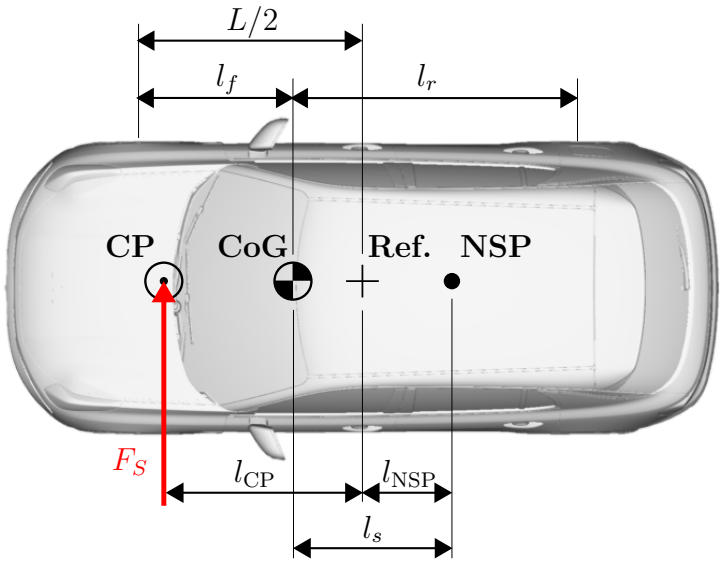

Figure 2.3: *Top view of a vehicle visualising the typical longitudinal positions of the aerodynamic centre of pressure (CP), the centre of gravity (CoG), a geometric reference point between the axles (Ref.) and the neutral steering point (NSP).*

$$l_{\text{NSP}} = l_s - \left(\frac{L}{2} - l_f\right) = \frac{C_r l_r - C_f l_f}{C_f + C_r} + \frac{l_f - l_r}{2} = \frac{C_r - C_f}{C_f + C_r}\frac{L}{2} \tag{2.5}$$

Aerodynamic centre of pressure

Figure 2.3 present the centre of pressure (CP) in front of the NSP. This is typical for a regular passenger vehicle. However, this also implies that the vehicle is *aerodynamically unstable* (any crosswind would work to rotate the vehicle away from the wind, increasing the relative flow angle). Early work on straight-line handling concluded that CP should be located behind CoG (later corrected to behind NSP) [18, 33]. In 1965, Barth [34] suggested stabilising fins at the rear to improve stability of the vehicle by moving CP rearwards towards CoG and NSP. Nevertheless, that might not be a realistic solution. Even though the vehicle is aerodynamically unstable, the complete vehicle dynamic system can remain stable due to the road contact. Favre et al. [35] conducted a numerical study in which CP, CoG and NSP were altered independently (the NSP position was altered by varying the cornering stiffness, to decouple its influence from the CoG position). As expected, CP should be moved rearward to reduce crosswind sensitivity, primarily to decrease the distance to NSP, and NSP should be located behind CoG [35].

The aerodynamic forces and moments are often defined at the reference point between the axles [7]. The aerodynamic yaw moment can thus be defined as $M_z = F_S l_{\text{CP}}$. The distance between CP and the reference, l_{CP}, will also vary since the aerodynamic side force, F_S, and yaw moment, M_z, are not strictly linearly dependent. In summary, Figure 2.3 give valuable insights on straight-line handling. Although, as stated above, the positions of NSP and CP move depending on the driving scenario and wind load.

Vertical aerodynamics

The normal loads affect the cornering stiffness as a digressive function [36]. Therefore, the aerodynamic lift forces at the front and rear axle will affect the cornering stiffness and thus the driving dynamics at high speed. Milliken et al. [37] introduced a static stability, based on a bicycle model with the tyre cornering stiffness linearised at the static normal loads. Negative index values were defined as stable. The index value increased with vehicle velocity, which is consistent with the decrease in yaw damping at higher velocities. The stability index has been used in parametric studies, showing that a positive lift balance ($C_{lf} - C_{lr}$) increases vehicle stability [38]. This corresponds to decreasing the cornering stiffness at the front axle and increasing it at the rear, moving the NSP further rearward according to Equation 2.5. Using a similar approach by calculating the eigenvalues of the linear system of the bicycle model, taking into account the aerodynamic lift forces through the cornering stiffness, results in Figure 2.4. The figure shows the contours of the real eigenvalues at 180 km/h, where negative eigenvalues define a stable linear system. Increasing the lift balance ($C_{lf} - C_{lr}$) creates a more stable vehicle, as for the stability index. In addition, the figure defines a shaded region where aerodynamic lift forces cause positive real eigenvalues and hence an unstable linear system. Although this limit is realistically never reached, the two approaches explain the effect of vertical aerodynamics on straight-line driving stability. Howell and Le Good [39, 40] conducted subjective on-road experiments, where test drivers evaluated the high speed stability performance of several vehicles with different lift coefficients. The improvement in stability performance with positive lift balance was confirmed [39].

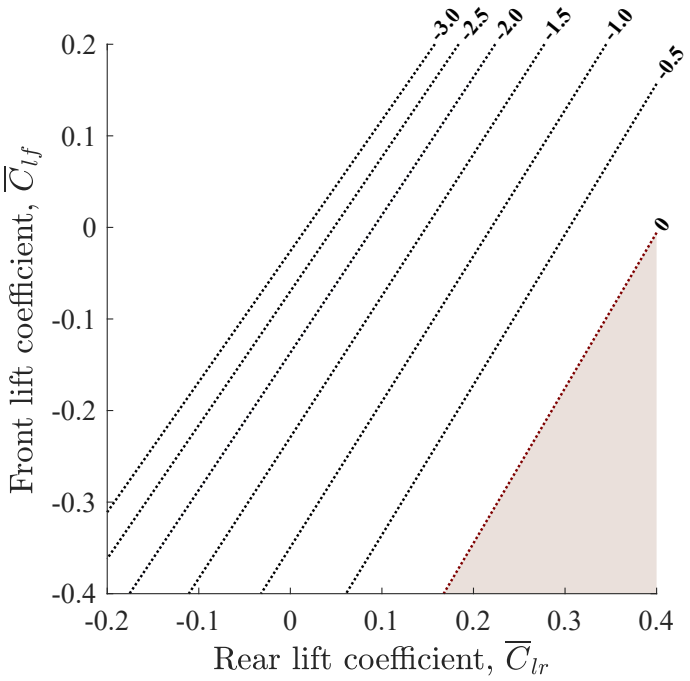

Figure 2.4: *The largest of the real eigenvalues of the linearised bicycle model, at* 180 km/h *driving speed, where the shaded region defines an unstable linear system.*

Vehicle dynamic parameters

The static stability index was further used to highlight important vehicle dynamic properties. It was found beneficial to decrease the yaw mass moment of inertia and especially to move CoG forward, increasing the vehicle understeer [38]. This was also established by MacAdam et al. [18] and later in other studies [28, 41, 42]. MacAdam et al. also showed the advantage of moving CP rearward (according to the theory above) and the benefit of increased roll stiffness. Wheel alignments, especially the toe angles, are known to affect high speed stability performance. Using toe-in at the rear axle increases understeering and reduces vehicle yaw sensitivity and nervousness.

2.2.2 Crosswind aerodynamics

The background and theory on crosswind aerodynamics will first cover constant crosswinds followed by transient crosswind conditions.

Constant crosswinds

Perpendicular crosswinds, w_y, induce flow angles, ψ, relative to the direction of the vehicle, see Figure 2.5. The relative flow from the vehicle velocity, v_x, and wind components, w_x and w_y, affect the resulting flow angle and magnitude, V_{mag}, as in,

$$V_{\text{mag}} = \sqrt{(v_x + w_x)^2 + w_y^2}, \qquad \psi = \arctan\left(\frac{w_y}{v_x + w_x}\right). \tag{2.6}$$

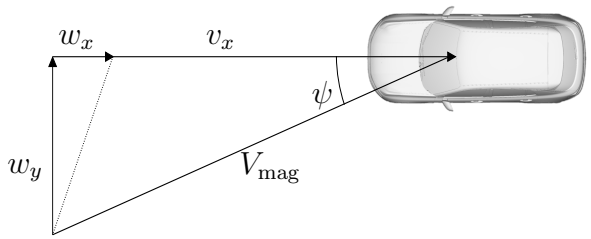

Figure 2.5: *Schematics of how the flow angle, ψ, and flow velocity, V_{mag}, relate to the vehicle velocity, v_x, and horizontal wind components, w_x and w_y.*

The aerodynamic forces and moments are determined by the magnitude and angle of the flow. As the vehicle goes faster, the flow angle decreases. Nevertheless, the aerodynamic forces and moments will increase at higher velocities. As shown in Equation 2.7, the aerodynamic side force, F_S, increases with the square of the flow velocity, V_{mag}.

$$F_S = \frac{1}{2}\rho A C_S(\psi) V_{\text{mag}}^2 = K_1 C_S(\psi) V_{\text{mag}}^2 \tag{2.7}$$

The density of air, ρ, and frontal area, A, can be set (together with the half) to the constant K_1 to simplify the expression. The coefficient of side force, C_S, is a function of the incoming flow angle, ψ. So, the quadratic increase in forces and moments with flow velocity holds for a constant flow angle. However, as the flow angle decreases with increasing vehicle velocity, a more realistic setting for high speed driving is to keep the crosswind velocity, w_y, constant. In this scenario, without head- or tail wind ($w_x = 0$), the flow angle decreases approximately linear with the vehicle velocity. The first approximation in Equation 2.8, that the side force coefficient is directly proportional to the flow angle, was observed for multiple vehicle models in the study by Howell and Panigrahi [43]. This linearisation is presented using a constant, K_2. The second approximation of small angles, together with the assumption of Reynolds number independent aerodynamic coefficients, implies that the vehicle velocity is high, e.g. above 100 km/h, which is in the range of interest for high speed driving stability.

$$C_S(\psi) \approx K_2\psi = K_2 \arctan\left(\frac{w_y}{v_x}\right) \approx K_2\frac{w_y}{v_x} \tag{2.8}$$

The resulting expression of the side force in Equation 2.9 shows an approximately linear increase with vehicle velocity and crosswind velocity. Hence, doubling the driving speed will almost double the side force, even though the crosswind velocity is kept constant, see Figure 2.6.

$$\Rightarrow F_S = K_1 K_2 w_y \left(v_x + \frac{w_y^2}{v_x}\right) \tag{2.9}$$

The same approximations can be made for the aerodynamic yaw moment, C_{ym}, (or any aerodynamic coefficient with a linear dependency on the flow angle). In summary, this

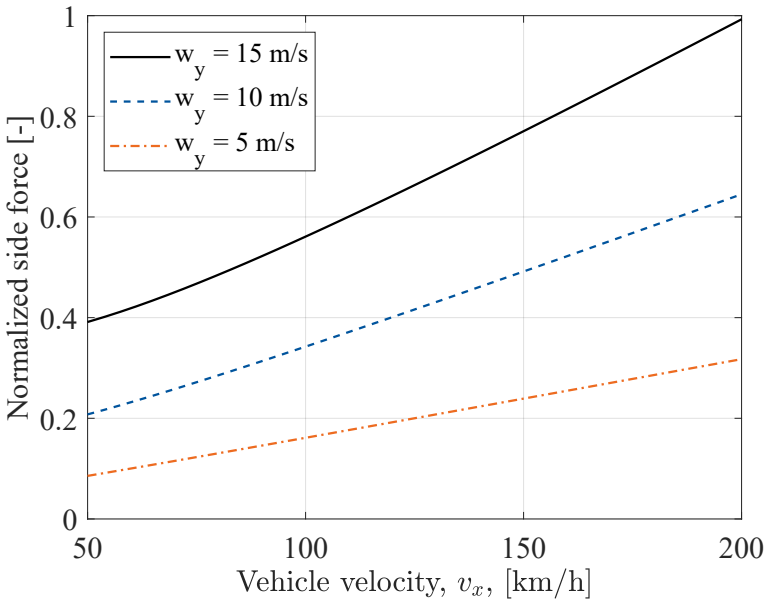

Figure 2.6: *The side force increase with vehicle velocity, v_x, and crosswind velocity, w_y, based on Equation 2.9. Normalised with the side force at* 200 km/h *and* $w_y = 15$ m/s.

simplified example shows that the increase in aerodynamic side force and yaw moment occur simultaneously as the yaw damping of the vehicle decreases with increasing speed, making the vehicle more crosswind sensitive at high speeds. These two facts exemplify why high vehicle velocities affect the stability performance of a road vehicle.

Transient crosswinds

So far, this section has discussed aerodynamics in constant crosswinds. However, that is a rare on-road condition, as mentioned in Section 2.1. Time-dependent, *transient*, crosswind conditions intensify the challenges with driving stability. Chadwick et al. [44] experimentally showed high overshoots in the aerodynamic yaw moment when exciting both a sharp-edged and a radiused-edged box to transient crosswinds. Similar results were presented by Theissen [30], where the overshoots in the yaw moment were explained by the delay in flow angle between the front and rear of the vehicle, when driving into crosswinds. Bell et al. [22] highlighted an additional effect for the overshoots as the pressure development is slower on the leeward side in strong crosswinds. These effects could not be captured in a quasi-steady aerodynamic model, where the aerodynamic coefficients obtained at constant crosswinds are used.

The early work on classifying wind conditions was based on wind loading for structures, such as buildings, where an aerodynamic admittance function was used [45]. The aerodynamic admittance (transfer function) describes how the dynamic overshoots of the forces and moments are affected by the frequency of the crosswind flow, compared to the steady crosswind forces [46]. The non-dimensional Strouhal number is often used when analysing oscillating flows. The frequency, f, of the flow is non-dimensionalised by a characteristic length, l, and the freestream velocity, V_∞, see Equation 2.10. Stoll and Wiedemann [47] investigated the DrivAer notchback's aerodynamic side force and yaw moment admittance using a transient crosswind wind tunnel setup and two simulation methodologies. The results showed a side force admittance close to unity (quasi-steady) before a drop-off at St = 0.15. On the contrary, the yaw moment

admittance showed an increase up until St = 0.15 and thereafter a decrease.

$$\mathrm{St} = \frac{fl}{V_\infty} \tag{2.10}$$

$$\mathrm{K} = \frac{2\pi fl}{V_\infty} = 2\pi\mathrm{St} \tag{2.11}$$

Another quantity related to the Strouhal number is the reduced frequency [10], see Equation 2.11. A rule-of-thumb associated with this quantity is steady-state crosswind aerodynamics at $K = 0$, quasi-steady when $K < 0.1$ and unsteady when $K > 1.0$ [10]. Note, that the range $K = 0.1-1.0$ is neither classified as quasi-steady nor unsteady. The spectral energy flow cascade can be seen in Figure 2.7, depending on crosswind frequencies at 160 km/h and corresponding St, K and λ/l values. For reference: the critical crosswind scale region of 2-20 vehicle lengths, λ/l, corresponds to $K = 3.1 - 0.3$, respectively. However, it is important to note that this is a rule of thumb. For example, Fuller and Passmore [48] found transient flow effects originating from a-pillar separation of a 1/6 scale Davis model at a reduced frequency of 0.098 (quasi-steady). On the other hand, Oettle et al. [49] found that the side window surface pressure develops quickly at crosswind changes and that it could be accurately approximated using a quasi-steady model up to $K = 1.0$.

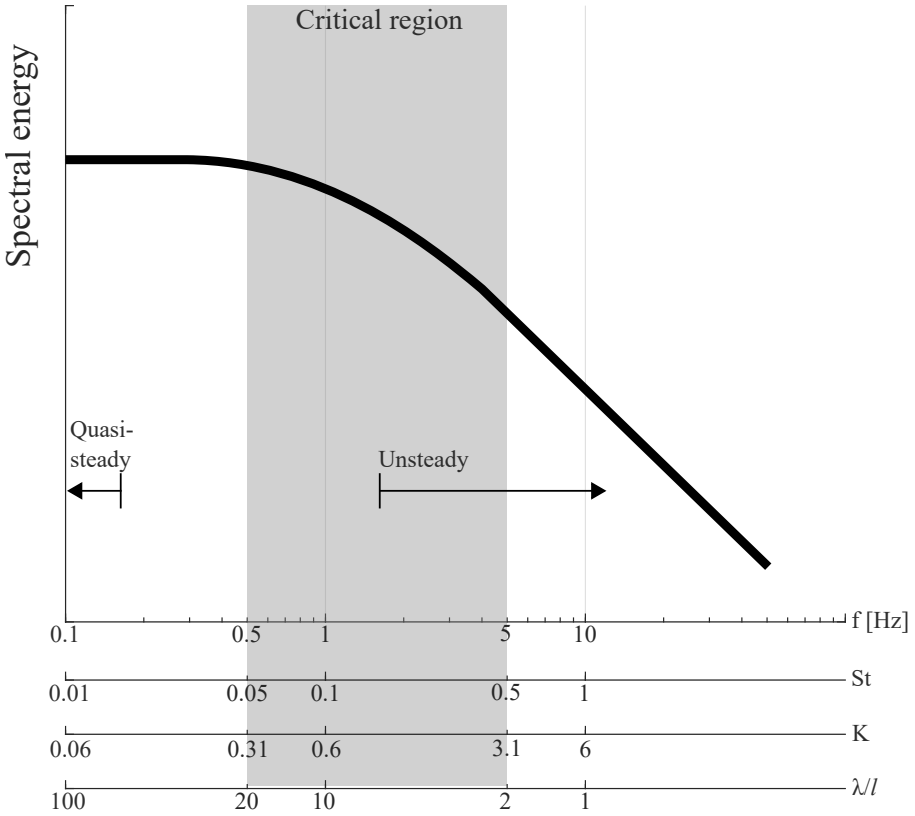

Figure 2.7: *The spectral energy of the crosswind flow and relevant scales for driving stability, at* 160 km/h *(inspired by [10] and [29]).*

2.3 Wake aerodynamics

Crosswind aerodynamics aid the understanding of the vehicle sensitivity to gusts and the averaged lift forces can be used as guidelines for high speed stability performance. However, small changes in time-averaged lift forces can have a more significant effect on the high speed stability performance than what can be solely explained by the change in cornering stiffness. This indicates that important information is lost when disregarding the transient aerodynamic forces. Okada et al. [50] showed correlations between transient aerodynamic flow structures above the trunk deck of a sedan and its on-road subjective assessment. The flow structures were shown to affect the aerodynamic pitching and could be reduced by modifications to the A- and C-pillars [51–53]. Kawakami et al. [54] correlated the subjective assessment to the roll and yaw moment fluctuations and showed that the fluctuations could be reduced by using a roof-side spoiler design and delta-winglet vortex generators mounted on the sides at the rear of the vehicle. The vortex generators were evaluated subjectively on a test vehicle, where improvements in driving stability were noted. A numerical study used a methodology based on DMD (dynamic mode decomposition) to find geometrical improvements to reduce fluctuations in pitching moment at 1.2 Hz [55], a problematic frequency since it lies close to the pitching mode of the suspension system in a typical passenger vehicle ($\approx 1.0 - 1.5$ Hz). The fluctuations were successfully reduced by adding new design solutions at the rear-side spoiler, under the vehicle and at the front wheels. These studies indicate that aerodynamic load fluctuations influence vehicle stability performance and that clever design solutions can reduce these fluctuations.

The aerodynamic load fluctuations on a bluff body, such as a passenger vehicle, are mainly determined by the dynamics of the wake aft the body. Large unsteady wake motions will result in significant load fluctuations. Furthermore, the shape of the wake can indicate some aerodynamic characteristics of the vehicle, such as a higher rear lift for a down-wash dominated wake versus an up-wash dominated wake. Urquhart et al. [56] found that optimising the roof and side angles for low drag on a simplified vehicle geometry (Windsor model) resulted in a vertically balanced wake that is neither up-wash nor down-wash dominated. Interestingly, simplified geometries, such as the Windsor and Ahmed body, with presumably balanced wakes, have been shown to have bi-stable wake dynamics, where the wake randomly switches between two asymmetrical but mirrored states [57, 58]. The aspect ratio of the vehicle base determines the orientation of the bi-stability, where the wake state switches from left to right for a broad base and top to bottom for a tall base [57], also referred to as symmetry breaking modes [59]. Nonetheless, these effects were quite sensitive since they disappeared when subjecting the models to slight crosswind flows [60, 61]. However, Meile et al. [62] and later [63, 64] showed that vertical wake bi-stability could occur in crosswind conditions when adding a slanted rear windscreen angle of 35 deg to the Ahmed body. For this geometry, the bi-stability only occurred at certain crosswind conditions [62–64]. This led to the reasoning that real detailed passenger vehicles with slanted rear windscreen angles could exhibit wake bi-stabilities in crosswinds, which was confirmed in a study by Bonnavion et al. [65] investigating a hatchback vehicle. Similarly, this vehicle geometry only exhibited the vertical switching between wake states in a specific range of the relative flow angle. The wake data difference between the states was not as evident as for the simplified bodies, yet two statistically preferred vertical base pressure gradient states were found. The two states were predominantly determined by an

either attached or detached flow over the rear windscreen in these crosswind conditions [65]. Vertical wake multi-stabilities have also been found in studies on light vans [59, 65, 66].

2.4 Driver behaviour and subjective assessment

When driving on the highway, the driver will correct the vehicle from any lane deviations using the steering. If this becomes difficult or is required too often, it classifies as an issue with driving stability. This section will first review previous work analysing driver behaviour in crosswind conditions. The last part of the section will include a background on the topic of what is subjectively assessed by drivers as driving stability issues.

2.4.1 Driver behaviour

Drivers react differently to crosswind excitations. Nevertheless, a study by Wagner and Wiedemann [67] concluded that the human driver might amplify the vehicle response when correcting for crosswinds in the frequency range of 0.5 – 2 Hz [67, 68]. At frequencies <0.5 Hz, the driver can correct for slow changes and at frequencies >2 Hz, the changes are too rapid for the driver reaction [67], and the spectral energy of the flow is also lower at these frequencies [10, 30]. Note that, the vortex shedding frequency at the vehicle base is dependent on the flow velocity, but at highway driving it is well above 2 Hz for a typical passenger vehicle [69]. Therefore, to affect the human-vehicle system in the critical region of 0.5 – 2 Hz requires strong wake dynamic effects or external excitations, such as crosswinds.

2.4.2 Subjective assessment

During vehicle development, the final assessment of driving stability is often done by experienced drivers on test tracks. Their subjective judgement has proven to be reliable and reproducible. However, their subjective evaluation cannot be used directly in any virtual vehicle dynamics computer simulation. Therefore, it is necessary to correlate subjective assessment with objective quantities of the vehicle motion. The yaw velocity, lateral acceleration, lateral deviation and headrest acceleration have been shown to correlate with the subjective assessment of crosswind sensitivity [18, 70]. In addition, smaller steering wheel corrections were correlated with improved ratings when evaluating the total drivability at high speed in [71]. Other studies using driving simulators have also identified the drivers' perceivable limits [72] and shown that drivers are sensitive to yaw and roll velocity [73, 74], lateral acceleration and the time delay between these motions [74].

3

Methodology

This chapter introduces the numerical and experimental methodologies used in this work.

3.1 Test object

This thesis used a compact sports utility vehicle (SUV) as the test object. The vehicle mass was 1845 kg, with 57 % of the static load on the front axle. The suspension system consisted of a MacPherson front suspension and a 4-link trailing arm rear suspension, with anti-roll bars at both axles. Coil springs and passive dampers control the system. The vehicle was equipped with an electronic power-assisted steering (EPAS) system. The virtual model of the vehicle, used in the numerical work, included the detailed underbody and engine bay, but modelled the 235/50 R19 tyres as slicks. Figures 3.1 presents a rendered image of the test vehicle.

3.2 Numerical methodology

Numerical tools were used to predict the aerodynamic and vehicle dynamic effects on driving stability. The aerodynamic forces and moments were predicted using both computational fluid dynamics (CFD) simulations and via modelling approaches approximating the aerodynamic response. The vehicle dynamic models of varying fidelity are presented, along with descriptions of coupling methods between the disciplines. The numerical studies were conducted at the vehicle velocity (v_x) of 160 km/h.

Figure 3.1: *A rendered image of the vehicle used in the thesis.*

3.2.1 Computational fluid dynamics

All aerodynamic CFD simulations were performed using the cell-centred finite volume solver ANSYS Fluent (versions 2020R1 to 2021R2). Resolving time-dependent forces that affect driving stability required scale-resolving simulations, where the hybrid Reynolds-averaged Navier-Stokes (RANS) – large eddy simulation (LES) approach was best suited for external automotive aerodynamics. The stress-blended eddy simulation (SBES) turbulence model [75] was used, with the SST k-ω in the RANS region and the dynamic Smagorinsky model (DSM) [76] for the sub-grid scale modelling in the LES region. The dependent variables were discretised using second-order accurate discretisation schemes. The bounded central difference scheme was used for the velocity components, while the turbulence quantities were discretised using the second-order upwind scheme. The bounded second-order implicit temporal scheme was used to advance in time. The solver settings are summarised in Table 3.1.

A hexahedral-dominant mesh was set up with refinements in regions of large gradients; near the vehicle surface, close to the wheels and roof spoiler and in the wake behind the vehicle. The wake refinements extended outward to resolve gradients in crosswind and gusty conditions. A mesh and time step study was carried out in Paper C. The resulting mesh consisted of approximately 190×10^6 cells, with 15 prism layers on the exterior for a $y^+ < 1$ approach in the sub-viscous region. The prism layers can be seen in the zoomed view in Figure 3.2, where a gradual growth can be observed between the prism layers, the intermediate tetrahedral layer, and the hexahedral mesh. The top view in Figure 3.2 shows three of the refinement zones' sizes, while cell sizes as small as 4.25 mm were used around the wheels, the spoiler and curved surfaces. The time steps (Δt) of 1.6×10^{-4} s and 2.5×10^{-4} s was used, with 4 inner iterations. This resulted in normalised time step sizes ($l/(V_\infty \Delta t)$, where l is the vehicle length) above 400, as recommended by Ekman et al. [77]. The mesh accuracy was further evaluated by analysing the mesh quality in the wake behind the vehicle, using two-point correlation (Equation 3.1) of the longitudinal velocities along the three lines in Figure 3.2.

$$C^{norm}_{v'_x v'_x}(x_A, x_B) = \frac{\overline{v'_x(x_A)\, v'_x(x_B)}}{v_{x,rms}(x_A)\, v_{x,rms}(x_B)} \tag{3.1}$$

Table 3.1: *CFD solver settings.*

Turbulence model	SBES SST k-ω
Sub-grid scale model	Dynamic Smagorinsky model (DSM)
Pressure-velocity coupling	Coupled
Gradient scheme	Least Squares cell-based
Pressure discretization	Second-order
Momentum discretization	Bounded Central Difference
Turbulence discretization	Second-order
Temporal discretization	Bounded second-order implicit

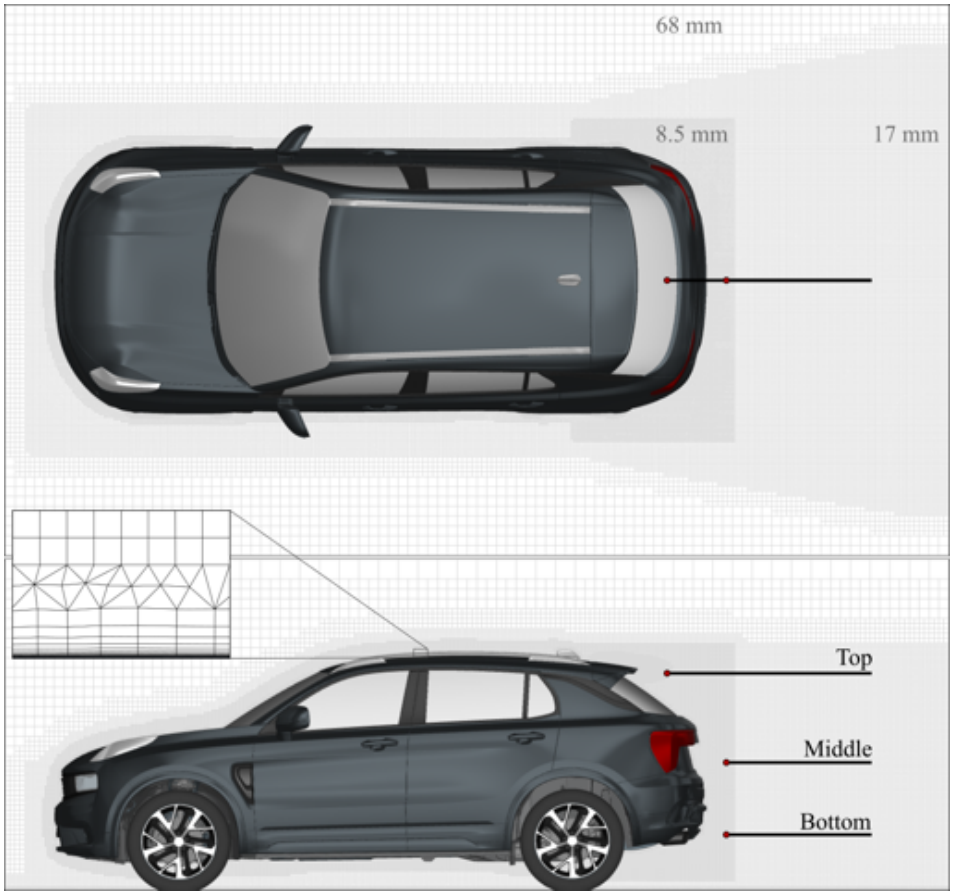

Figure 3.2: *The mesh showing the zone refinements around the vehicle, a zoom-in of the prism layers, and the two-point correlation lines.*

The two-point correlation was proposed by Davidson [78] as a better alternative when evaluating LES resolution compared to, e.g., energy spectra and resolved turbulent kinetic energy. The normalised two-point correlation (Equation 3.1) between spatial coordinates x_A and x_B gives a value close to unity when the signals are highly correlated and close to zero for uncorrelated signals. Each line in Figure 3.2 has its reference point x_A (red dot) closest to the vehicle. The number of correlated cells along a line in a separated region indicates how well the mesh can resolve turbulent structures. According to [78], at least eight cells should be correlated in LES to resolve the largest eddies properly. All lines fulfilled this criterion as seen in Figure 3.3.

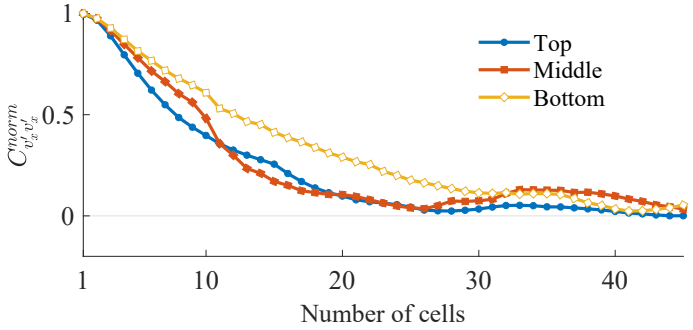

Figure 3.3: *The two-point correlation results.*

The CFD boundary conditions differed between the analyses of high speed stability at fixed yawed flow angles and for the crosswind gust sensitivity analyses.

Boundary conditions for high speed stability analysis

The high speed stability analyses were performed in fixed yawed flow angles (ψ). Figure 3.4 visualises the flow components, where the crosswind velocities (w_y) were chosen to match the investigated flow angles. These flow components (v_x and w_y) formed the boundary conditions at the velocity inlets. Zero-pressure boundary conditions were used at the outlets (opposite the inlets). The domain roof had a Neumann zero-gradient boundary condition while the ground was modelled as a moving wall with the longitudinal vehicle velocity, v_x. The tyres had moving (rotating) wall conditions while the rim rotations were modelled using moving reference frames (MRFs). The domain size was sufficiently large to avoid any effects from the inlet and outlet and had a blockage of less than 0.4 %. The length of the domain was $16.1l$, the width $8.9l$ and the height $4.4l$. The unsteady simulations were initialised with steady-state RANS, followed by a 2 s unsteady solution for flushing the domain and setting the final solver settings. Then, the simulations were run for 5 s physical time for averaging and to resolve any low-frequency fluctuations at 0.5–2 Hz ($\mathrm{St} = 0.05 - 0.2$).

Boundary conditions for crosswind gust sensitivity analysis

The boundary conditions at the sides and the inlet of the domain needed to be altered to simulate transient gusts travelling through the domain. The sides used periodic boundary conditions (green in Figure 3.4), while the remaining inlet specified the fixed v_x component and the crosswind as a time-dependent $w_y(t)$ variable. The gust simulations used the same flushing methodology, before simulating the gusts twice to average the transient response.

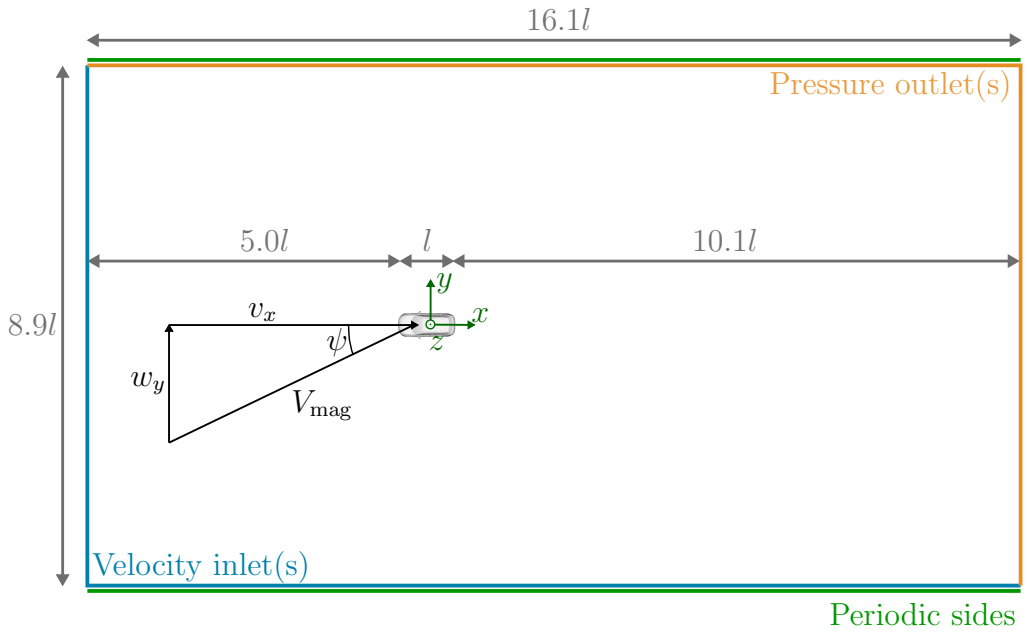

Figure 3.4: *Top view of the computational domains with inlet, outlet and periodic boundaries marked in blue, orange and green, respectively. The relations between the flow angle, ψ, flow velocity, V_{mag}, vehicle velocity, v_x, and lateral wind component, w_y, are shown.*

3.2.2 Aerodynamic modelling

The transient aerodynamic response to crosswind gusts can be approximated using aerodynamic models. The advantage of modelling the aerodynamic response is the fast calculation time in fractions of seconds, compared to the simulation time of days for the transient CFD simulations.

The experimental on-road study in Paper A resulted in a classification of crosswind gust profiles, used throughout the thesis in the aerodynamic modelling.

Gust profile classification

Measurement of vehicle-local flow conditions throughout several weeks of test-track driving under different wind conditions enabled a broad classification of gust profiles. The profiles were mathematically defined by a piecewise function of the crosswind gust, inspired by Favre and Efraimsson [79]. The function can be seen in Equation 3.2 and has four parameters controlling the crosswind amplitude and four parameters specifying the time duration in each stage of the gust profile, see Figure 3.5 for a graphical explanation of the gust parameters. Visual inspection of the flow data resulted in the classification of the four classes (A–D) seen in Figure 3.6 and described below:

A is characterised by a continuously changing crosswind, with a zero-crossing between two peak values. This type of crosswind gust was one of the most frequent in the experimental data. The regularly changing crosswind implies that the drop time is longer than the build-up time, $t_d > t_b$.

B is characterised by a slow build-up time and a rapid drop, including a zero-crossing. The profile is similar to profile A, except that the drop time is shorter than the build-up time, $t_d < t_b$.

$$
\boldsymbol{w_y(t)} \begin{cases} = \boldsymbol{w_y^{start}} & \text{for } t < t_0 \\ = \boldsymbol{w_y^{start}} + \frac{\boldsymbol{w_y^{max}} - \boldsymbol{w_y^{start}}}{\boldsymbol{2}} \left(\boldsymbol{1} - \boldsymbol{\cos}\left(\frac{\boldsymbol{\pi}}{\boldsymbol{t_b}} \left(\boldsymbol{t} - \boldsymbol{t_0}\right)\right)\right) & \text{for } t_0 < t < t_0 + t_b \\ = \boldsymbol{w_y^{max}} & \text{for } t_0 + t_b < t < t_0 + t_b + t_p \\ = \boldsymbol{w_y^{max}} - \frac{\boldsymbol{w_y^{max}} - \boldsymbol{w_y^{min}}}{\boldsymbol{2}} \left(\boldsymbol{1} - \boldsymbol{\cos}\left(\frac{\boldsymbol{\pi}}{\boldsymbol{t_d}} \left(\boldsymbol{t} - \boldsymbol{t_0} - \boldsymbol{t_b} - \boldsymbol{t_p}\right)\right)\right) & \text{for } t_0 + t_b + t_p < t < t_0 + t_b + t_p + t_d \\ = \boldsymbol{w_y^{min}} & \text{for } t_0 + t_b + t_p + t_d < t < t_0 + t_b + 2t_p + t_d \\ = \boldsymbol{w_y^{end}} + \frac{\boldsymbol{w_y^{min}} - \boldsymbol{w_y^{end}}}{\boldsymbol{2}} \left(\boldsymbol{1} + \boldsymbol{\cos}\left(\frac{\boldsymbol{\pi}}{\boldsymbol{t_b}} \left(\boldsymbol{t} - \boldsymbol{t_0} - \boldsymbol{t_b} - \boldsymbol{2t_p} - \boldsymbol{t_d}\right)\right)\right) & \text{for } t_0 + t_b + 2t_p + t_d < t < t_0 + 2t_b + 2t_p + t_d \\ = \boldsymbol{w_y^{end}} & \text{for } t > t_0 + 2t_b + 2t_p + t_d \end{cases} \tag{3.2}
$$

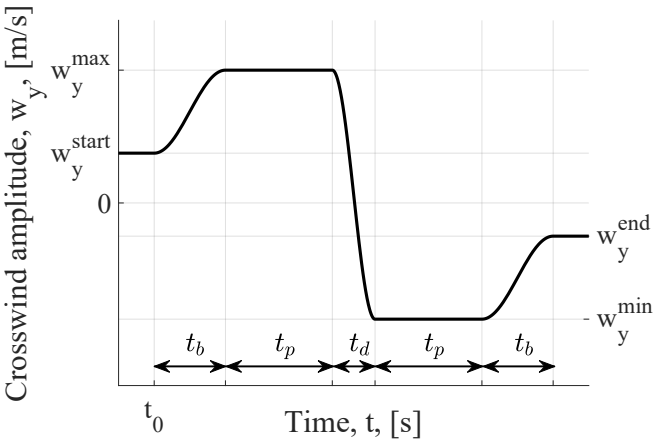

Figure 3.5: *Graphical representation of the gust parameters in Equation 3.2, were the time parameters define the build-up time, t_b, pausing time, t_p and the drop time t_d.*

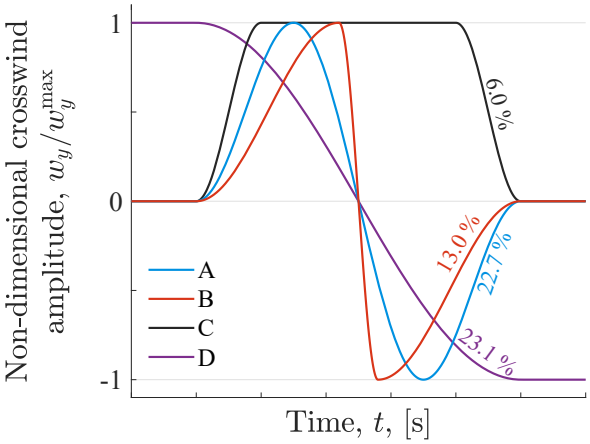

Figure 3.6: *The four gust classes (A-D) classified in the experimental study and their frequency of occurrence (35.2 % undefined).*

C is characterised by the quick ramp-up and ramp-down of the crosswind and a relatively long pause at the maximum crosswind magnitude without zero-crossing. The gust profile starts and ends with no crosswind and is the profile that best represents the crosswind sensitivity testing at crosswind facilities, described in ISO 12021:2010 [23]. This type of crosswind was the least common during the experimental on-road testing at the test track.

D is characterised by a simple transition between two levels in the magnitude of the crosswind. The example in Figure 3.6 includes a zero-crossing, but the experimental data also showed examples of a quick ramp down from a constant to no crosswind. The build-up and pause times are set to zero in this profile, $t_b = t_p = 0$, and the initial crosswind magnitude equals the maximum magnitude, $w_y^{\text{start}} = w_y^{\text{max}}$, and the end and minimum magnitudes are also equal, $w_y^{\text{min}} = w_y^{\text{end}}$. A step function of the crosswind can be created by decreasing the drop time duration towards zero, $t_d \to 0$.

Gust classes A and B can be seen as variants of a common base profile with a combined percentage of 35.7 %. However, it is evident that the wind data were highly irregular since 35.2 % of the crosswind gusts did not fit into any of the four classes. Nevertheless, this classification of gust profiles enhances the possibility of using real-world inspired crosswind gust profiles in virtual simulations. Table 3.2 defines gust profiles 1, 2 and 3 (used in the numerical crosswind studies) corresponding to gust class A, B and C, respectively. The crosswind amplitude of ±5 m/s equals a flow angle of ±6.4 deg at the vehicle velocity of 160 km/h. This represents considerable, yet realistic, crosswind conditions. The gust duration, t_{gust}, of 1.6 s was chosen based on the typical gusts seen in the experimental data. It translates to 16 vehicle lengths, which lies in the critical range for vehicle dynamic crosswind stability reported in previous works [10, 29, 30]. Profiles 1 and 2 were chosen to investigate the effects of different build-up times, t_b, and drop times, t_d, for gust profiles that included a zero-crossing of the flow angle. The third profile does not include the zero-crossing, but has a fast build-up time and a longer pausing time, t_p, and thus a higher integral of the crosswind velocity.

Table 3.2: *Values used in Equation 3.2 to build the gust profiles used in the numerical studies.*

	Gust class	w_y^{start} [m/s]	w_y^{max} [m/s]	w_y^{min} [m/s]	w_y^{end} [m/s]	t_b [s]	t_p [s]	t_d [s]	$t_{\text{gust}} = 2t_b + 2t_p + t_d$ [s]
Profile 1	A	0	5	-5	0	0.5	0	0.6	1.6
Profile 2	B	0	5	-5	0	0.7	0	0.2	1.6
Profile 3	C	0	5	5	0	0.3	0.5	0	1.6

Quasi-steady models

The transient aerodynamic response to the gusts can be approximated using quasi-steady models. The standard and an extended quasi-steady approach were compared to the transient CFD (tCFD) gust simulations described below.

- A **Quasi-steady (QS)** approach; uses tabled data of time-averaged aerodynamic loads at a range of set flow angles to create a linear interpolant. The averaged data originated from unsteady CFD simulations at constant flow angles. The interpolant function determines the aerodynamic response during the crosswind gust, based on the instantaneous flow angle and magnitude. This method is flexible since the aerodynamic load from any gust profile can be approximated once the tabulated data is created (within the flow angles of the tabulated data). The drawback is that all transient aerodynamic effects are neglected.

- A **Quasi-steady with axle delay (QSD)** approach; extends QS by accounting for the effect of the time delay between the front and rear axles when driving into a gust ($\Delta t = \frac{L}{v_x}$). This is one way to represent the flow delay along the vehicle. The yaw moment and side force were split up into the front and rear side forces, as

$$F_{sf} = \frac{F_S}{2} + \frac{M_z}{L} \text{ and} \tag{3.3}$$

$$F_{sr} = \frac{F_S}{2} - \frac{M_z}{L}. \tag{3.4}$$

  Similarly, the lift force and pitch moment were divided into front and rear lift. The roll and drag contributions were divided equally between the axles. This per-axle formulation enabled the phase shift of the aerodynamic response, e.g. the side force and yaw moment:

$$F_S(t) = F_{sf}(t) + F_{sr}(t - \Delta t) \tag{3.5}$$

$$M_z(t) = \frac{L}{2}\left(F_{sf}(t) - F_{sr}(t - \Delta t)\right) \tag{3.6}$$

  The QSD has the additional advantage of accounting for the transient aerodynamic effect of the axle delay. However, the method neglects any transient fluid dynamic effects.

- A **transient CFD (tCFD)** approach; simulated the full crosswind gust events twice via a transient inlet condition. Each gust was simulated twice (with different starting times of the gust) to increase the reliability of the transient solution by making an average of the forces and moments at each time step. This approach accounts for the axle delay and any fluid dynamic effects, but requires two simulations per gust profile, making it costly.

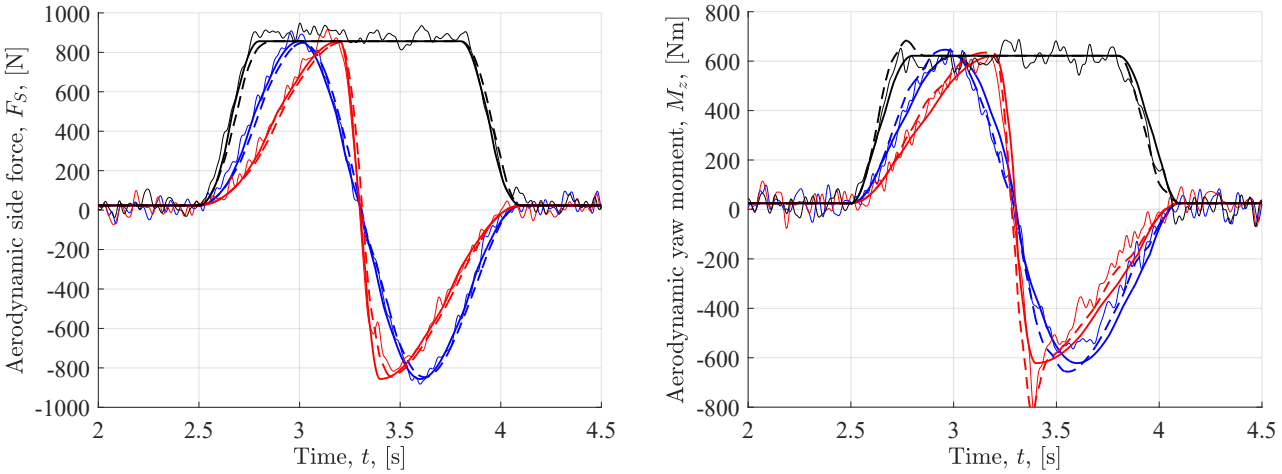

(a) *Side force.* **(b)** *Yaw moment.*

Figure 3.7: *The aerodynamic response for gust profile 1 (**blue**), profile 2 (**red**) and profile 3 (**black**), comparing tCFD (thin lines —) to QS (thick lines —) and QSD (thick dashed lines - - -) approaches.*

Figures 3.7a and 3.7b display the aerodynamic side force and yaw moment responses, respectively. The figures present comparisons between the three crosswind gust profiles and between the three aerodynamic response modelling methods: quasi-steady (QS), quasi-steady with axle delay (QSD) and transient CFD (tCFD). To improve visibility, the tCFD results were filtered through a 32 Hz low-pass filter. As can be seen in Figure 3.7a, there are minor differences in the side force response between the modelling methods (thin, thick and dashed lines). Both quasi-steady approaches neglected any transient fluid dynamic effects, and since the transient CFD (which accounts for those effects) showed similar results, it could be concluded that no significant transient effect of the side force is present during crosswind gusts of the magnitude and time interval investigated in this study. Furthermore, the modelling of the time delay between the axles had a small effect on the side force results (thick and dashed lines in Figure 3.7a).

The axle delay modelling had a more substantial effect on the yaw moment response (Figure 3.7b). Note especially the positive peak overshoot at 2.75 s of QSD profile 3 (black dashed) and the negative peak of QSD profile 2 (red dashed) at 3.4 s. These effects can be explained by the observation that in constant crosswind flow, the front axle side force works to turn the vehicle away from the crosswind (increasing the aerodynamic yaw moment), while the rear axle side force works in the opposite direction for the yaw moment, as demonstrated by Theissen [30]. The positive yaw moment overshoot at 2.75 s resulted from high front axle side force without any counteracting side force at the rear axle. The effect at 3.4 s is even more significant, as the rapid change in flow angle resulted in a brief instance when the front and rear axle side forces worked together to decrease the yaw moment to its negative peak value. This effect could be confirmed by the tCFD, which also showed a negative peak at 3.4 s and an overall better agreement with the QSD solution. Moreover, this also indicated that there was no significant transient fluid dynamic effect for the yaw moment either.

In summary, neither the aerodynamic side force nor the yaw moment showed any transient fluid

dynamic effects at these crosswind magnitudes and gust time intervals. Therefore, the QSD modelling approach was considered an acceptable approximation of the aerodynamic response to crosswind gusts. The overshoots of the aerodynamic yaw moment could be explained by the time delay between the front and rear axles when driving into crosswinds.

3.2.3 Vehicle dynamic modelling

The vehicle dynamic response to the aerodynamic loads affects the vehicle sensitivity and the drivers' perception of driving stability. Vehicle dynamic models enable virtual assessment of vehicle response in various driving scenarios. Therefore, models must be representative of the real vehicle and have sufficient fidelity (accuracy) to emulate the vehicle response. The most accurate models are the detailed multi-body dynamics (MBD) models, where kinematic and elasto-kinematic effects of the chassis, suspension and steering systems are modelled as one complex system. As a result, MBD models use the positions (hard points) of the suspension and steering components as input for building the model; thus, defining the model at a low hierarchical level. These complex models are often said to be of high fidelity. However, vehicle requirements are set on a system level, a higher hierarchy than the hardpoint-defined models. Hence, this becomes a drawback when analysing the sensitivity of system properties since multiple properties change when altering the hardpoints in high-fidelity models. A viable alternative is to use the models defined on a system level, such as the bicycle model. Although they present lower fidelity, their inherent definition makes them useful when assessing system properties and finding suitable requirement settings. Additionally, lower fidelity models can be used earlier in the vehicle design process when hardpoint details are still not defined. Despite their many advantages when lower fidelity models are preferred, the accuracy issue still needs to be addressed. The accuracy of four models of varying fidelity has been evaluated and used in this thesis:

- The **classical bicycle one-track model (low fidelity)**; has 2 degrees of freedom (DoF): lateral and yaw motion. The tyres were modelled linearly with a lateral cornering stiffness coefficient, linearised around the static axle loads.

- The **enhanced 3 DoF model (mid fidelity)**; was based on the bicycle model, but several additional vehicle properties were implemented to increase its accuracy. It was found that including a roll DoF improved the model (in agreement with the conclusions of a previous study on the effects of roll dynamic for crosswind sensitivity [28]). The lateral tyre cornering stiffness was modelled, based on the normal load, using a 2^{nd} order polynomial. The polynomial was fitted to experimental tyre data. Furthermore, the enhanced model accounted for kinematic and elasto-kinematic steering effects in the suspension system. Figure 3.8 shows a schematic view of the enhanced model.

- The **enhanced 6 DoF model**; extended to enhanced 3 DoF model by including vertical (heave and pitch) and longitudinal dynamics to evaluate the high speed stability effects of the aerodynamic lift and drag forces. The vertical suspension stiffness and damping were modelled for each axle. Hence, this model had 6 degrees of freedom.

- The **multi-body dynamic model (high fidelity)**; was used as the reference model. It was built in Adams/Car, using the *PAC2002* [80] (Pacejka Magic Formula) tyre model and had a Gruebler count of 2136 (approximate degrees of freedom).

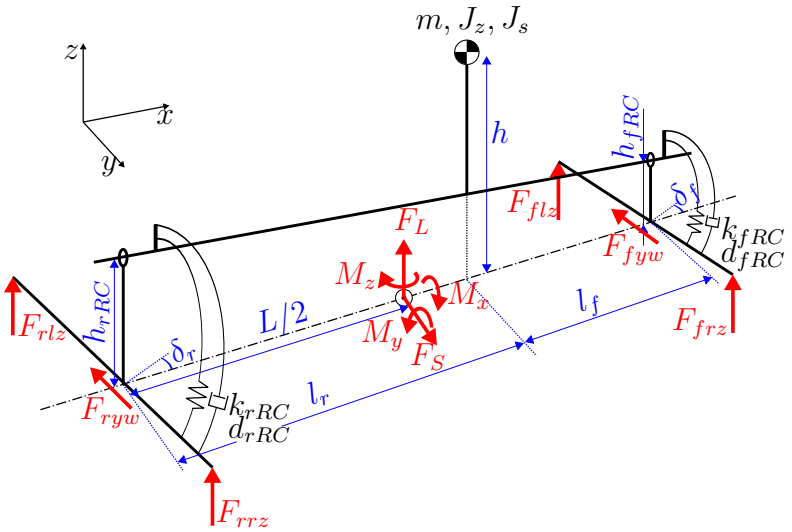

Figure 3.8: *The enhanced model (mid-fidelity), including the aerodynamic force play.*

Model validation

The motion responses of the low-, mid- and high-fidelity models were compared for the three gust profiles, using the QSD approach based on tabulated windtunnel data as aerodynamic input, see Figure 3.9. The validation focused on the road plane motions: lateral acceleration (a_y) and yaw velocity (ω_z), known to affect the subjective assessment of driving stability [1, 18, 70]. The high-fidelity model was used as reference. Evidently, the classical bicycle model (low fidelity) failed to emulate the response in terms of yaw velocity and lateral acceleration, acting as a too damped system. The enhanced model (mid fidelity) matched the response of the high-fidelity model well, proving that the essential system properties for this load case have been accurately implemented in this model.

To further justify the use of the enhanced model, a validation was performed using the experimental test track data from Paper A. Thirteen instances of experienced stability issues were selected from the data set. The measured vehicle motion response during the events could then be compared to the modelled response, where the vehicle-local wind measurements were converted to aerodynamic inputs using the quasi-steady approach. The driver steering was also used as input to the enhanced 3 DoF model. Figure 3.10 shows the comparison for one of the instances. The model successfully captures the rapid changes and amplitude values of the measured data. All 13 instances were analysed, and Figure 3.11 compared the measured and modelled values of the combined proxy measure (Equation 4.1). The diagonal line shows the ideal solution, where the modelled and measured values are equal. The data showed a fit of $R^2 = 0.86$ to the diagonal line, which was regarded as acceptable considering the uncertainty of the measurement equipment and external disturbances (such as road unevenness) during the test track experiments. However, the model seemed to overpredict the response of the two strongest crosswind events. The highest driver steering wheel intervention was found at these events; hence, too simple modelling of the steering system could explain the overpredictions. Nevertheless, the studies presented in this work used a fixed steering wheel angle, and the simplified steering system did not affect those results. The red square data point represents the instance seen in Figure 3.10.

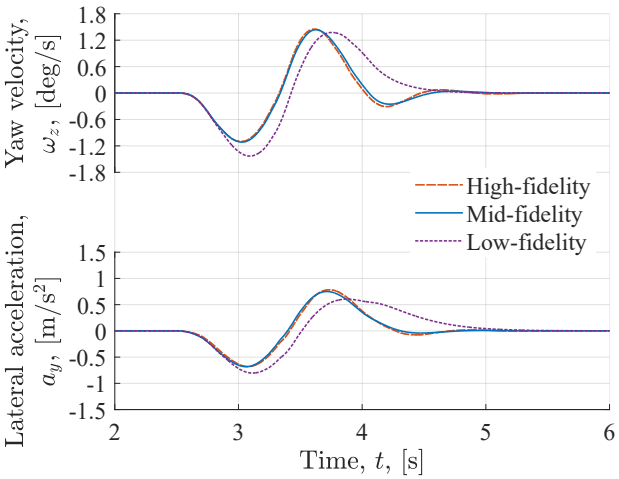

(a) *Profile 1.*

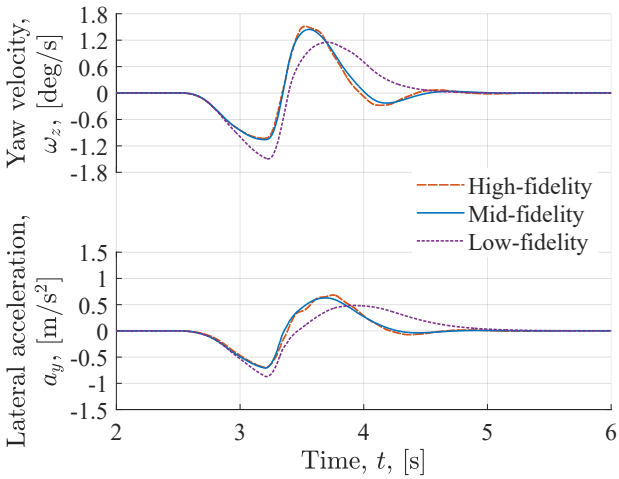

(b) *Profile 2.*

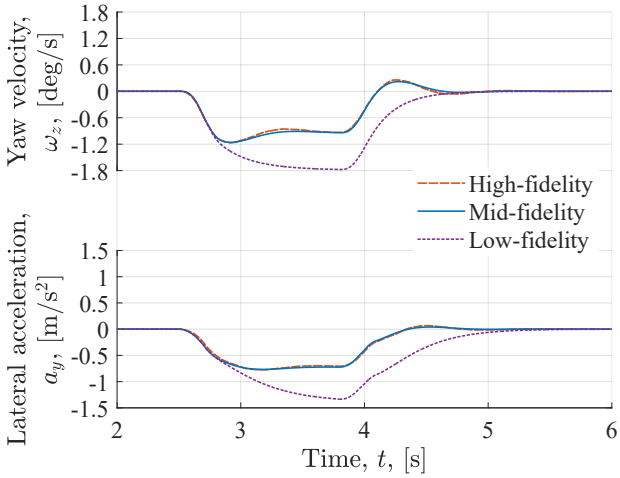

(c) *Profile 3.*

Figure 3.9: *Fidelity analysis; comparing the yaw velocity and lateral acceleration response during the gust profiles, for the three vehicle dynamics models.*

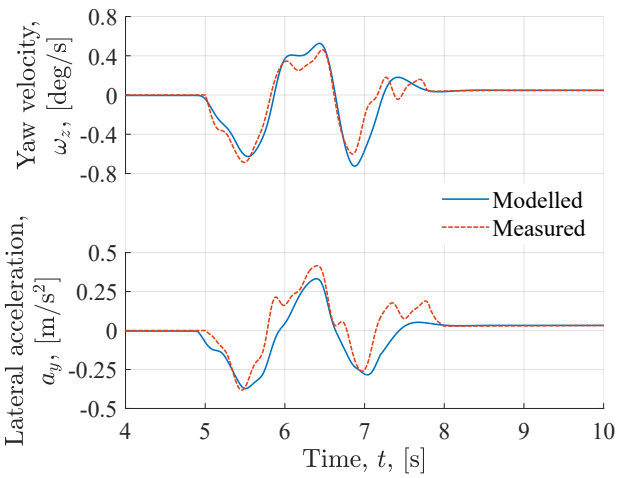

Figure 3.10: *Validation of the enhanced (mid-fidelity) model; comparing modelled versus measured yaw velocity and lateral acceleration response during crosswind gust event No. 8.*

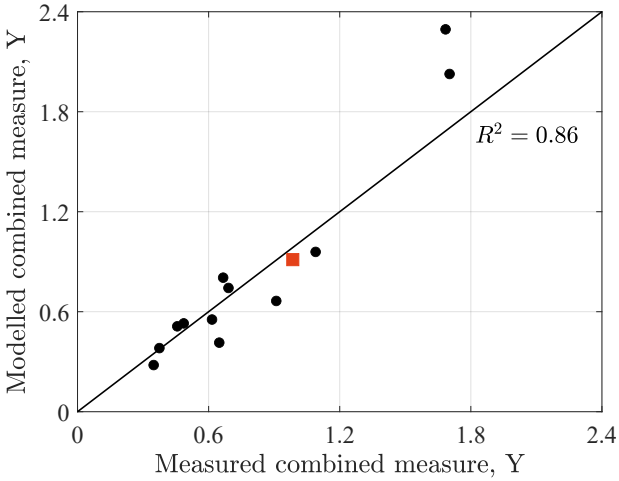

Figure 3.11: *Measured vs. modelled values of the proxy measure, Y (Equation 4.1). The red square corresponds to gust event No. 8, seen in Figure 3.10.*

Driver modelling

A simple driver model was used for all numerical vehicle dynamic modelling. The driver model used a locked steering angle, which was calculated to yield zero yaw velocity and lateral acceleration prior to applying unsteady aerodynamic forces and moments.

3.2.4 Numerical coupling

The numerical coupling between aerodynamics and vehicle dynamics can be implemented in two ways. The most straightforward is to use a 1-way coupling, where the aerodynamic load is applied on the vehicle dynamic model, but the vehicle motion response does not affect the aerodynamics. The more authentic description would include the vehicle motion changes in the aerodynamic modelling, as in a 2-way coupling.

The necessity of a lateral 2-way coupling for SUVs was investigated. The coupling was performed using the aerodynamic QSD model coupled to the enhanced 3 DoF vehicle dynamic model. The QSD model uses the relative flow magnitude, V_{mag}, and angle, ψ, as inputs. By accounting for the vehicle body slip, β, and the global yaw angle, ϕ_z, the 2-way coupling could implement road perpendicular crosswinds via the flow conditions, as in Figure 3.12. Equation 3.7 express the relative flow velocity and angle. The 2-way coupling was also implemented as crosswinds perpendicular to the motion vector of the vehicle, $v_v = \sqrt{v_x^2 + v_y^2}$. For this, Equation 3.7 could be simplified to Equation 3.8 by setting $\phi_z = -\beta$. Similarly, the 1-way coupling formulation was achieved by setting $v_y = 0$ and $\phi_z = 0$, see Equation 3.9.

2−way road perpendicular

$$V_{\text{mag}} = \sqrt{v_v^2 + w_y^2 + 2v_v w_y \sin(\beta + \phi_z)}, \qquad \psi = \arctan\left(\frac{w_y + v_v \sin(\beta + \phi_z)}{v_v \cos(\beta + \phi_z)}\right) - \phi_z \tag{3.7}$$

2−way

$$\phi_z = -\beta \;\Rightarrow\; V_{\text{mag}} = \sqrt{v_v^2 + w_y^2}, \qquad \psi = \arctan\left(\frac{w_y}{v_v}\right) + \beta \tag{3.8}$$

1−way

$$v_y = 0,\ \phi_z = 0 \;\Rightarrow\; V_{\text{mag}} = \sqrt{v_x^2 + w_y^2}, \qquad \psi = \arctan\left(\frac{w_y}{v_x}\right) \tag{3.9}$$

Figure 3.13 show the vehicle motion response comparing the 1-way and 2-way coupled solutions,

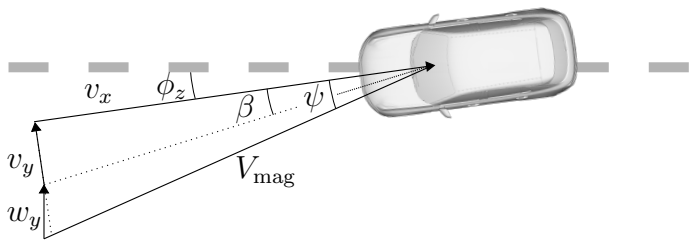

Figure 3.12: *Schematics of the lateral 2-way coupling between aerodynamics and vehicle dynamics through the relative flow angle and magnitude.*

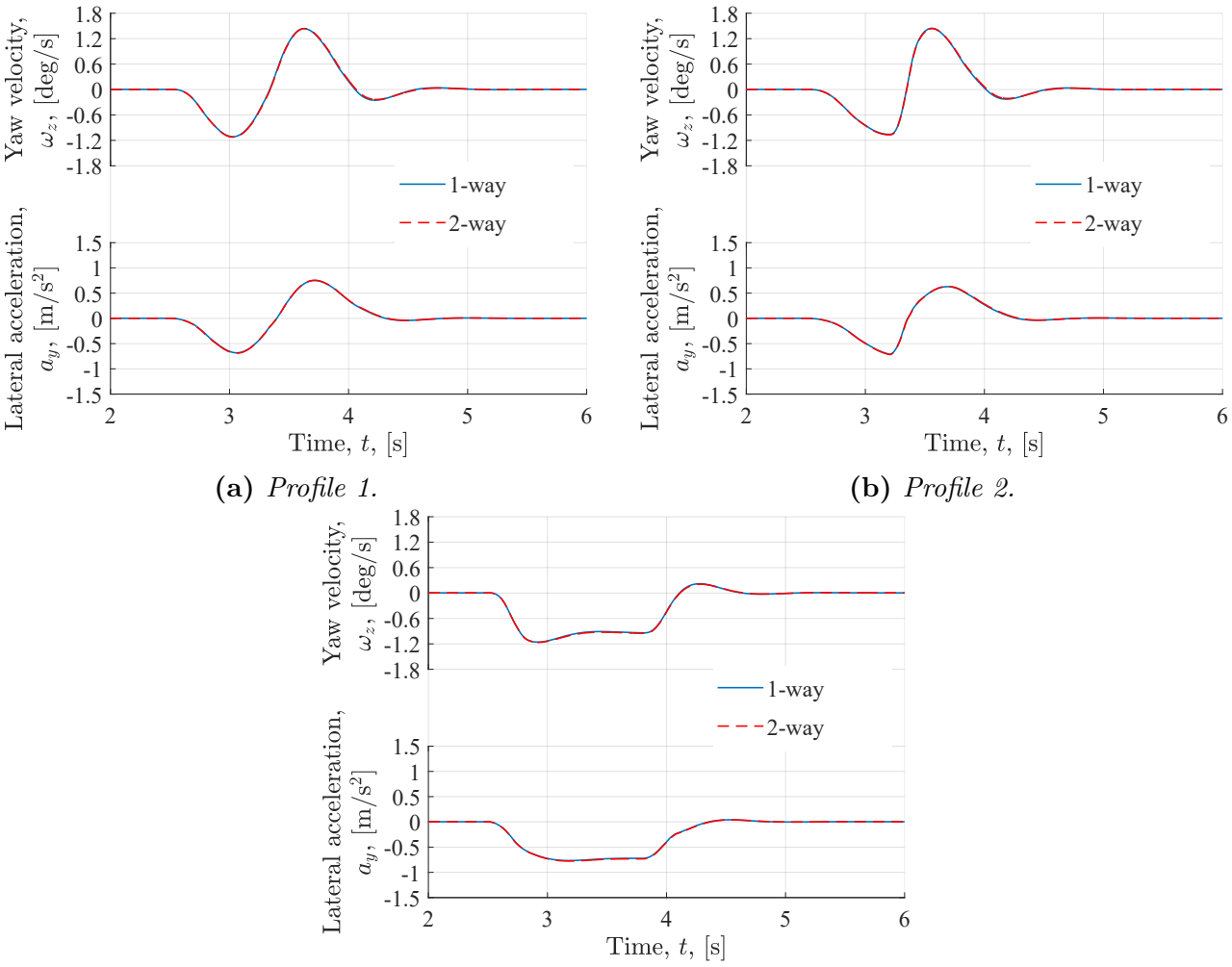

(a) *Profile 1.*

(b) *Profile 2.*

(c) *Profile 3.*

Figure 3.13: *The vehicle motion response in terms of yaw velocity, ω_z, and lateral acceleration, a_y, for the three gust profiles, comparing 1-way and 2-way coupled solutions for the SUV.*

for the three gust profiles. The effects of the 2-way coupling (by accounting for the vehicle body slip) were negligible for an SUV at these crosswind conditions. Although the discrepancy between the coupling methods was slight, the largest effects were seen during gust profile 3 (Figure 3.13c).

3.3 Experimental methodology

Experiments were carried out in the CEVT (China Euro Vehicle Technology) driving simulator, on Hällered proving ground (HPG) and at Volvo Cars aerodynamic wind tunnel (PVT).

3.3.1 Driving simulator testing

The CEVT driving simulator (Figure 3.14) is a VI-grade DiM250 simulator; a system where the front half of the vehicle body is mounted on a 6 degrees of freedom hexapod base frame, which in turn can be actuated planary across the floor using air bearings [81]. The testing

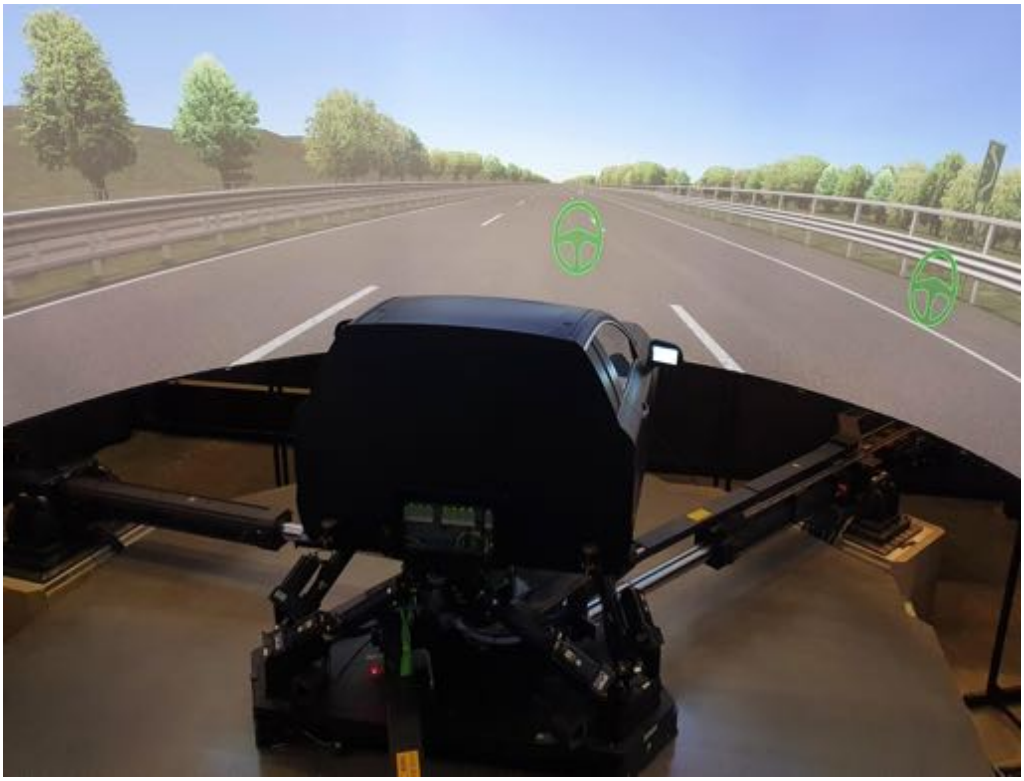

Figure 3.14: *The VI-grade DiM250 driving simulator at CEVT.*

performed in this work used a straight-line highway environment with three flat lanes of road class A. As seen in Figure 3.14, the surrounding environment included road railings, trees, bushes and viaducts for improved perception of longitudinal speed through the visuals. The simulator used CarRealTime for the vehicle dynamic modelling, where a model of the test object was implemented. The CarRealTime model had a Matlab/Simulink interface, which enabled an adjustable coupling between aerodynamics and vehicle dynamics. The aerodynamic forces and moments were specified and applied in an aerodynamic reference point at ground level, in the lateral symmetry plane in the middle between the axles.

3.3.2 On-road testing

The on-road testing was performed at the Hällered proving ground (HPG) high speed test track. All tests were performed in dry conditions and all driving was done by experienced drivers.

Instrumentation

The instrumentation setup was designed to enable synchronised data acquisition of the relative flow conditions, the dynamic motion of the vehicle and the subjective input from the drivers. Table 3.3 lists the measurements and associated equipment.

The magnitude and angle of the vehicle-local flow were measured using a seven-hole probe positioned 371 mm above the roof using a probe holder mounted in place of the shark fin antenna, see Figure 3.15. This, to decrease the vehicle's influence on the measured flow and

Table 3.3: *Instrumentation setup for the experimental high speed driving.*

Equipment	Measurement
7-hole probe Prandtl tube	Flow magnitude and angle
Subjective trigger	Instability events
GPS-RTK	Positioning and speed
IMU	Vehicle motion response

to reduce the flow disturbance over the rear roof spoiler. The probe had a flow cone angle of receptivity of 70 deg and an accuracy of ±1 deg [82]. The probe's pressure tubes were connected to HCLA pressure sensors sampling at 2500 Hz. The pressure sensors measured the pressure difference between a reference pressure (atmospheric pressure) and the holes at the tip of the seven-hole probe. The atmospheric pressure was obtained by the static pressure port of a Prandtl tube mounted 80 mm above the seven-hole probe, see Figure 3.15. The static port pressure of Prandtl tubes is slightly affected by yawed flow, but the pressure error was assumed to be <2 % for flow angles below 10 deg according to [83]. This did not affect the flow angle calibration, but caused a slight variation in the flow magnitude calibration.

A subjective trigger was installed in the cabin to enable analysis of the short events where stability issues were noted. The driver could press the trigger while driving, generating a time mark in the data.

Two GPS antennas were mounted inside the vehicle, on the centre line at the windshield and at the rear of the vehicle. The GPS positioning was enhanced by a real-time kinematic (RTK) system, giving a positioning accuracy of ±0.01 m and velocity accuracy of ±0.1 m/s [84]. The motion of the vehicle was monitored using a Dewesoft DS-IMU2 module, an inertial measurement unit (IMU) that combines gyroscopes and accelerometers with measurement accuracies of ±0.033 deg/s and ±0.032 m/s^2, respectively [84]. The IMU was firmly mounted to the structure of the vehicle, close to the centre of gravity (CoG), see Figure 3.15. The

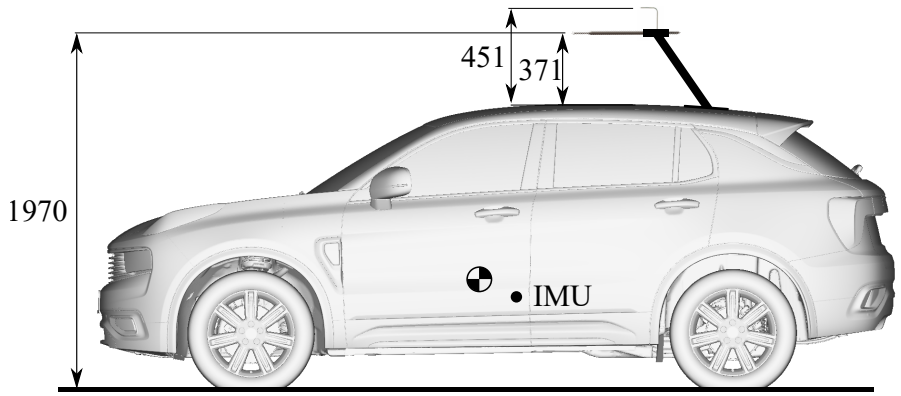

Figure 3.15: *Schematics of the placement of the seven-hole probe and the Prandtl tube in* mm *and the position of the inertial measurement unit (IMU).*

Figure 3.16: *An aerial view of Hällered Proving Ground, showing the oval test track (courtesy of Volvo Car Corporation) [85].*

acceleration measurements could be translated to any point in reference to the IMU placement. In this study, the lower back of the seated driver was used as a reference point. This reference point was selected to enable correlations between the drivers' subjective assessment and their experienced motion in the vehicle.

Test track and test procedure

The analysis was focused on the two 1.1 km straight runs of the oval test track at HPG (see Figure 3.16). Three experienced drivers participated in the studies. Before the data acquisition, a co-driving session was conducted where all drivers independently could trigger at events of substantial stability issues. As all drivers marked the same events, it was concluded that the data from all three drivers could be used in the study. The test drivers were instructed to drive in a straight line and to keep the steering wheel fixed. The test procedure started by driving a couple of laps on the test track to verify the functionality of the measurement equipment and to ensure that the tyres reached operational temperature. The testing was primarily focused on 160 km/h driving, but the vehicle was evaluated at speeds ranging from 120 km/h to 200 km/h.

Post-processing

The flow and vehicle motion data were analysed at the subjective trigger events and compared with the complete data set to find any exceptional trends prior to a trigger. All data were filtered through a Hamming low pass filter of order 500 with a cut-off frequency of 5 Hz. Higher frequencies of the wind and vehicle motion were disregarded for the driving stability analysis.

The time marks from the drivers' subjective triggers were used to analyse the data before the trigger events. Figure 3.17 visualises four signals to exemplify the data analysis with two trigger events as red vertical lines. A window of 3 s before each trigger was marked as the region of instability. It was assumed that the cause of the subjective perception of stability issues would be found within these time intervals, both in terms of the vehicle motion

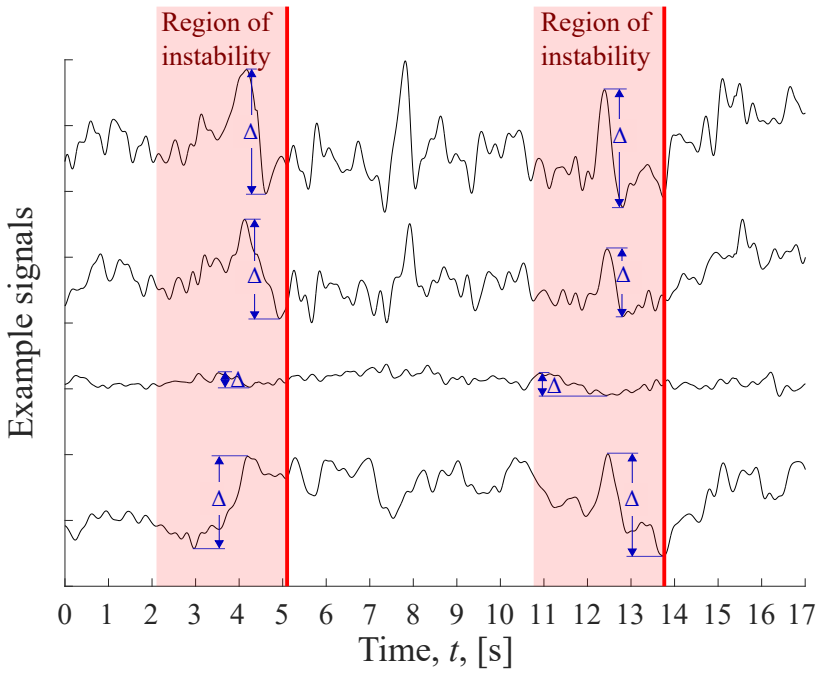

Figure 3.17: *Example of trigger events (red lines) and windows used to visualise the regions of instability.*

response and crosswind conditions. The most robust and useful way to analyse the data was by measuring the amplitude between maximum and minimum peaks within the regions of instability, see Δ amplitudes in Figure 3.17. This was done both for the air flow measurements, to determine typical crosswind conditions before the subjective triggers and for the motion responses experienced by the drivers, to correlate their subjective assessment to quantitative objective measures.

The data at the subjective trigger events were compared to the complete data set to find unusual trends in the trigger data. The comparisons were made using a similar analysis methodology for the complete data set. A sliding window of 3 s, with 1 s stepping, was applied to all the data.

3.3.3 Wind tunnel testing

The wind tunnel experiments were performed at Volvo Cars aerodynamic wind tunnel (PVT). PVT is a closed return tunnel with a slotted wall test section. The test section is 27 m^2 resulting in a $\approx$10 % blockage for a full-scale passenger vehicle. The test section is equipped with a 5-belt moving ground system and a boundary layer control system consisting of a suction scoop, two distributed suction zones and tangential blowers behind the wheels and behind the centre belt. A more detailed description and performance review of the wind tunnel's moving ground and boundary layer control systems can be found in the work by Sternéus et al. [86] and Ljungskog [87]. The vehicle is held in place by four struts. The struts and the whole platform, including the wheel drive units, are connected to the under-floor balance, measuring the forces and moments acting on the vehicle with a repeatability of $\pm 0.001\,C_D$, $\pm 0.001\,C_{lf}$ and $\pm 0.005\,C_{lr}$ within the same test session [86].

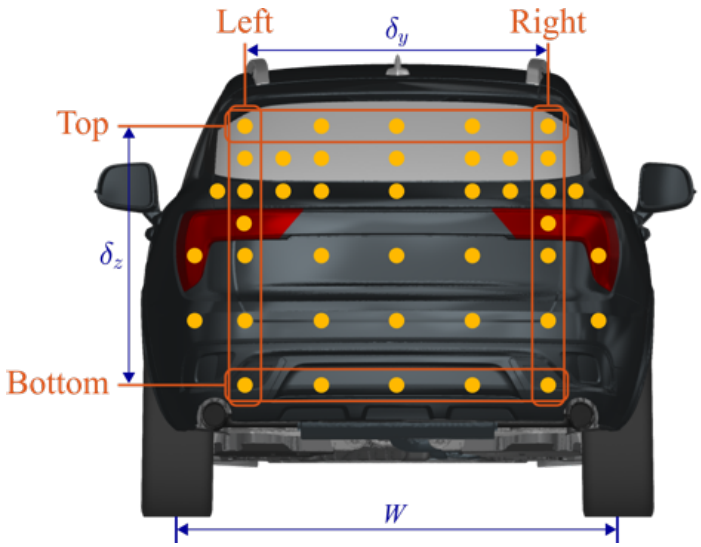

Figure 3.18: *Pressure sensor layout for the wind tunnel experiment, with rows and columns used for creating lateral and vertical base pressure gradients.*

Base pressures were taken during 60 s at 5000 Hz using 42 HCLA pressure sensors connected via 0.1 m tubing to the pressure spades marked in Figure 3.18. The figure also shows the left and right columns used to create the non-dimensional lateral base pressure gradient (Equation 3.10) at every time instance. The top and bottom rows were used for the non-dimensional vertical base pressure gradient (Equation 3.11). The top, bottom, left and right probes were spatially averaged as in Equation 3.12, where n_c and n_r represent the number of columns and rows, respectively, and i is the indexing of the probe in the row or column.

$$\frac{\partial c_p}{\partial y^*}(t) = \frac{c_p^{left}(t) - c_p^{right}(t)}{\delta_y / W} \tag{3.10}$$

$$\frac{\partial c_p}{\partial z^*}(t) = \frac{c_p^{top}(t) - c_p^{bottom}(t)}{\delta_z / W} \tag{3.11}$$

$$\begin{aligned}
c_p^{top}(t) &= \frac{1}{n_c}\sum_{i=1}^{n_c} c_p(y_i, z_{top}, t) \\
c_p^{bottom}(t) &= \frac{1}{n_c}\sum_{i=1}^{n_c} c_p(y_i, z_{bottom}, t) \\
c_p^{left}(t) &= \frac{1}{n_r}\sum_{i=1}^{n_r} c_p(y_{left}, z_i, t) \\
c_p^{right}(t) &= \frac{1}{n_r}\sum_{i=1}^{n_r} c_p(y_{right}, z_i, t)
\end{aligned} \tag{3.12}$$

4

Crosswind sensitivity

The influence of crosswind gusts on vehicle stability has been studied, first by investigating the sensitivities found during on-road experiments at the test track. Then, a coupled aerodynamic and vehicle dynamic simulation methodology was utilised to find critical parameters that influence the vehicle's sensitivity to these winds. Finally, the drivers' perceived sensitivity to crosswinds was studied using a driving simulator setup.

4.1 On-road sensitivity

The results from the test track campaign in Paper A are first presented in terms of the environmental wind conditions of interest for driving stability. After that, a section on subjective assessment and correlated objective measures will follow.

4.1.1 Wind load conditions

The test track experiments showed that the vehicle was subjected to crosswinds that mainly varied between 0 – 5.4 m/s within a 3 s window, see *All data* in Figure 4.1a. It is also evident from the distributions in the figure that higher variations in crosswind correlated with a higher fraction of subjective triggers. The dark brown colour represents the overlap between the two data sets. The discrepancy between the crosswind conditions at the triggers and the complete data set indicates that the change in crosswind was an underlying factor for issues with straight-line driving stability performance in this study. Half of all triggers occur in crosswinds $\geq$5.5 m/s, which only represents 14 % of the total wind data. This correlates a varying crosswind with a decrease in driving stability performance. It should be noted that 16 % of the triggers occur in conditions with little or no wind ($<$3.3 m/s). Therefore, it is assumed that driving stability issues might occur without crosswinds.

The resulting relative flow angle (ψ) is dependent on the vehicle speed (v_x) and the wind components (w_x and w_y). When driving at 160 km/h without any head- or tailwind, a variation in crosswind of 8 m/s results in a relative flow angle variation of 10 deg. Figure 4.1b shows the change in flow angle before triggers and the distribution for the complete data set. The figure displays information that overlaps with Figure 4.1a. However, since the test procedure included different driving velocities, the resulting flow angles could be of interest. Only one-fourth of the complete data set had a varying flow angle above 6 deg, but 59 % of the triggers were recorded at these flow conditions. Furthermore, gusts above 10 deg were rare, but had a high correlation

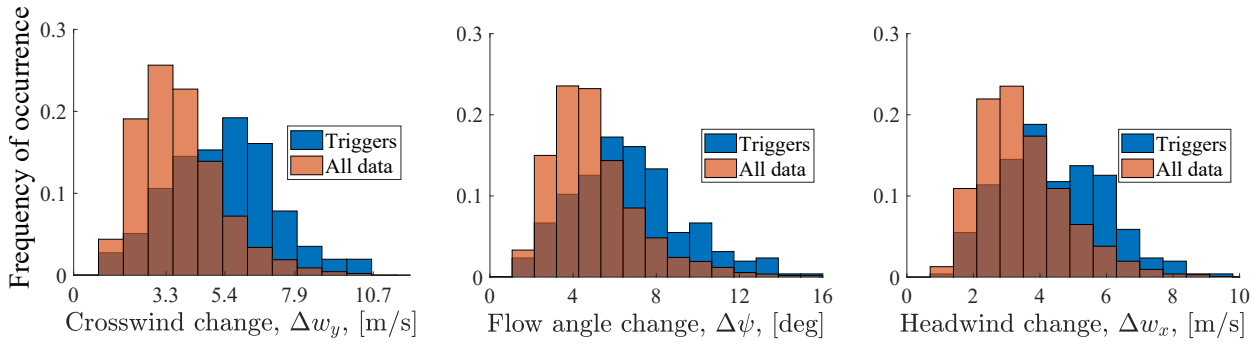

(a) **(b)** **(c)**

Figure 4.1: *The frequency of occurrence distributions for three wind quantities, comparing the data at the trigger events to the complete data set.*

with stability issues. The distributions presented in Figure 4.1b show a smaller discrepancy between triggers and all data than the crosswind magnitude in Figure 4.1a. This indicates that the crosswind magnitude was the more differentiating measure.

Although the discrepancy between the trigger data and the complete data set was small for the headwind change (Δw_x) in Figure 4.1c, a change in magnitude above 5 m/s showed an increased occurrence of subjective trigger events. Naturally, any crosswind non-perpendicular to the vehicle path would give a reading on the headwind measurements. Hence, the change in headwind (Δw_x) and flow angle ($\Delta\psi$) were presumably indirect effects of stability issues, while the change in crosswind (Δw_y) was a direct effect.

4.1.2 Vehicle motion response

The motion response data of the test vehicle was used to correlate the drivers' subjective assessment with certain vehicle motions, to formulate an objective measure for driving stability performance. Figure 4.2a shows the frequency of occurrence for the change in longitudinal acceleration (Δa_x) of the complete data set and the data prior to trigger events. 60 % of all data lie in the interval of 0.1 – 0.2 m/s^2, which was also the case for the trigger data. However, a discrepancy can be observed between the trigger data and the complete data set, indicating that a trigger was more frequent when the change in longitudinal acceleration was $\geq$0.2 m/s^2.

In general, the variations in lateral acceleration (Δa_y) proved to be greater compared to longitudinal acceleration (note the limits on the x-axis in Figure 4.2b). Hence, the driver was subjected to higher variations in lateral acceleration at normal straight-line driving. More interestingly, the discrepancy between trigger data and the complete data set was greater for lateral acceleration, indicating that this vehicle motion can be correlated with driving stability performance. For example, only 36 % of the complete data had magnitude variations greater than 0.5 m/s^2 while the number was 75 % for the data at the trigger events. The yaw velocity (ω_z) and lateral acceleration (a_y) are motions in the road plane and will later be shown to have a high correlation between them. Figure 4.2c shows that the change in yaw velocity ($\Delta\omega_z$) had the largest discrepancy between triggers and all data where 33 % of the trigger data varies >1.0 deg/s (compared to only 8 % of the complete data set).

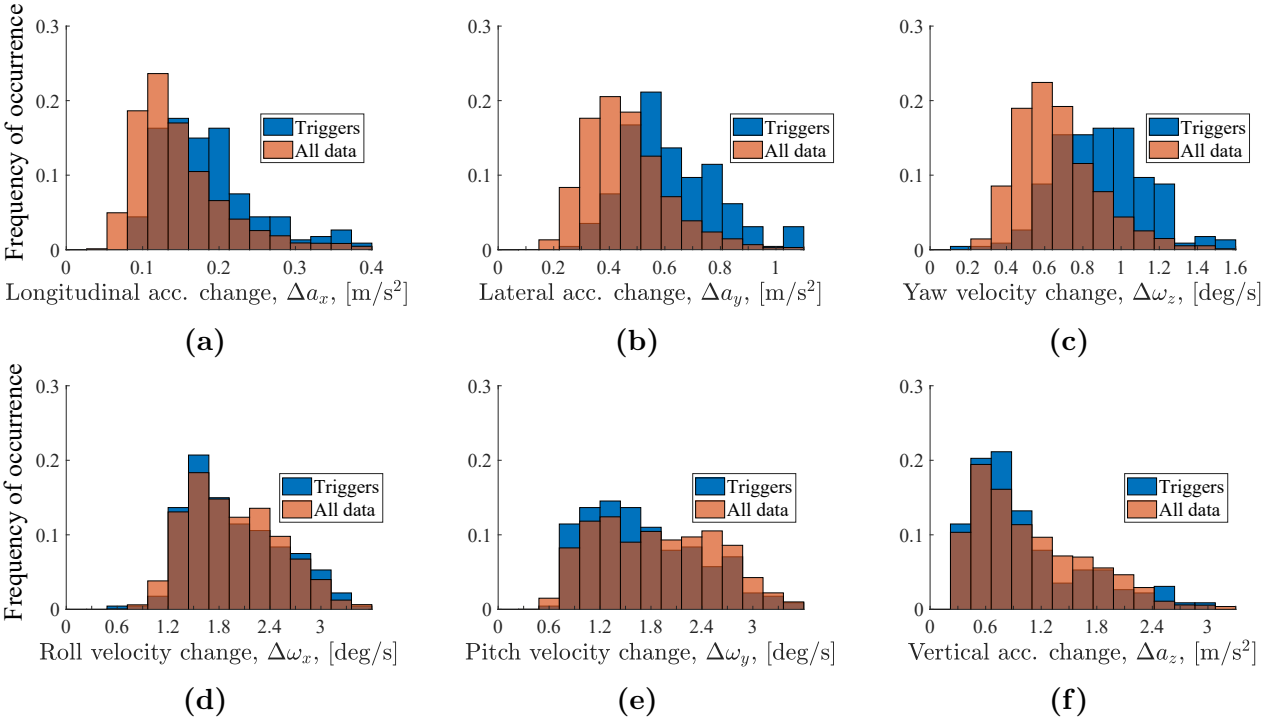

Figure 4.2: *The probability of occurrence distributions for six vehicle motion quantities, comparing the data at the trigger events to the complete data set.*

The roll velocity (ω_x), pitch velocity (ω_y) and vertical acceleration (a_z) had higher variations at normal straight-line driving compared to yaw velocity, longitudinal and lateral acceleration. According to Figure 4.2d, the change in roll velocity ($\Delta\omega_x$) had almost no discrepancy between the trigger data and the complete data set. Hence, using this analysis method, it could be concluded that large changes in roll velocity were not the cause of the drivers' subjective triggers. Similarly, no discrepancies could be seen for either the change in pitch velocity ($\Delta\omega_y$) or vertical acceleration (Δa_z) see Figures 4.2e and 4.2f. Consequently, even though roll velocity, pitch velocity, and vertical acceleration generally had higher magnitude variations compared to the other three vehicle motions, they did not correlate with poor driving stability performance. Oscillating vibrations from the road seems to be expected by the driver and were therefore not evaluated as exceptional.

In summary, high lateral acceleration and yaw velocity changes seem to correlate with lower crosswind sensitivity performance. The amplitude changes of these vehicle motion responses were combined to formulate a proxy measure for the stability performance. The combined measure uses an elliptic formulation of the amplitudes, see Equation 4.1, where Δa_y and $\Delta\omega_z$ were the configuration's amplitude measure for lateral acceleration and yaw velocity, respectively. Note that the units in Equation 4.1 should be [m/s^2] in Δa_y , [deg/s] in $\Delta\omega_z$ and that the formula is not claimed to be general for any driving nor to represent a physical quantity.

$$Y = \sqrt{2\left(\Delta a_y\right)^2 + \left(\Delta\omega_z\right)^2} \tag{4.1}$$

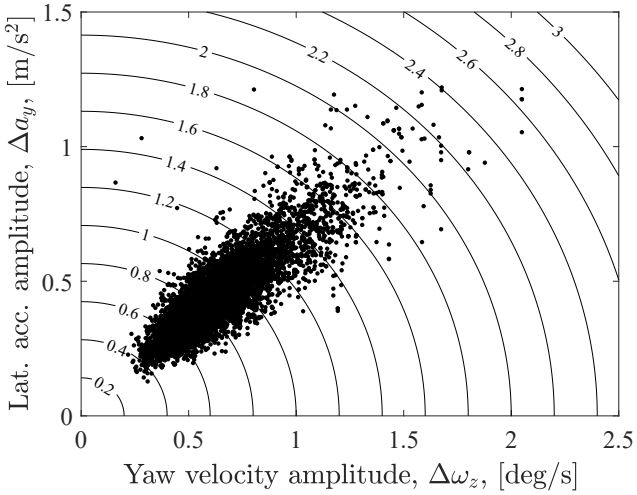

Figure 4.3: *The response amplitudes for the complete data set, with the objective proxy measure (Equation 4.1) visualised as contour lines.*

Figure 4.3 show the amplitude responses of the complete data set together with the objective proxy measure. The axes show the amplitude measures while the contour lines indicate the value of the objective measure calculated using Equation 4.1. The figure also shows the strong correlation between lateral acceleration and yaw velocity. The measure is designed to promote a low response for both vehicle motions.

4.2 Vehicle sensitivity

In Paper B, the vehicle's sensitivity to crosswind gusts was analysed using 1-way coupled numerical simulations between aerodynamics (QSD model) and vehicle dynamics (enhanced 3 DoF model), to find key vehicle parameters affecting the sensitivity.

4.2.1 Parametric analysis setup

A numerical design of experiments was created to perform a sensitivity study of vehicle dynamic and aerodynamic parameters. The study included 25 vehicle parameters and utilised the proxy measure for crosswind sensitivity (Equation 4.1) to evaluate the performance of each design. Sixteen of those were related to vehicle dynamics, having the prefix V in Table 4.1, and the nine aerodynamic parameters have the prefix A. The table gives the name, abbreviation, unit and investigated intervals between the minimum and maximum values. The nominal values were based on the existing vehicle and the intervals were selected from existing specifications and feasible spread for multiple vehicle types. Parameters V1-V7 capture the primary vehicle dynamic properties, such as wheel base (V1) and mass (V5). V8 is the input to the polynomial modelling of the lateral cornering stiffness of the tyre. V9-V16 are associated with suspension characteristics, i.e. kinematics and compliance (K&C) parameters. Side force steer (V9-V10) account for the additional steering of the suspension and steering system kinematics when side axle loads are applied, while the roll steer (V11-V12) do the same for the vehicle roll angle. Roll centre heights (V13-V14) and roll stiffnesses (V15-V16) were also included.

Table 4.1: *Parameters and their intervals investigated in the sensitivity study.*

No.	Parameter	Abbr.	Unit	Min	Max
V1	Wheel base	whlB	m	2.60	3.00
V2	Track width	trkW	m	1.45	1.75
V3	Centre of gravity height	CoGz	m	0.40	0.80
V4	Centre of gravity position, l_f/L	CoGx	1	0.40	0.55
V5	Vehicle mass	mass	kg	1500	2700
V6	Sprung mass moment of inertia (x)	inertx	kgm^2	400	750
V7	Mass moment of inertia (z)	inertz	kgm^2	2500	4500
V8	Normalised tyre lateral cornering stiffness	corStif	1/rad	20.0	30.0
V9	Side force steer, front	sStrFr	deg/kN	-0.15	0.01
V10	Side force steer, rear	sStrRe	deg/kN	-0.01	0.05
V11	Roll steer, front	rStrFr	deg/deg	-0.10	0.01
V12	Roll steer, rear	rStrRe	deg/deg	-0.01	0.06
V13	Roll centre height, front	rcFr	m	0.06	0.20
V14	Roll centre height, rear	rcRe	m	0.08	0.22
V15	Roll stiffness, front	rStifFr	Nm/deg	1200	3000
V16	Roll stiffness, rear	rStifRe	Nm/deg	1000	2500
A1	Side force coefficient gradient	side	1/deg	0.025	0.050
A2	Front lift coefficient at zero flow angle	fLift0	1	-0.050	0.050
A3	Front lift coefficient quadratic increase	fLiftq	$1/\mathrm{deg}^2$	0.0005	0.0015
A4	Rear lift coefficient at zero flow angle	rLift0	1	-0.100	0.050
A5	Rear lift coefficient increase at 1.25 deg	rLift1	1	0	0.010
A6	Rear lift coefficient increase at 3.75 deg	rLift3	1	0	0.070
A7	Rear lift coefficient increase at 7.5 deg	rLift7	1	0.010	0.070
A8	Roll moment coefficient gradient	roll	1/deg	0.008	0.011
A9	Yaw moment coefficient gradient	yaw	1/deg	0.006	0.011

The aerodynamic parameters were based on yaw sweep curves, where the coefficients of side force, roll moment and yaw moment often show a linear dependency on the flow angle [43]. Hence, the A1, A8 and A9 represent the linear gradient of the three coefficients, respectively. The front lift coefficient was modelled using; A2 to set the smallest value of front lift (at 0 deg flow angle), and A3 to control the quadratic increase of the coefficient at higher flow angles. Similarly, the rear lift coefficient was controlled with four parameters, where the first (A4) set the smallest value of rear lift and the following (A5-A7) manipulated the increase at higher flow angles. This modelling approximation of the yaw sweep curves was only used in the parametric study. Otherwise, the exact yaw sweep curves were used.

A total of 15 000 configurations were simulated using the commercial optimisation software ModeFRONTIER 2017R5. The software was used to generate a Latin hypercube sampling and calculate the significant main effects (with a 95 % confidence level using t-distribution).

4.2.2 Parametric sensitivity analysis

Figure 4.4 shows the significant main effects of all 25 parameters, for the three aerodynamic load cases (gust profiles). The longitudinal centre of gravity position (V4) had the highest main effect, based on the chosen intervals. The positive effect of 0.85 (profile 1) indicates that increasing V4, i.e. moving the centre of gravity (CoG) rearwards, increases the vehicle motion response to the crosswind and thus negatively affects vehicle stability performance. This effect was expected and has been observed in other studies [28, 38, 41, 42]. In general, it can be noted that each parameter's trend effect (sign) was persistent regardless of gust profile, although the magnitude and level of significance varied. To minimise the yaw velocity response, increasing vehicle mass (V5) and yaw moment of inertia (V7) proved beneficial. The figure also demonstrates the importance of wheel base (V1), tyre lateral cornering stiffness (V8), and finally, the axle side force steer gradients of the rear and front axles (V10 and V9). Although V9 and V10 had minor main effects, it was considered an interesting finding as it showed that suspension characteristics have the potential to influence stability when primary vehicle parameters cannot be altered.

For the aerodynamics, it is evident that the yaw moment coefficient gradient (A9) had an effect size comparable to the vehicle dynamic effect V4, while the gradient of the side force (A1) had a minimal effect. The driving stability in crosswinds can thus be improved by reducing the gradient of the yaw moment coefficient (C_{ym}), i.e. moving the centre of pressure (CP) rearwards (Figure 2.3).

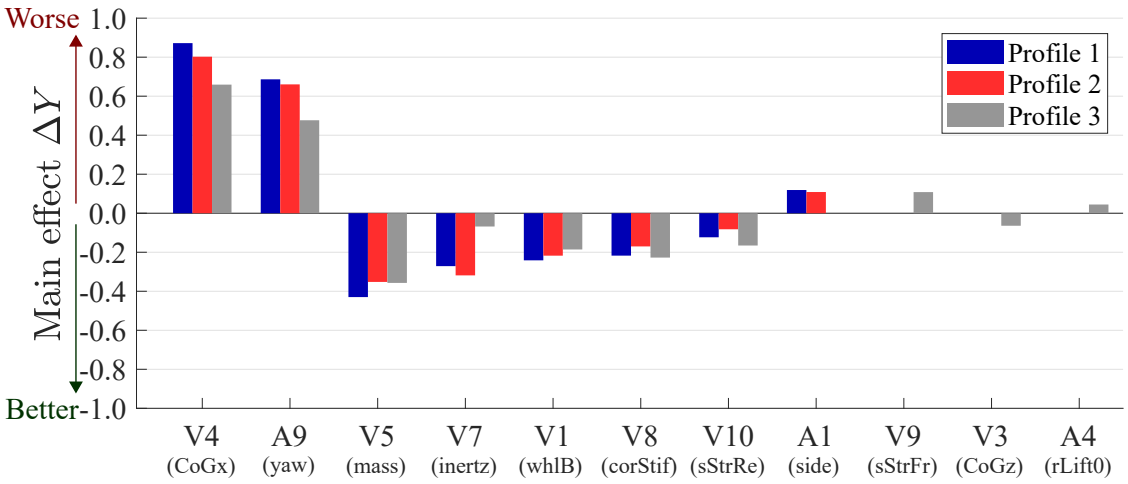

Figure 4.4: *The main effects of the significant vehicle dynamic and aerodynamic parameters combined.*

4.3 Driver sensitivity

The driving simulator enabled analysis of perceivable limits of gust strength and the opportunity to evaluate objective measures that correlate with the subjective perception of crosswind sensitivity. The study (Paper E) included 38 drivers, of whom 15 were expert drivers.

4.3.1 Driving simulator setup

The QSD model (Section 3.2.2) was used to approximate the aerodynamic forces and moments caused by the crosswind gusts and the road perpendicular lateral 2-way coupling (Equation 3.7) was implemented between aerodynamics and the vehicle dynamic model in the driving simulator. The general setup for the driving simulator studies is described in Section 3.3.1.

Test drivers were subjected to a randomised sequence of gusts where the crosswind magnitude varied between 1 m/s to 13.5 m/s. This was done at the three driving speeds of 120, 160 and 200 km/h, to evaluate the speed dependency of the objective measures. The drivers were asked to verbally report any gust they felt on a scale from 1 to 3. The driver inputs were logged and time stamped for post-processing. Gusts that passed unnoticed got the value 0 on the scale. The full subjective scale with descriptions per level can be seen below.

- **Trigger 0**: The vehicle was subjected to a gust, which the driver did not notice.
- **Trigger 1**: The driver noticed a gust, but assessed that no steering intervention was needed.
- **Trigger 2**: The driver noticed a gust, but assessed the vehicle as controllable with steering intervention.
- **Trigger 3**: The driver noticed a gust, but regarded the vehicle as difficult to control.

The motion experienced by the drivers was recorded using the inertial measurement unit (IMU) in the simulator's cockpit. The data sampling also included the steering wheel angle and steering wheel torque. Peak-to-peak delta values of these objective measures were taken at the gusts and subjective trigger events, to analyse the driver sensitivities objectively.

4.3.2 Wind gust strength sensitivity

The crosswind magnitude affects the vehicle response, but is not an objective measure that the driver can perceive. Nevertheless, analysis of the subjective correlation to the crosswind magnitude gives a good overview of relevant wind velocities for the range of subjective assessments. Figure 4.5 shows the trigger levels depending on the Beaufort wind scale, comparing gust profiles 1 and 3. The figure shows that the gusts corresponding to Beaufort number 1 appear to go mostly unnoticed (trigger 0) by the drivers. For Beaufort number 1, almost all profile 1 gusts pass unnoticed, while some of the profile 3 gusts were noticed (trigger 1) and needed driver intervention (trigger 2). Most of the Beaufort number 2 level gusts also passed unnoticed, while most drivers noticed the gusts of Beaufort number 3 and higher. This suggests that gusts of amplitude below 3 m/s are difficult to detect (based on the setup in the driving simulator), also agreeing with the on-road results in Figure 4.1a. At the strongest crosswind gusts above 10 m/s (Beaufort number 6), the majority of drivers assessed

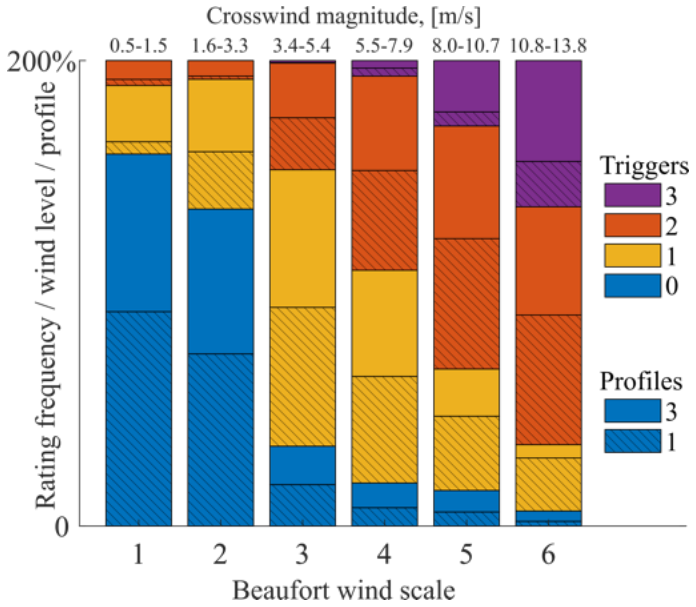

Figure 4.5: *The occurrence frequency of each trigger rating for crosswind gusts ranging from* 1 *to* 6 *on the Beaufort scale. Gust profiles 1 and 3 separately accumulate to* 100 % *for every crosswind level.*

that steering intervention was needed (triggers 2 and 3) and close to half of the profile 3 gusts were considered dangerous and difficult to control by the drivers. Generally, it seems that gust strengths above 8 m/s can be considered difficult to control when driving at high speeds. In addition, drivers seem more sensitive to profile 3 gusts. Interviews after the sessions revealed that profile 1 gusts were less severe since they helped to bring the vehicle back to the straight path due to the gust's switch from one side to the other. This was especially noticed by experienced drivers, who reacted less to the gusts, while some common drivers overreacted and worsened the vehicle reaction.

4.3.3 Subjective rating correlation to objective measures

Several objective measures were evaluated to find differentiable response levels per subjective rating. Furthermore, the predicted trigger values of an ideal measure should not change depending on driving speed. The best measures found are presented below.

Lateral acceleration

A high lateral gust response of the vehicle is known to negatively affect the subjective perception of crosswind sensitivity [18, 70, 74], which is also evident in Figure 4.6. The figure shows horizontal boxplots of the change in lateral acceleration (Δa_y) due to the gusts for each trigger level and driving speed. The results for common drivers are shown in Figure 4.6a, where it can be seen that the median (circled dot) lateral acceleration responses increase with higher trigger levels for each individual driving speed (colour). Although the ranges overlap, this shows a correlation between the lateral acceleration response and the subjective trigger value. However, Figure 4.6a also indicates that the lateral acceleration ranges are speed-dependent and vary within each trigger level. The lateral acceleration response can thus only be compared for the same speeds, when predicting the trigger levels caused by the set motion response.

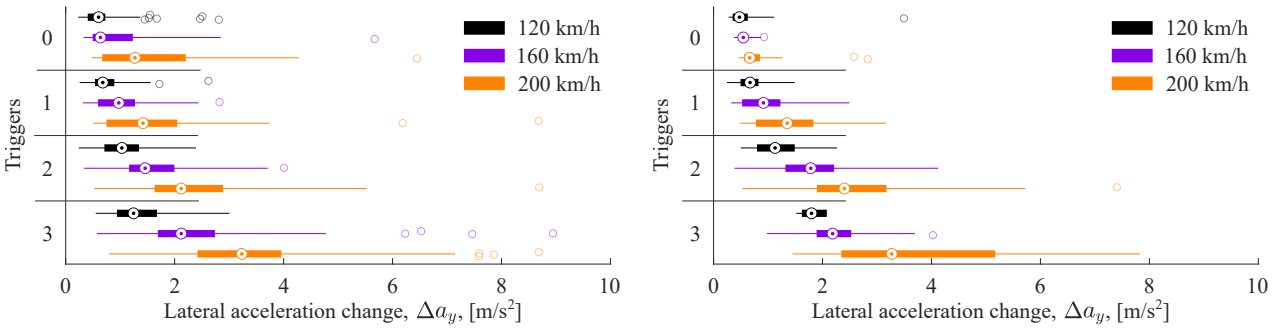

(a) *Common drivers.* **(b)** *Expert drivers.*

Figure 4.6: *Boxplots of the lateral acceleration response per trigger level, for (a) common and (b) expert drivers at* 120, 160 *and* 200 km/h. *The thick lines represent the interquartile range between the lower and upper quartiles with the circled dot as the median. Outliers are shown as circles.*

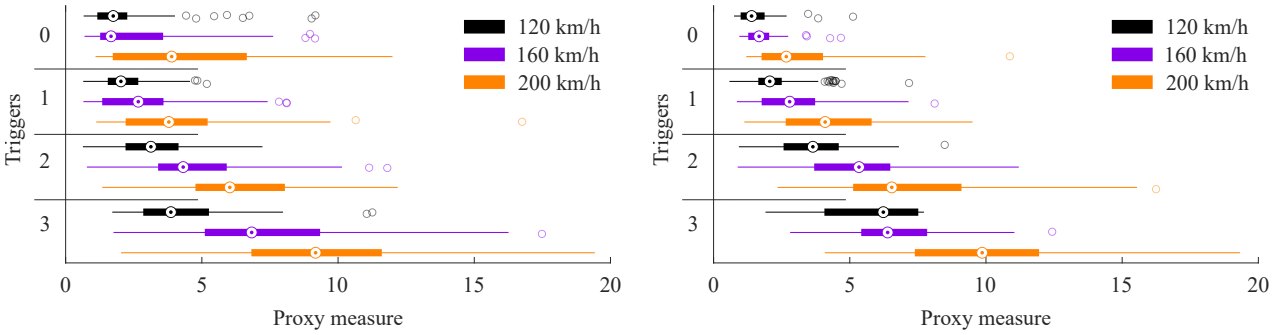

(a) *Common drivers.* **(b)** *Expert drivers.*

Figure 4.7: *Boxplots of the proxy measure (Equation 4.1) per trigger level, for (a) common and (b) expert drivers at* 120, 160 *and* 200 km/h. *The thick lines represent the interquartile range between the lower and upper quartiles with the circled dot as the median. Outliers are shown as circles.*

Figure 4.6b presents the results for the expert drivers. The expert drivers generally show less variance compared to the common drivers. Furthermore, for each driving speed, the expert drivers display less overlap in lateral acceleration response for each trigger level, especially when comparing driver types at 120 km/h. Hence, predicting the subjective trigger level based on lateral acceleration is more reliable for expert drivers. Nevertheless, the expert driver also shows the speed-dependency, so the predictions need adjustments for driving speed.

Yaw velocity

A lateral crosswind response of the vehicle will generate a change in lateral acceleration and yaw velocity. Paper E showed that yaw velocity, indeed, displays similar results as lateral acceleration, which agree well with the on-road sensitivity study (Figures 4.2b and 4.2c).

Proxy measure

The lateral acceleration and yaw velocity response were combined to a proxy measure (Equation 4.1) and used to analyse the vehicle sensitivity to crosswinds. Calculating this measure

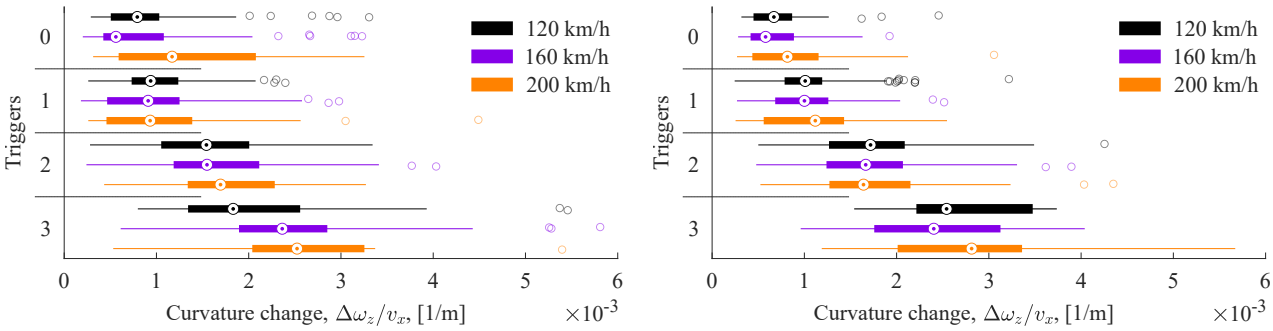

(a) *Common drivers.* **(b)** *Expert drivers.*

Figure 4.8: *Boxplots of the path curvature change per trigger level, for (a) common and (b) expert drivers at* 120*,* 160 *and* 200 km/h*. The thick lines represent the interquartile range between the lower and upper quartiles with the circled dot as the median. Outliers are shown as circles.*

from the driving simulator data results in Figure 4.7, displaying similar results as for lateral acceleration and yaw velocity. Namely, the proxy measure could differentiate the different trigger levels at a set driving speed, but the measure shows strong speed-dependency.

Path trajectory curvature

Interestingly, when analysing the data, it was found that scaling the yaw velocity with driving speed resulted in an almost speed-independent quantity while still enabling differentiation between trigger levels. This quantity represents the path curvature, ω_z/v_x, of the vehicle in m^{-1}. A vehicle travelling on the road in a straight path has no curvature, like the undisturbed driving scenario setup in the driving simulator. The path trajectory will change when the vehicle is subjected to strong crosswinds. Hence, this objective measure accounts for both the sensory lateral motion response of the vehicle and the visual feedback of deviating from the straight road. Figure 4.8 presents the results for using the path curvature as an objective measure for crosswind sensitivity. Expert drivers (Figure 4.8b) display essentially no speed-dependency and the median and interquartile values are separable by trigger level, although there are still overlapping ranges. In addition, this measure showed similar levels of data variance independent of speed for the trigger levels, unlike lateral acceleration and proxy measure, which had higher variance for higher driving speeds. Using the change in path curvature as an objective measure was less reliable for common drivers, as the data showed more overlap between trigger levels and a slight speed-dependency. The path curvature can be inversed into cornering radius for a more straightforward interpretation of the values. A curvature of $\omega_z/v_x = 2 \times 10^{-3}\,\mathrm{m}^{-1}$ would be equivalent to the vehicle suddenly starting to turn with the cornering radius of $R = 500\,\mathrm{m}$. Although the ranges for each trigger level overlap, it can be approximated that curvature variations above $\approx 3.5 \times 10^{-3}\,\mathrm{m}^{-1}$, are likely to correspond to a vehicle response challenging to control and, therefore, regarded as level 3 triggers. Furthermore, a change in curvature of $2 \times 10^{-3}\,\mathrm{m}^{-1}$ will likely require driver steering interventions (trigger 2 and 3), while values below $1 \times 10^{-3}\,\mathrm{m}^{-1}$ are likely undetectable or judged not to need any driver interventions.

5

High speed stability

This chapter focuses on high speed stability and describes how the performance is affected by wake dynamics and the balance of the lift forces. Two rear roof spoiler designs are first presented and discussed, covering the main findings of Paper C. These findings inspired alternative design solutions to improve the stability performance, which are included in Paper D together with windtunnel validation of the CFD results. An on-road evaluation of the design solutions and a subjective driver study from Paper E, comparing the importance of time-averaged lift forces versus wake dynamic fluctuations are also included.

5.1 Roof spoilers

Throughout the project, two versions of the roof spoiler were investigated. The two designs can be seen in Figure 5.1. The baseline spoiler demonstrated stability issues at high speeds, when evaluated on the test track, while the improved spoiler did not have any stability issues. This, even though the baseline spoiler had time-averaged front and rear lift force coefficients within the targets for high speed stability, which were inspired by the conclusions in [39]. The improved spoiler had even lower rear lift due to its more aggressive kick creating more up-wash in the base wake behind the vehicle. This design negatively affected the drag.

The results presented in this section are based on numerical CFD simulations, with the vehicle dynamic model coupling in Section 5.1.4.

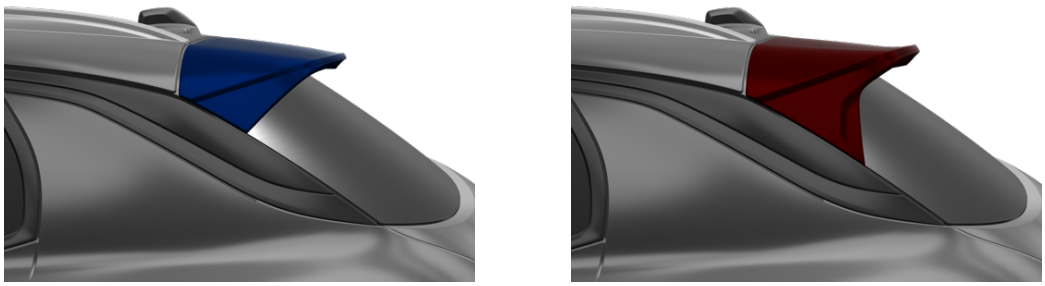

(a) *Baseline spoiler.* **(b)** *Improved spoiler.*

Figure 5.1: *Rendered images of the baseline spoiler (blue) and the improved spoiler (red), used in this thesis.*

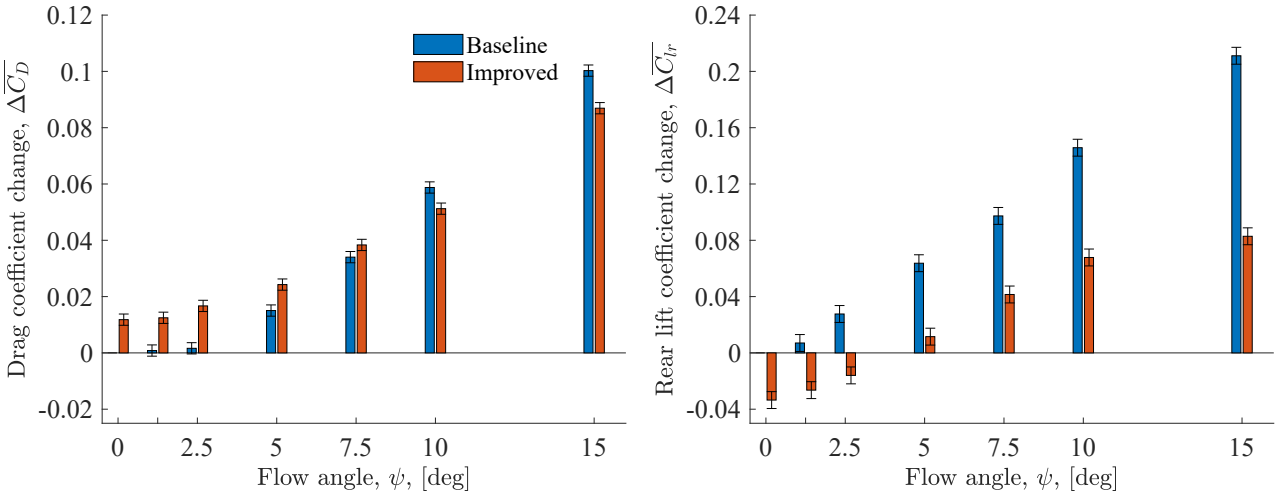

(a) *Drag.* **(b)** *Rear lift.*

Figure 5.2: *The influence of roof spoiler design and yawed flow angle on the aerodynamic coefficients, with the baseline spoiler at zero flow angle as reference. Numerical uncertainties were estimated based on averaging time, and the mesh and time step study in Paper C.*

5.1.1 Averaged forces and base pressures

Drag

The drag and rear lift force coefficients ($\overline{C_D}$ and $\overline{C_{lr}}$) of the two spoiler designs are presented in Figure 5.2 at a set of yawed flow angles, where the baseline spoiler at 0 deg is used as reference. The other time-averaged aerodynamic forces and moments are not presented since the simulations showed no significant differences between spoiler designs. Figure 5.2a displays the increased drag for the improved spoiler up until 10 deg yawed flow, where the improved spoiler displays lower drag and less sensitivity to yawed flow compared to the baseline. These differences in drag are mainly attributed to differences in base pressures, since the stagnation pressure at the front is unaffected by spoiler design. Figure 5.3 shows the base pressure coefficient for flow angles of 0, 2.5, 5.0 and 7.5 deg. The lower drag of the baseline spoiler at small flow angles is expressed as higher base pressures. The more aggressive kick of the improved spoiler creates a larger and more up-washed wake with lower base pressure. In the transition from 2.5 deg to 5.0 deg yawed flow, the baseline spoiler (Figures 5.3b and 5.3c) displays a rapid reduction in pressure on the slanted rear windscreen. The improved spoiler (Figures 5.3f and 5.3g) shows less pressure loss on the rear windscreen and even greater pressure on the rear windscreen at 7.5 deg (Figure 5.3h) compared to the baseline spoiler. Another noteworthy difference at 5.0 and 7.5 deg yawed flow is the baseline's low-pressure zone on the lower windward side of the rear windscreen, which is not observed for the improved spoiler.

Rear lift

The improved spoiler decreased rear lift compared to the baseline at all yaw angles, see Figure 5.2b. This rear lift offset between spoilers increases slightly for larger flow angles, further displaying the baseline spoiler's higher sensitivity to yawed flow. These differences can be estimated from the base pressures (Figure 5.3), focusing on the vertical location of the centre of pressure, where the improved spoiler has the high-pressure zone located further towards the

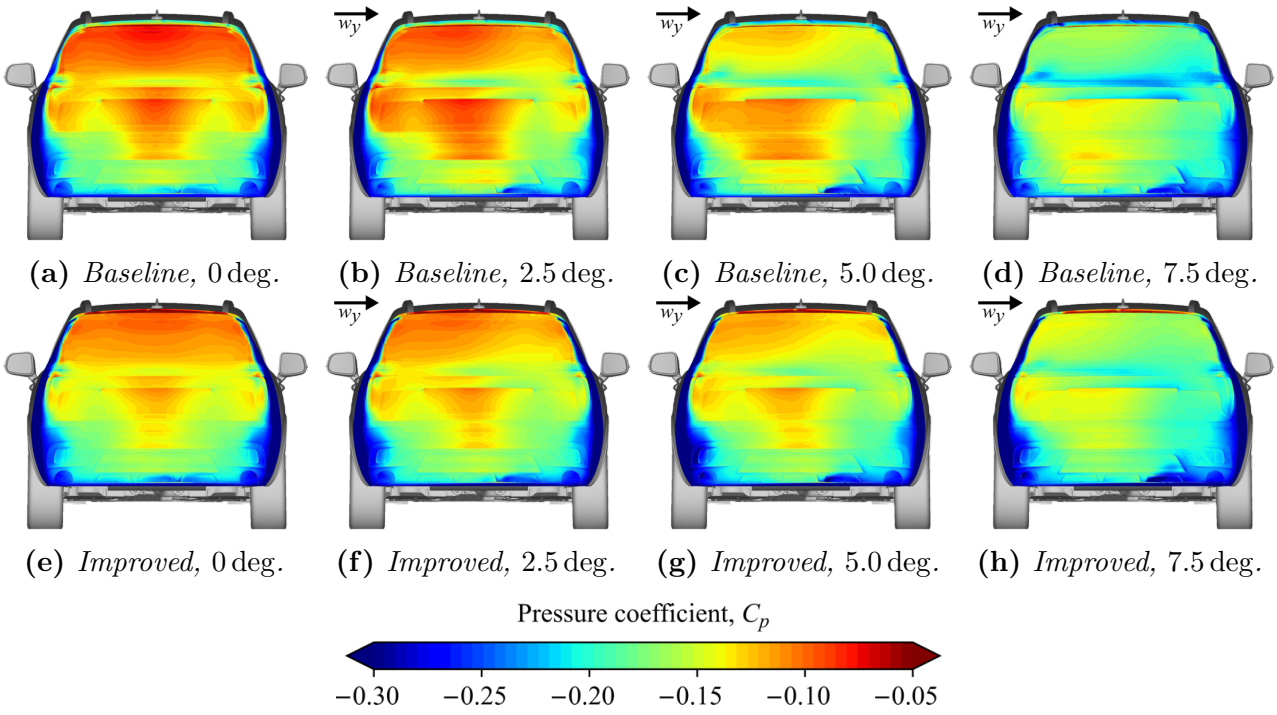

(a) *Baseline,* 0 deg. **(b)** *Baseline,* 2.5 deg. **(c)** *Baseline,* 5.0 deg. **(d)** *Baseline,* 7.5 deg.

(e) *Improved,* 0 deg. **(f)** *Improved,* 2.5 deg. **(g)** *Improved,* 5.0 deg. **(h)** *Improved,* 7.5 deg.

Figure 5.3: *Time-averaged base pressure coefficient,* $\overline{C_P}$*, for the two spoilers at* 0*,* 2.5*,* 5.0 *and* 7.5 deg *yawed flow angle.*

top of the base due to its more up-washed wake. An up-washed wake implies reduced flow velocity and increased pressure on the upper surfaces of the roof spoiler and increased velocity with lower pressure under the vehicle, which decreases the rear axle lift. A lower averaged rear lift, increasing the lift balance $(C_{lf} - C_{lr})$, is beneficial for driving stability, as discussed in Section 2.2.1. This suggests that the improved spoiler should perform better than the baseline. However, the improvement in high speed stability performance was greater than what could solely be explained by the average rear axle load increase of ≈100 N at 160 km/h and 0 deg yawed flow. Therefore, the chapter will continue analysing and discussing additional theories explaining the difference in the subjective high speed stability evaluations.

5.1.2 Averaged flow structures

The most significant differences in flow structures can be seen close to the slanted rear windscreen. Figure 5.4 show the vorticity, Ω_x, in x-normal planes located at 93 %, 95 % and 96 % of the vehicle length, for the 5 deg yawed flow condition. To indicate the wake size, the planes are clipped where the total pressure is greater than 0. As mentioned, the more aggressive kick angle of the improved spoiler creates a taller wake. The flow around the lower half of the vehicle looks almost identical while the upper part shows notable differences. The baseline configuration creates a strong anti-clockwise vortex structure (positive vorticity) at the windward side of the rear windscreen. The up-wash of the wake generates some out-flow at the mid-to-upper part of the inclined rear windscreen, while the inflow from the windward side occurs further down on the lower part of the windscreen and on the boot lid. The improved spoiler, having the higher windscreen pressure does not allow for this in-flow and weakens the vortex creating several smaller counter-rotating vortices instead. Furthermore, a clockwise

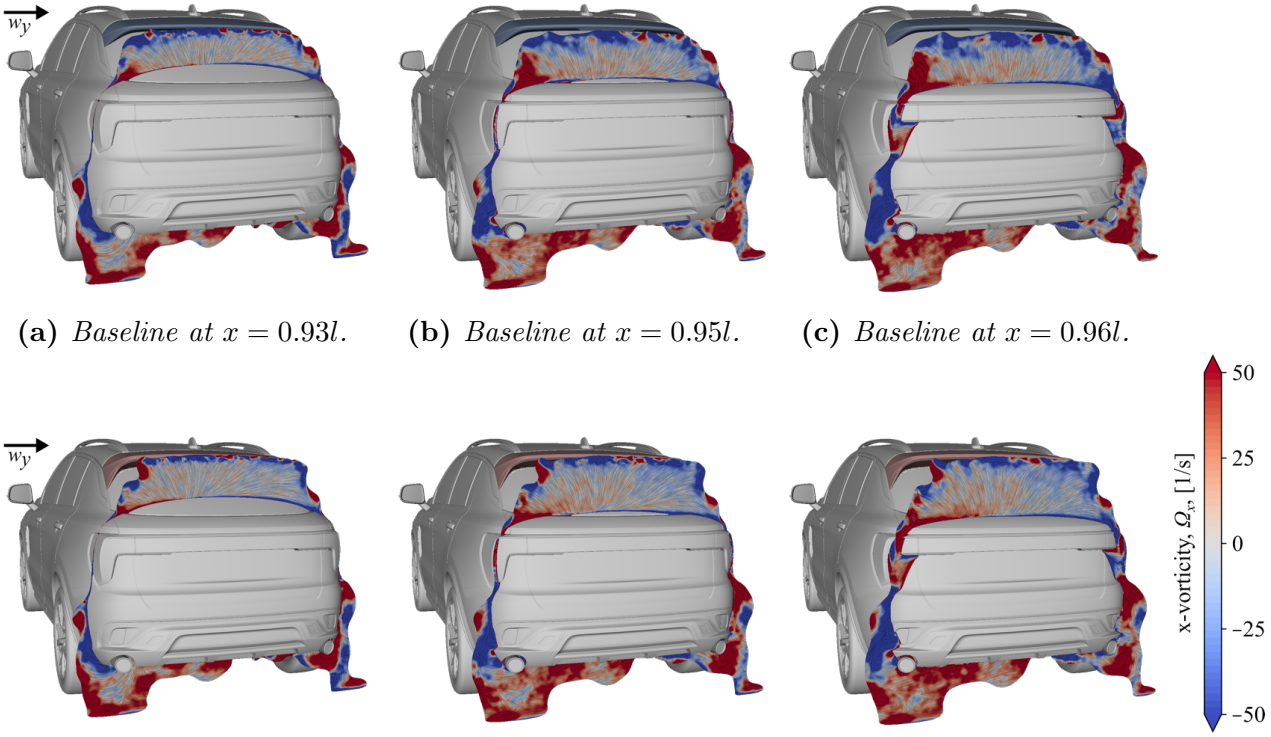

(a) *Baseline at* $x = 0.93l$. **(b)** *Baseline at* $x = 0.95l$. **(c)** *Baseline at* $x = 0.96l$.

(d) *Improved at* $x = 0.93l$. **(e)** *Improved at* $x = 0.95l$. **(f)** *Improved at* $x = 0.96l$.

Figure 5.4: *The time-averaged vorticity in x-normal planes, at* 5 deg *yawed flow. The values are clipped where the total pressure coefficient is larger than 0.*

vortex structure (negative vorticity) can be observed on the lower leeward side of the rear windscreen for the baseline (Figure 5.4c) but not as strong for the improved configuration (Figure 5.4f). Both these vortex structures could be traced on the base pressure as zones of low pressure in Figure 5.3c. The absence of strong vortex structures and the more up-wash dominated wake of the improved spoiler design explain its higher rear windscreen base pressure, Figure 5.3g, compared to Figure 5.3c. However, time-averaged results mask any transient phenomena that might affect the driving stability performance. These effects will be discussed next.

5.1.3 Unsteady forces and wake dynamics

The unsteady aerodynamic forces and wake dynamics were analysed in the Paper C study.

Rear lift fluctuations

The study showed that the baseline spoiler caused low-frequency rear lift fluctuations ($C'_{lr} = C_{lr} - \overline{C_{lr}}$) of high amplitude, especially in yawed flow conditions. Transforming the unsteady forces to the frequency domain is useful when comparing the strength of frequencies. Figure 5.5 displays the power spectral density (PSD) of the rear lift fluctuations in the frequency range of 0 Hz to 4 Hz, with focus on 0.5 Hz to 2 Hz known as a sensitive range for vehicle dynamics. The improved spoiler had frequency response levels insensitive to yawed flow up to the 7.5 deg, where a higher response at 0.5 Hz is observed. At 0 and 1.25 deg, the baseline spoiler had

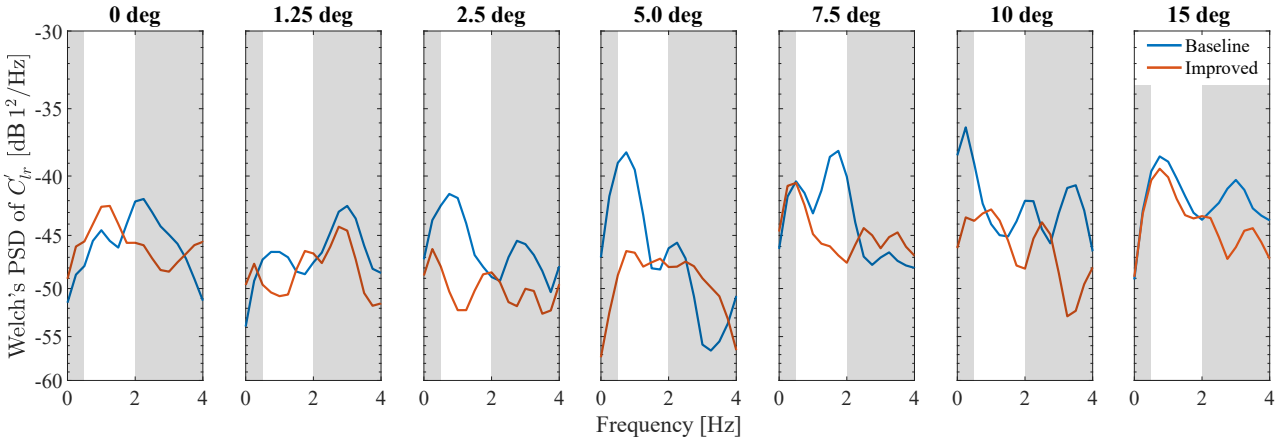

Figure 5.5: *Welch's PSD (power spectral density) frequency response of the rear lift fluctuations* ($C'_{lr} = C_{lr} - \overline{C_{lr}}$) *for the two spoilers at* 0, 1.25, 2.5, 5, 7.5, 10 *and* 15 deg *yawed flow angle. Using* 2 s *window size and* 90 % *overlap.*

a similar frequency response, but higher amplitude fluctuations for increased flow angles up to 15 deg where the improved spoiler also exhibited large low-frequency fluctuations. The largest difference happens at 5 deg flow angle, where the improved spoiler managed to keep the frequency response to similar levels as for the smaller flow angles, while the baseline configuration generated large low-frequency fluctuations close to 1 Hz. Note that negative PSD values can occur since decibel (dB) is a relative logarithmic measure. Hence, only the relative difference between values should only be considered. This means that the amplitude of the 1 Hz rear lift fluctuations of the improved spoiler were approximately 30 % of the amplitude for the baseline spoiler, for the 5 deg yawed flow case. The implications of these low-frequency fluctuations will be analysed further in Section 5.1.4, where vehicle dynamic effects will be discussed and related to real driving stability performance. The flow dynamics causing these fluctuations was of great interest to understand and possibly prevent this phenomenon. This will be discussed in the following.

Base wake dynamics

This section presents an analysis of the base wake using the base pressure gradient and conditional averaging of low and high lift modes for base pressure and skin friction, for the two spoilers and the 5 deg yawed flow angle. This angle was chosen as it displayed the largest low-frequency differences between the two spoilers.

The pressure gradients on the base were calculated using Equations 3.10 and 3.11 in the lateral and vertical directions, respectively. These time-dependent gradients were plotted as probability density functions (PDF) in Figure 5.6 to visualise the variance in the data and to determine if there is more than one state in the wake dynamics. Both spoilers had similar averaged lateral base pressure gradients, but the baseline spoiler had a larger variance, see Figure 5.6a. This means that the centre of pressure moves more laterally using the baseline spoiler, possibly affecting the lateral dynamics of the vehicle.

The improved spoiler creates a higher vertical base pressure gradient (indicating more up-wash and lower rear lift) with less variance, see Figure 5.6b. More interestingly, the improved spoiler

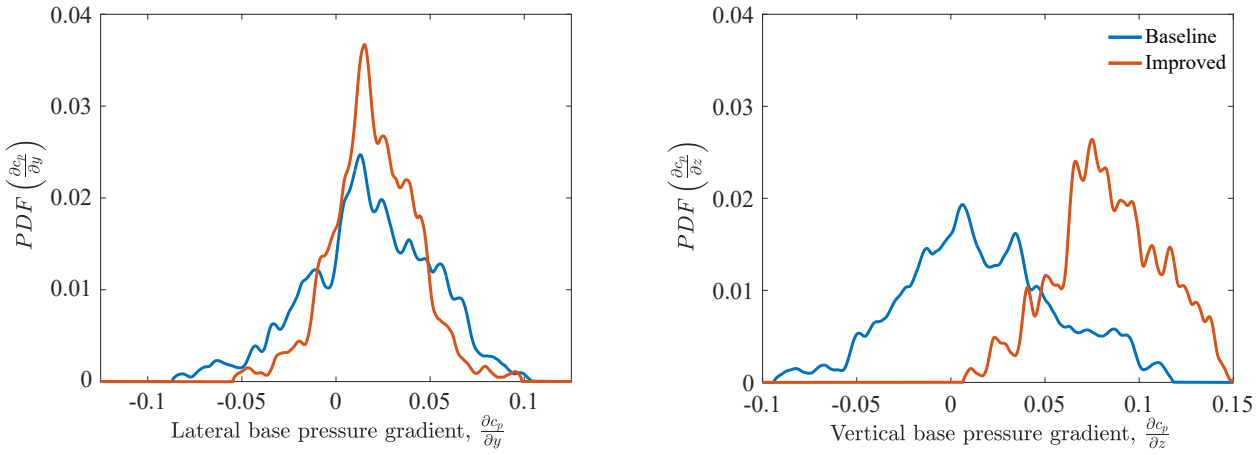

(a) *Lateral gradients.* **(b)** *Vertical gradients.*

Figure 5.6: *Average shifted histograms of the base pressure gradients (lateral and vertical) for two spoilers at* 5 deg *yawed flow.*

seems to have one flow state, while the baseline spoiler had two peaks of higher probability, indicating the existence of two dominant wake flow states (bi-stability). These states represent wake dynamics that generate high versus low rear lift forces, and can explain the differences observed in Figure 5.5.

To analyse the wake characteristics of the two states, a conditional averaging approach was utilised, based on the value of the rear lift force signal. When the rear lift was above its 75$^{\text{th}}$ percentile value, all unsteady base pressure, skin friction and flow field data were stored and averaged in a high (H) lift mode variable and similarly for the low (L) lift mode below the 25$^{\text{th}}$ percentile. The 75$^{\text{th}}$ and 25$^{\text{th}}$ percentiles were chosen to capture the wake mode extremes corresponding to the greatest rear lift fluctuations. The high (H) and low (L) rear lift modes of the baseline spoiler can be seen in Figure 5.7, where the base pressures show great differences. Firstly, the centre of pressure is located further up for the low rear lift mode. Second, the most considerable difference between the two modes is observed in the pressure on the rear

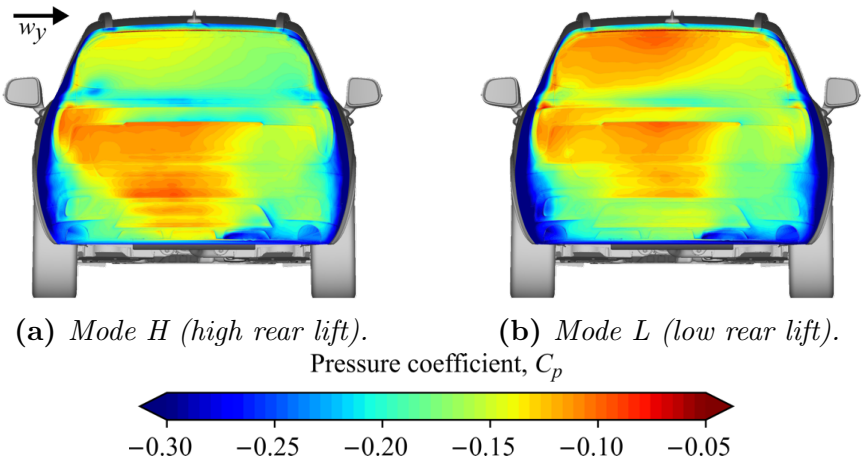

(a) *Mode H (high rear lift).* **(b)** *Mode L (low rear lift).*

Figure 5.7: *Conditionally averaged base pressures for the high (H) and low (L) rear lift modes, for the baseline spoiler at* 5 deg *yawed flow.*

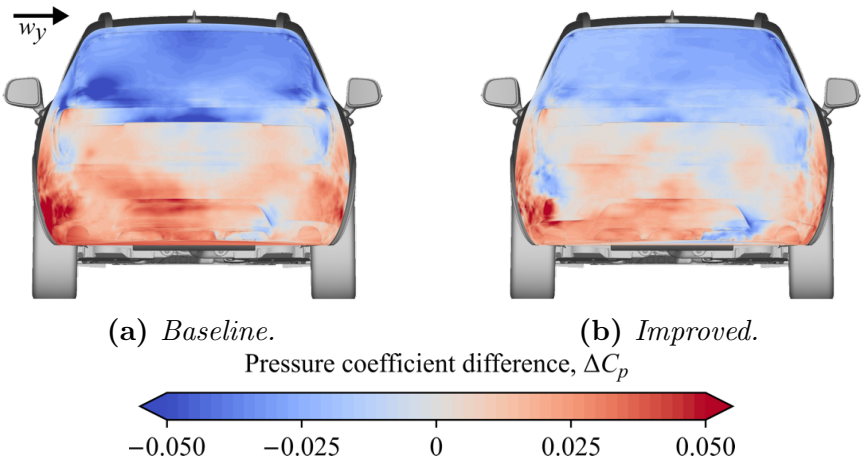

Figure 5.8: *Conditionally averaged base pressure differences between the high (H) and low (L) rear lift modes, for the two spoilers at* 5 deg *yawed flow.*

windscreen and beginning of the boot lid, where the high lift mode shows a local low-pressure zone on the lower windward side of the rear windscreen. This zone is caused by the vortex structure seen in Figure 5.4c temporarily attaching in this location at high lift modes. The low lift mode has a higher rear windscreen pressure, resembling the averaged values at smaller flow angles in Figure 5.3, while the high lift mode shows considerably lower rear windscreen pressure.

The vehicle equipped with the improved spoiler does have some rear lift force fluctuations. By displaying the pressure difference between the high and low lift modes, a comparison to the baseline spoiler could be created, see Figure 5.8. The general trend of a high lift mode with lower pressure on the upper half of the base and higher pressure on the lower half is seen for both spoilers. Nevertheless, the pressure difference between the upper and lower half is greater for the baseline spoiler. More noticeably, as seen above, the baseline spoiler has a low-pressure zone on the windward side of the rear windscreen at its high lift mode. The up-washed design of the improved spoiler seems to counteract the attached in-flow and the vortex formation on the slanted rear windscreen and prevents large pressure oscillations. A down-washed roof spoiler reduces windscreen pressure allowing temporarily attached in-flow which strengthens the vortex structure, as for the baseline spoiler.

5.1.4 Vehicle dynamic effects

The unsteady aerodynamic loads were applied to the enhanced 6 DoF vehicle dynamic model described in Section 3.2.3. Lift forces will directly influence the normal loads at the tyres and, consequently, the cornering stiffness at the front and rear axles. The variations in rear axle cornering stiffness due to the unsteady aerodynamics can be seen in Figure 5.9. Figures 5.9a and c show the results when modelling the vehicle as stiff, i.e. without any vertical dynamics. Evidently, the rear lift force fluctuations are transmitted to affect the cornering stiffness values. The higher low-frequency fluctuation amplitudes of the baseline spoiler are seen, whereas the improved spoiler fluctuates closer to the average value. Interestingly, when modelling the vertical dynamics of the vehicle with the axle spring and damper stiffnesses, the high-frequency

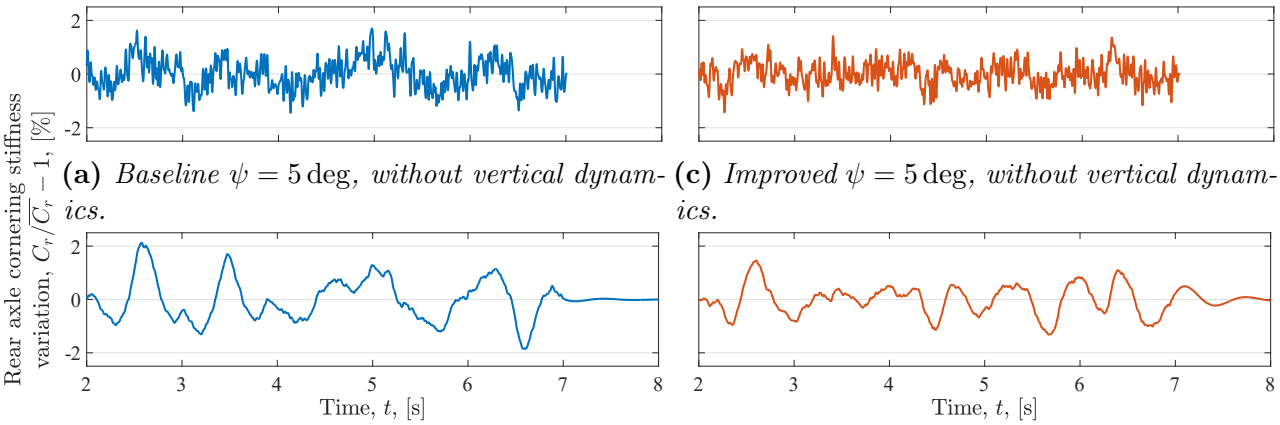

(a) *Baseline $\psi = 5\,\text{deg}$, without vertical dynamics.* **(c)** *Improved $\psi = 5\,\text{deg}$, without vertical dynamics.*

(b) *Baseline $\psi = 5\,\text{deg}$, with vertical dynamics.* **(d)** *Improved $\psi = 5\,\text{deg}$, with vertical dynamics.*

Figure 5.9: *The cornering stiffness variations for the two spoilers at $\psi = 5\,\text{deg}$, with and without modelling the vertical dynamics of the vehicle.*

fluctuations were reduced by the spring-damper system, while the low-frequency fluctuations increased, see Figures 5.9b and d. This, since the 1$^{\text{st}}$ natural frequency of the rear suspension lies close to the low-frequency aerodynamic fluctuations, thus intensifying the effect. The variations in cornering stiffness were smaller for the improved spoiler. Furthermore, its fluctuations of highest amplitude were closer to 2 Hz, compared with the high-amplitude fluctuations of 1 Hz of the baseline spoiler configuration.

The comparison in Figure 5.9 only included the two roof spoiler configurations at $\psi = 5\,\text{deg}$ flow angle. The effect of variation in cornering stiffness over a wide range of flow angles is presented in Figure 5.10. The variations between the 25$^{\text{th}}$ and 75$^{\text{th}}$ percentiles are shown in opaque colours, and the data between the 5$^{\text{th}}$ and 95$^{\text{th}}$ percentiles are presented in transparent colours, for the flow angle of 0, 1.25, 2.5, 5, 7.5, 10 and 15 deg. This indicates the cornering stiffness variations, in general and in maximum terms. First, it can be noted that the improved spoiler shows smaller variations for all flow angles investigated, both in general and maximum terms. Furthermore, the general variation of the improved spoiler was relatively independent of flow angle, while the baseline spoiler generated the highest variations at 7.5 and 15 deg flow angles. Finally, a maximum variation of up to $\pm 2\,\%$ was seen for the baseline spoiler. Naturally, a lower time-averaged rear axle lift force would be beneficial using this ratio measure. Nevertheless, the effect from the lower average rear lift of the improved spoiler was approximately one order of magnitude smaller than the differences seen in the figure. The higher fluctuation amplitudes were, thus, the primary cause of the differences seen. The cornering stiffness at the rear axle was presented to directly show the effects of the different aerodynamic characteristics of the rear lift force. However, this is not, by itself, a measure that the driver can notice. The balance between front and rear axle cornering stiffness determines the vehicle's understeering characteristics, which is related to the driver's perception of the vehicle. One measure of understeering is the distance, l_s, between the centre of gravity (CoG) and the neutral steering point (NSP), described in Section 2.2.1. A larger distance l_s translates to more understeering. This measure also accounts for the time-averaged differences in lift forces. Figure 5.11 shows the NSP position variations for the investigated flow angles. It is evident that the vehicle equipped with the improved spoiler yields more understeering at high speeds. Moreover, the

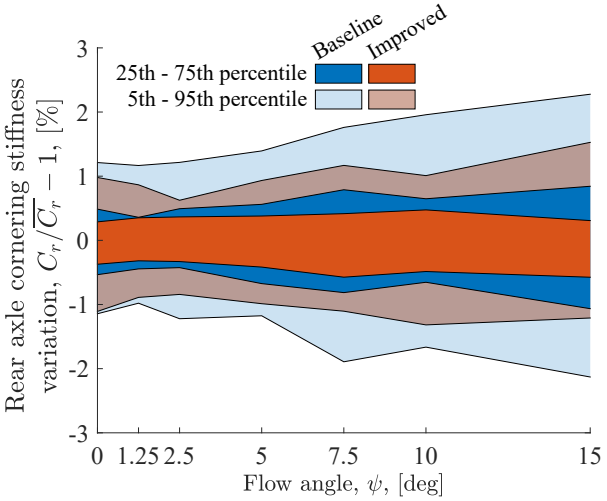

Figure 5.10: *The cornering stiffness variations for the two spoilers at* $\psi = 0$, 1.25, 2.5, 5, 7.5, 10 *and* 15 deg.

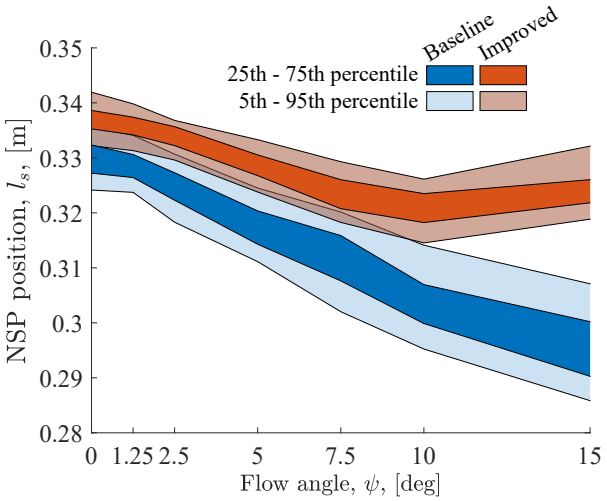

Figure 5.11: *The neutral steering point (NSP) variations, relative CoG, for the two spoilers at* $\psi = 0$, 1.25, 2.5, 5, 7.5, 10 *and* 15 deg.

baseline spoiler had an almost linearly decreasing understeering, as the flow angle increased, while the improved spoiler understeering was less sensitive to changes in flow angle. This means that the understeering characteristics of the baseline spoiler vary more at every set flow angle, but also that significant additional variations occur in conditions when the relative flow angle varies, which is the typical condition on the road. Driving in crosswinds also generates lateral aerodynamic loads. This, with varying neutral steering point position, means that vertical force fluctuations cause a lateral motion response of the vehicle that might be interpreted as vehicle nervousness by the driver.

5.2 Roof spoilers, diffusers and side spoilers

The findings in Paper C inspired additional configurations that could affect the wake dynamics (Paper D). Since the improved spoiler caused greater up-wash, an investigation on wake balance was conducted by creating three simplified diffuser designs to be used with the baseline spoiler. The three designs with diffuser angles of 0, 5 and 10 deg are shown in Figure 5.12. The temporary attachment of the strong windward side vortex on the slanted rear windscreen caused high wake dynamic fluctuations for the baseline spoiler configuration. A side spoiler geometry could hypothetically break this flow dynamics. Hence, the baseline spoiler was kept while investigating three alternative side spoiler designs, see Figure 5.13. All three designs were extended from the roof spoiler with large side coverage for the windscreen. Differences are seen on the lower part where the side spoilers attach to the boot lid, where an in-washed, a straight and an out-washed design was created to alter the vortex structure.

5.2.1 Averaged forces

The drag and rear lift coefficients of the additional configurations at 5 deg yawed flow are presented in Table 5.1, where the baseline spoiler is used as reference. As shown previously,

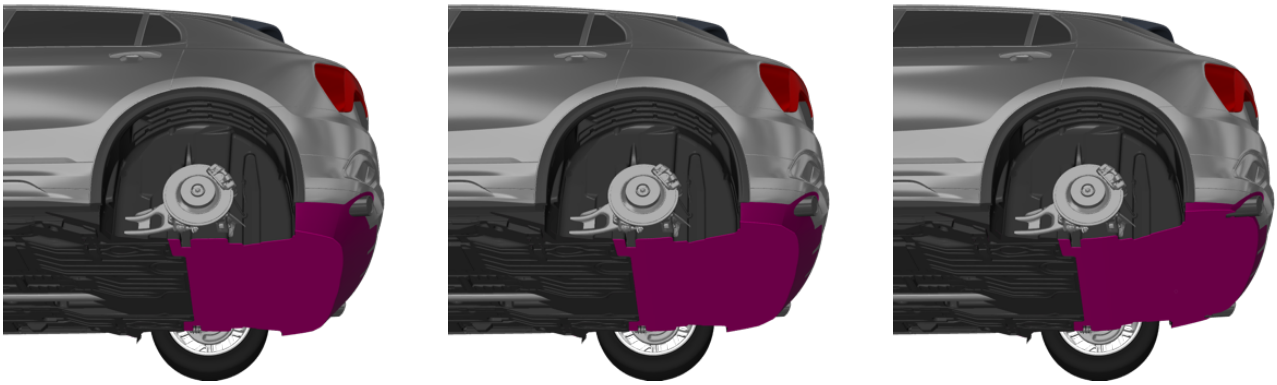

(a) 0 deg. **(b)** 5 deg. **(c)** 10 deg.

Figure 5.12: *Rendered images of the three diffusers (purple) on the test vehicle equipped with the baseline spoiler.*

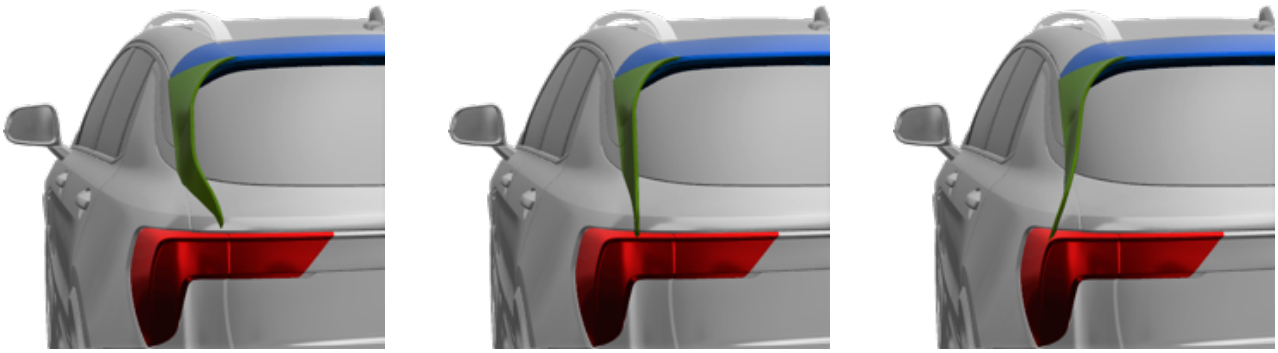

(a) *In-washed design.* **(b)** *Straight design.* **(c)** *Out-washed design.*

Figure 5.13: *Rendered images of the three side spoiler designs (green) using the baseline spoiler.*

the improved spoiler generates lower rear lift at the expense of increased drag due to its more aggressive up-wash. The flat (0 deg) diffuser increases the rear lift compared to the baseline spoiler, while the 5 and 10 deg diffusers gradually decrease the averaged rear lift. In addition, the 5 deg diffuser reduced drag slightly, while the other diffusers increased drag. The out-washed design of the side spoiler reduced rear lift, but increased drag since the separated area of the base is increased. In comparison, the straight side spoiler design shows slightly higher rear lift and lower drag, while the in-washed design had even lower drag and higher lift than the baseline spoiler.

Table 5.1: *The time-averaged delta drag and rear lift coefficients of the improved spoiler, the three diffusers and the three side spoiler designs, using the baseline spoiler as reference.*

	Roof spoilers		**Diffusers**			**Side spoilers**		
	Baseline	Improved	0 deg	5 deg	10 deg	In-wash	Straight	Out-wash
$\Delta C_D^{5^\circ}$	Ref.	0.009	0.003	-0.002	0.006	-0.003	0.002	0.005
$\Delta C_{lr}^{5^\circ}$	Ref.	-0.052	0.067	-0.005	-0.015	0.007	-0.021	-0.029

5.2.2 Unsteady forces and wake dynamics

Rear lift fluctuations

In Figure 5.14, the low-frequency rear lift fluctuations of the roof spoilers are evaluated against the additional configurations at 5 deg yawed flow. Using diffusers to alter the wake balance was ineffective in reducing the large rear lift fluctuations of the baseline spoiler. Nevertheless, the 10 deg diffuser performed better compared to the other diffuser angles, showing the beneficial effects of the increased up-wash in the wake.

Although all side spoiler designs were excessive (see Figure 5.13), the straight and the in-washed designs were unable to reduce the low-frequency rear lift fluctuations. They performed similarly to the baseline spoiler. Interestingly, the out-washed design could, on the other hand, reduce the rear lift fluctuations to levels equal to the improved spoiler, or lower. This, while having lower drag and higher lift compared to the improved spoiler. The out-washed side spoiler could therefore be an alternative design solution to improve high speed stability. The wake dynamics explaining these results will be discussed next.

Base wake dynamics

The pressure coefficient differences between the high (H) and low (L) lift modes are displayed in Figure 5.15, where a higher difference implies larger unsteady wake fluctuations. As previously noted, the baseline spoiler (Figure 5.15a) has greater vertical differences between the high and low rear lift modes, indicating more powerful vertical wake motions than the improved spoiler. Furthermore, the in-flow and windward side vortex appears to cause a low-pressure zone when attaching to the lower part of the windscreen. The strength of this zone was increased when using the flat (0 deg) and the 5 deg diffusers. Among diffusers, the 10 deg had the smallest pressure variations. Still, it showed similar base pressure variations as the baseline spoiler, although with a slightly weaker low-pressure zone at the windward side. This agrees with the results in Figure 5.14, where the 10 deg is the best diffuser, yet not as good as the improved spoiler.

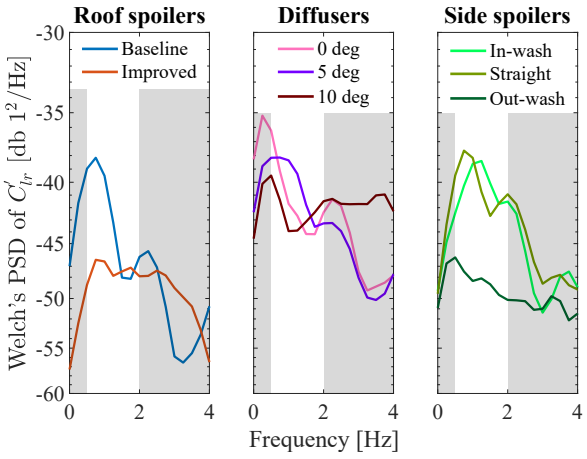

Figure 5.14: *Welch's PSD (power spectral density) frequency response of the rear lift fluctuations ($C'_{lr} = C_{lr} - \overline{C_{lr}}$) for the two roof spoilers, the three diffusers and the three side spoiler designs, at* 5 deg *yawed flow. Using* 2 s *window size and* 90 % *overlap.*

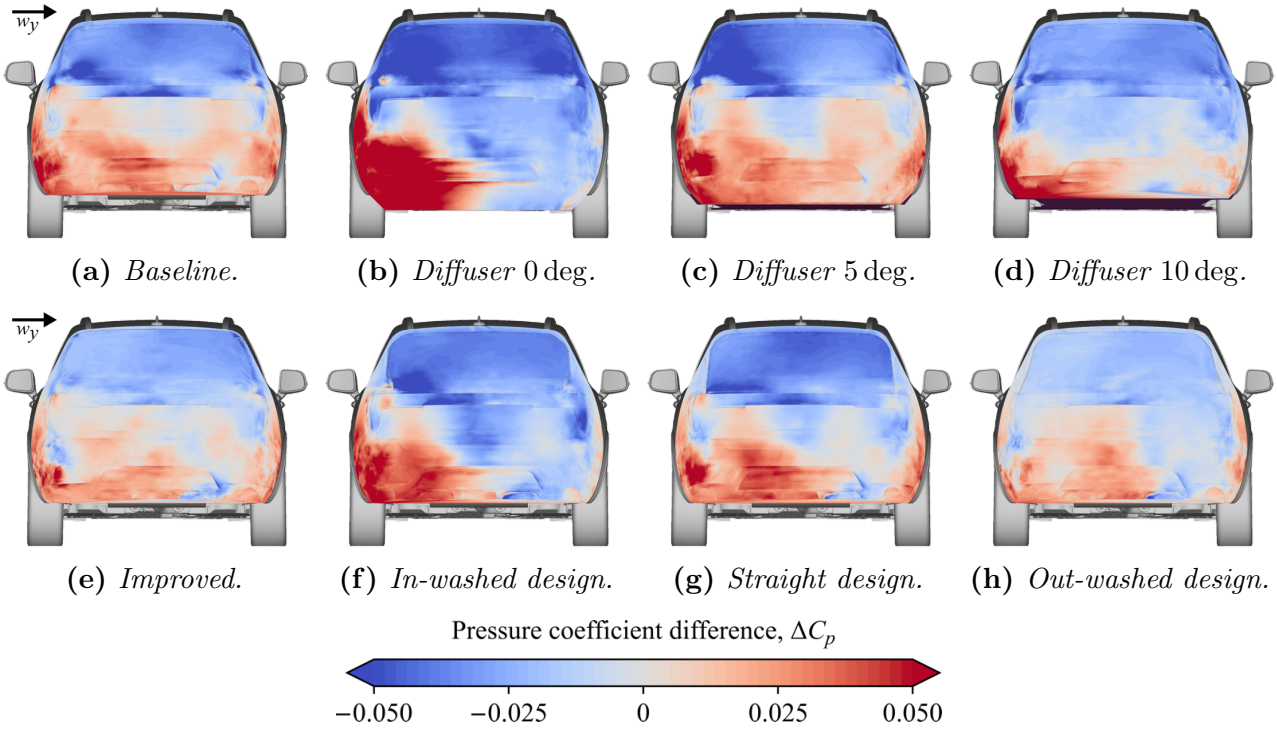

(a) *Baseline.* **(b)** *Diffuser* 0 deg. **(c)** *Diffuser* 5 deg. **(d)** *Diffuser* 10 deg.

(e) *Improved.* **(f)** *In-washed design.* **(g)** *Straight design.* **(h)** *Out-washed design.*

Figure 5.15: *Conditionally averaged base pressures difference between the high (H) and low (L) rear lift modes, at* 5 deg *yawed flow.*

The straight side spoiler did not break the bi-stable flow dynamics, nor did the in-washed design. Instead, the in-washed side spoiler was shown to guide the attached flow inwards feeding the clockwise vortex structure at the lower windward side of the windscreen, further demonstrating the significance of this flow structure. In agreement, the out-washed design counteracted the in-flow and the vortex structure which stabilised the wake and reduced pressure variations, as seen in Figure 5.15h. These pressure variations were slightly lower than the improved spoiler, resulting in the low rear lift fluctuations observed in Figure 5.14.

Figure 5.16 shows the velocity magnitude at the centreline in 5 deg yawed flow for the two roof spoilers and the out-washed side spoiler, where the red lines are manually positioned in the overall flow direction towards the base to qualitatively mark the wake balance. The time-averaged velocities are presented in Figures 5.16b, 5.16e and 5.16h, where the improved spoiler creates a taller and more up-washed wake. The improved spoiler's high and low lift modes show similar up-washed wake characteristics as its time-averaged data, indicating a relatively stable wake. Similarly, the out-washed side spoiler has a stable wake, but with less up-wash. In comparison, the baseline spoiler shows a balanced wake for its high lift mode (Figure 5.16a) and an up-washed dominated low lift mode (Figure 5.16c) similar to the wake of the out-washed side spoiler. The baseline spoiler's switching between balanced (mode H) and up-wash dominated wake (mode L) affects not only the pressure at the base but also the underbody and exterior flow. These wake motions cause the large fluctuations in the aerodynamic rear lift force discussed in Figures 5.5 and 5.14.

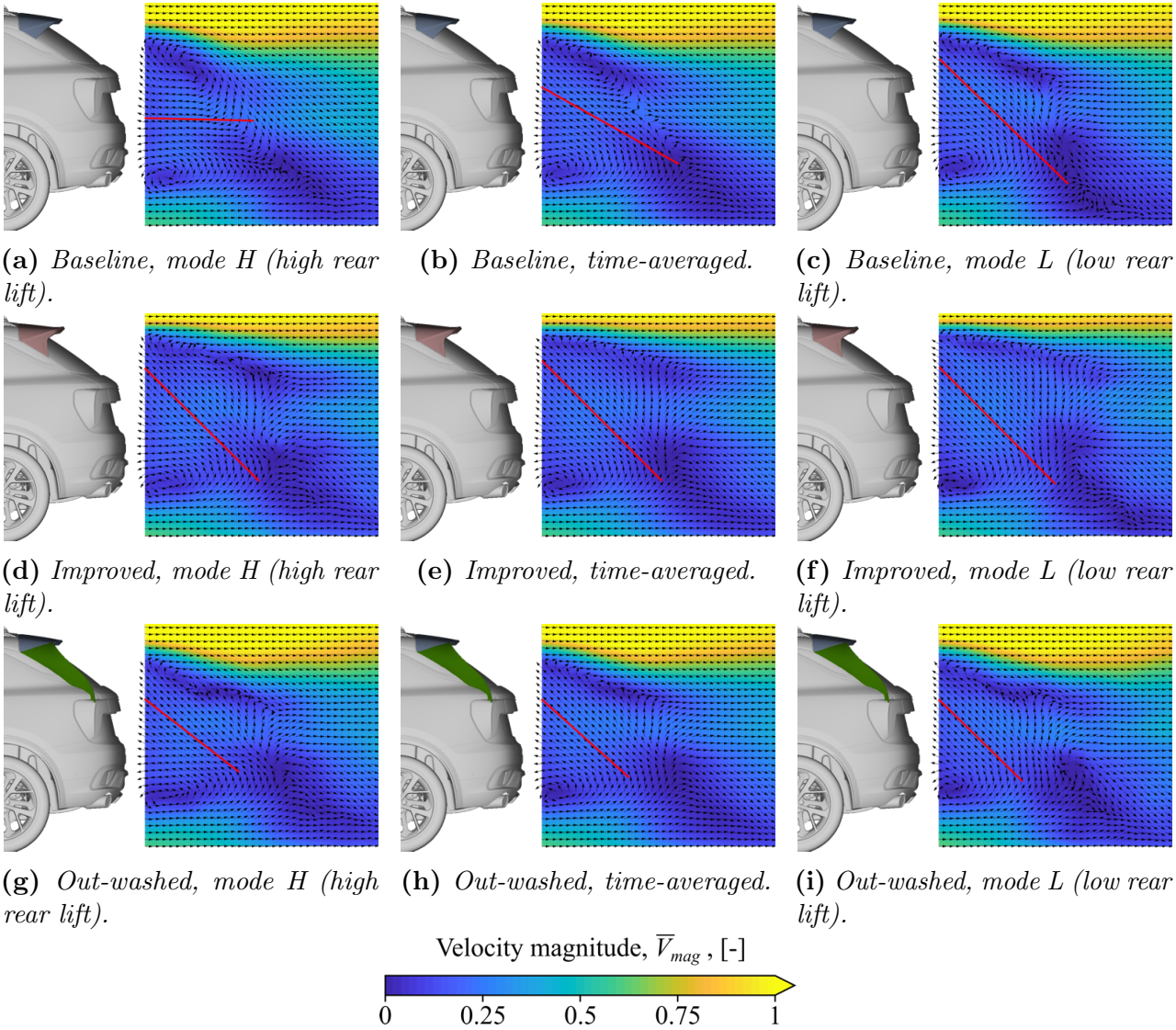

(a) *Baseline, mode H (high rear lift).* **(b)** *Baseline, time-averaged.* **(c)** *Baseline, mode L (low rear lift).*

(d) *Improved, mode H (high rear lift).* **(e)** *Improved, time-averaged.* **(f)** *Improved, mode L (low rear lift).*

(g) *Out-washed, mode H (high rear lift).* **(h)** *Out-washed, time-averaged.* **(i)** *Out-washed, mode L (low rear lift).*

Figure 5.16: *Conditionally averaged wake velocity fields for the high (H) and low (L) rear lift modes, at* 5 deg *yawed flow. Time-averaged velocity fields are included for comparison in the y-normal centreline planes. The red lines are manually positioned in the overall flow direction towards the base to mark the wake balance.*

5.2.3 Wind tunnel validation

The wind tunnel experiments confirmed the predicted time-averaged C_D and C_{lr} trends of the evaluated configurations; the baseline and improved roof spoilers and the out-washed side spoiler, see Paper D for more analysis of the averaged forces.

The unsteady forces could not be measured using the wind tunnel setup. However, these effects were estimated indirectly using unsteady base pressure measurements. The lateral and vertical base pressure gradients were calculated according to Equations 3.10 and 3.11. Figure 5.17b shows that the bi-stable vertical wake dynamics of the baseline spoiler was replicated experimentally at 2.5 deg yawed flow, compared to at 5 deg in the CFD simulations

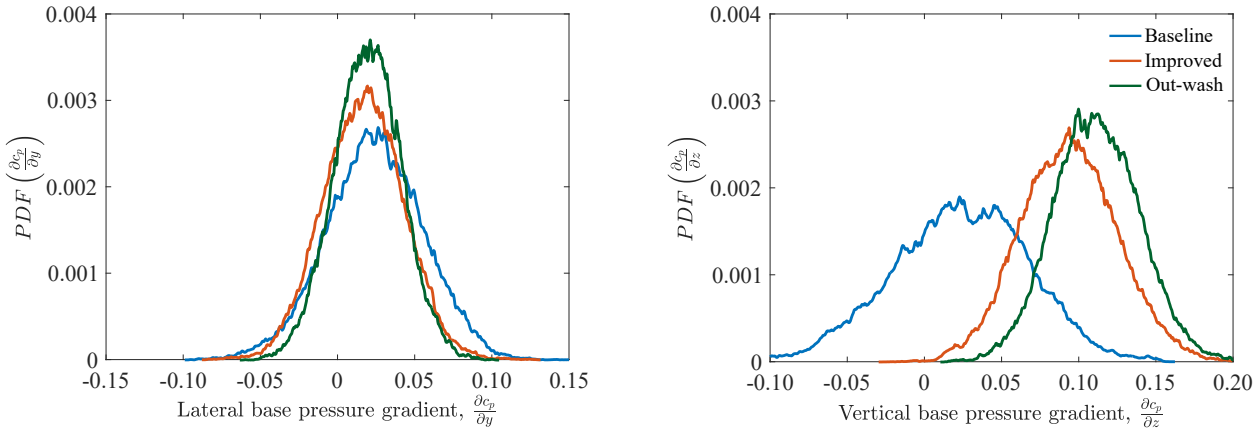

(a) *Lateral gradients.* **(b)** *Vertical gradients.*

Figure 5.17: *Average shifted histograms of the base pressure gradients (lateral and vertical) obtained from the wind tunnel experiment, in* 2.5 deg *yawed flow.*

(Figure 5.6b). For all investigated flow angles, the baseline spoiler had a lower vertical base pressure gradient with higher variance than the other two configurations. The out-washed side spoiler was shown to have the highest vertical base pressure gradient and the most stable wake laterally and vertically, indicated by the lowest variances in Figure 5.17.

The unsteady base pressures were conditionally averaged using a similar methodology as in the numerical setup. However, the experimental conditions were based on the 25^{th} and 75^{th} percentiles of the vertical base pressure gradient instead of the rear lift coefficient. This was regarded as acceptable since the two quantities are highly correlated. A low vertical base pressure gradient corresponds to a high rear lift, and vice versa. Figure 5.18 displays the pressure coefficient difference between the low and high modes of the vertical base pressure gradient. Without crosswind (0 deg), all three configurations have similar and stable wakes (Figures 5.18c, 5.18g and 5.18k). Setting the flow angle to 2.5 deg increases the pressure fluctuations for the baseline spoiler (Figure 5.18b). The low-pressure zone on the windward side of the slanted rear windscreen, discussed in the numerical results, is also observed experimentally. The design of the out-washed side spoiler created a stable wake in all investigated crosswind conditions. The improved roof spoiler demonstrated low pressure fluctuations at 2.5 deg yawed flow, while 5 deg flow caused higher pressure variations on the windward side of the rear windscreen. The improved spoiler could reduce the effect of this separating and re-attaching vortex structure, but not completely break the dynamics, as the out-washed side spoiler could. The baseline roof spoiler showed higher pressure variations and, thus, higher vertical wake fluctuations starting at lower flow angles. In addition, the baseline spoiler demonstrated pressure variations on the leeward side of the rear windscreen in Figure 5.18b. The -5 deg flow cases (Figures 5.18d, 5.18h and 5.18l) present relatively good symmetry of the wake dynamics, with the strongest effects occurring on the windward side of the base. The numerical results at 5 deg yawed flow (Figure 5.15) predict slightly lower pressure variations and wake fluctuations compared to the magnitudes shown experimentally in the wind tunnel.

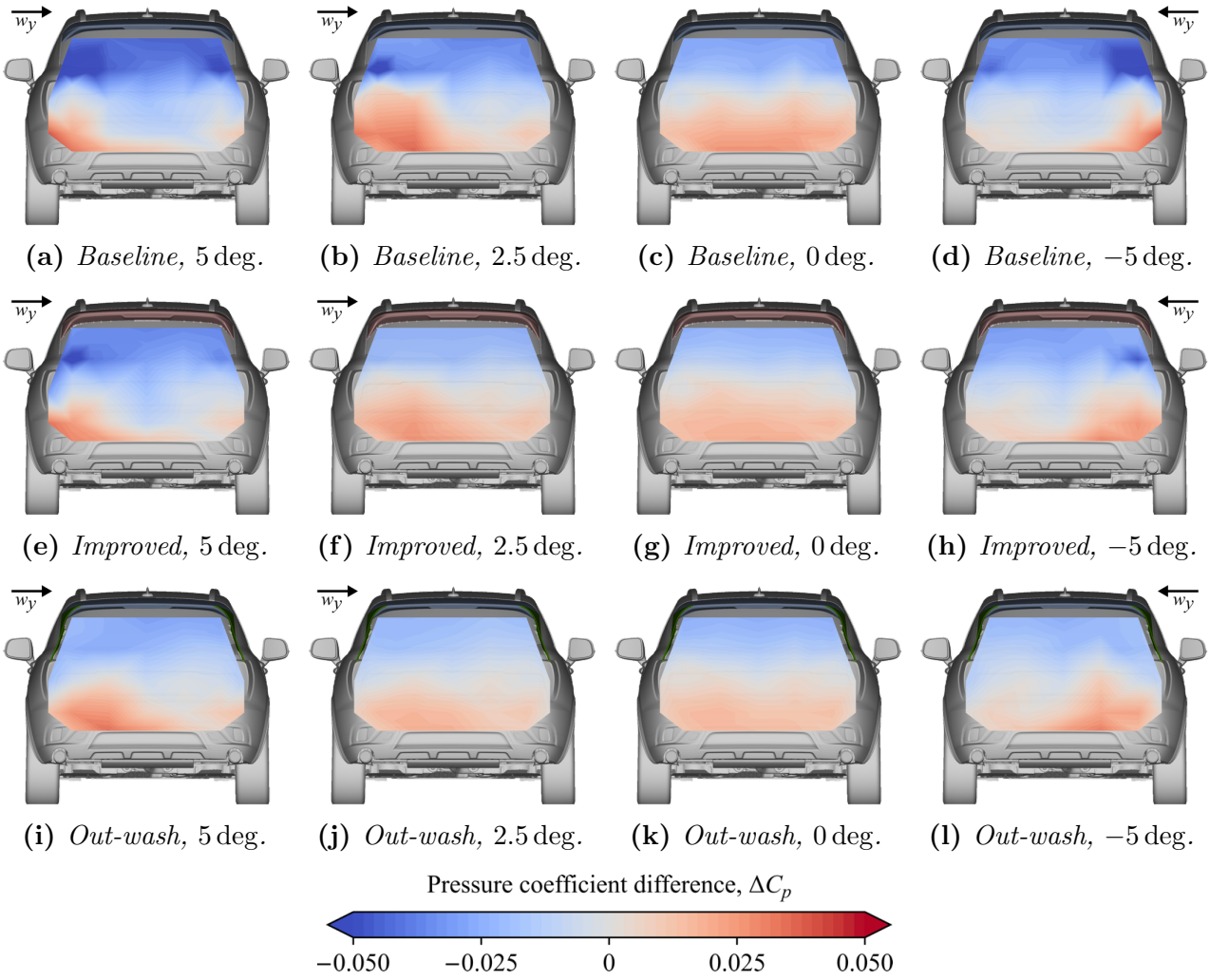

(a) *Baseline,* 5 deg. **(b)** *Baseline,* 2.5 deg. **(c)** *Baseline,* 0 deg. **(d)** *Baseline,* −5 deg.

(e) *Improved,* 5 deg. **(f)** *Improved,* 2.5 deg. **(g)** *Improved,* 0 deg. **(h)** *Improved,* −5 deg.

(i) *Out-wash,* 5 deg. **(j)** *Out-wash,* 2.5 deg. **(k)** *Out-wash,* 0 deg. **(l)** *Out-wash,* −5 deg.

Figure 5.18: *Conditionally averaged base pressure differences between the low and high base pressure gradient modes, obtained from the wind tunnel experiment.*

5.3 Driver perceived stability

Subjective high speed stability evaluations were performed on the test track (Paper D) and in the driving simulator (Paper E), by professional test drivers.

5.3.1 On the test track

The test track driving methodology was described in Section 3.3.2. The professional test drivers evaluated the baseline spoiler to have high speed stability issues. These were described as constant vehicle nervousness, with occasional more prominent lateral disturbances of the vehicle. The improved spoiler reduced nervous behaviour and prevented other unexpected occasional disturbances. The out-washed side spoiler (with the baseline roof spoiler) was also evaluated on the test track, since the numerical study predicted its wake dynamics to improve the driving stability performance. This was confirmed on the test track, as no stability issues were noted.

5.3.2 In the driving simulator

The driving simulator enabled subjective evaluation of the numerically simulated aerodynamic forces and moments. Furthermore, the forces and moments could be manipulated to test concepts difficult to evaluate on the test track.

Setup

The 5 s CFD simulated aerodynamic force and moment coefficients were stacked in time to create unsteady aerodynamic data for 3 min of testing. The study primarily included two aerodynamic configurations of the two rear roof spoilers seen in Figure 5.1. Three professional test drivers participated in and evaluated all configurations blindly. The study was set up to test the hypothesis that explains the differences in stability performance as an effect of vertical wake fluctuations. Therefore, four additional configurations were constructed by artificially manipulating the aerodynamic fluctuations of the two spoilers. The configuration numbering was based on the separation of the aerodynamic coefficients into time-averaged components, $\overline{C}$, and fluctuating components, C'. The first digit in the numbering corresponded to the averaged coefficients, where 1 used the baseline spoiler loads and 2 used the loads from the improved spoiler. Hence, configurations 1.1 and 2.2 were exactly the baseline and improved spoilers. All six configurations can be seen in Table 5.2. A special case can be seen in configurations 1.2_{lr} and 2.1_{lr}, where only the rear lift fluctuations, C'_{lr}, have been altered from the original configurations. In configuration 1.2, all force and moment fluctuations from the improved spoiler have been combined with the time-averaged load of the baseline spoiler, and vice versa for configuration 2.1.

Configuration assessment

All drivers identified configuration 1.1 as the worst in terms of high speed stability. The configurations were also evaluated in pairs by altering between the two while driving. The driver needed only to classify the best and worst in the pair. By analysing the results, it was possible to construct a list of the best-to-worst configurations, see Table 5.3. All drivers had the same relative evaluation of the configurations. As discussed, configuration 2.2 was expected to be the best and configuration 1.1 the worst. Unexpectedly, combining the aerodynamic forces of configuration 1.1 with only the rear lift fluctuations of configuration 2.2 (i.e. configuration 1.2_{lr}) was not perceived as more stable compared to vice versa (i.e. configuration 2.1_{lr}), even

Table 5.2: *The unsteady aerodynamic load case for each configuration.*

	Averaged coefficients, $\overline{C}$	Rear lift fluctuations, C'_{lr}	Fluctuations rest, C'_{rest}
Config. 1.1	Baseline	Baseline	Baseline
Config. 2.2	Improved	Improved	Improved
Config. 1.2_{lr}	Baseline	Improved	Baseline
Config. 2.1_{lr}	Improved	Baseline	Improved
Config. 1.2	Baseline	Improved	Improved
Config. 2.1	Improved	Baseline	Baseline

Table 5.3: *The resulting order from best to worst configuration when comparing every combination in pairs.*

	Configuration					
	Best			→		Worst
Driver 1	2.2	1.2	2.1_{rl}	1.2_{rl}	2.1	1.1
Driver 2	2.2		2.1_{rl}	1.2_{rl}		1.1
Driver 3	2.2		2.1_{rl}	1.2_{rl}		1.1

though the wake fluctuations mainly affect rear lift. Still, the effects of wake dynamics affected other forces and moments and the rear lift fluctuations of these two configurations were not in phase with the other fluctuations, making these modified configurations ambiguous to evaluate subjectively. Instead, changing all fluctuations (as in configurations 1.2 and 2.1) was a more realistic approach to compare the effects of the time-averaged forces and the wake dynamic fluctuations, making all fluctuations in phase and accounting for wake dynamics effects on all forces and moments. With this approach, it can be seen in Table 5.3 that driver 1 evaluated configuration 1.2 as the second-to-best and 2.1 as the second-to-worst configuration. Hence, the second digit in the configuration numbering was a good indicator of the high speed stability performance, implying that the differences in wake dynamics seem to be the primary cause of the spoiler's different on-road subjective ratings. This will be further investigated below.

Averaged versus fluctuating rear lift effects

The drivers compared the influence of the time-averaged and fluctuating rear lift components. The testing was based on configuration 1.1, as it was a known unacceptable configuration in terms of high speed stability. Drivers were first asked to notify when the setup became acceptable, while the time-averaged rear lift coefficient, $\overline{C}_{lr}$, was reduced. When the lowest time-averaged rear lift value was reached, the value gradually increased toward its original value and the drivers gave notice when the configuration performed unacceptable again. It was hypothesised that the stability issues could also be solved by damping the rear lift fluctuations. Hence, the drivers also evaluated the acceptable/unacceptable limits when scaling the rear lift fluctuations from 1 to 0 and back to 1. Finally, they evaluated the acceptable/unacceptable limits when both the time-averaged rear lift and the fluctuation scaling were altered simultaneously, to extend the investigated design space.

The results in Figure 5.19 have been averaged for all three drivers. The black circle represents configuration 1.1, used as a reference and considered unacceptable. The vertical axis shows adjustments to the averaged rear lift coefficient, which is usually the dimension used for the target setting. It is evident that exclusively decreasing the rear lift coefficient of configuration 1.1 can improve the performance of driving stability, although a considerable change of $\Delta\overline{C}_{lr} = -0.3$ was needed. The horizontal axle shows the scaling of low-frequency rear lift fluctuations, where configuration 2.2 is shown as a star. Configuration 2.2 had a slightly lower averaged rear lift coefficient, but the amplitudes of the low-frequency fluctuations were approximately 30 % compared to configuration 1.1. Damping the rear lift fluctuations solved the stability issues, even though the fluctuations of all other aerodynamic forces were still present. Hence, to improve the high speed driving stability of a vehicle, the combination of reducing the rear

lift fluctuations (i.e. wake dynamics) and decreasing the averaged rear lift is important. For reference, the square represents the averaged increase in the rear lift coefficient required to make the vehicle mathematically unstable, i.e. critically oversteered, at 180 km/h. This estimation was based on the eigenvalues of the linear system created from the vehicle dynamic bicycle model [36], discussed in Section 2.2.1.

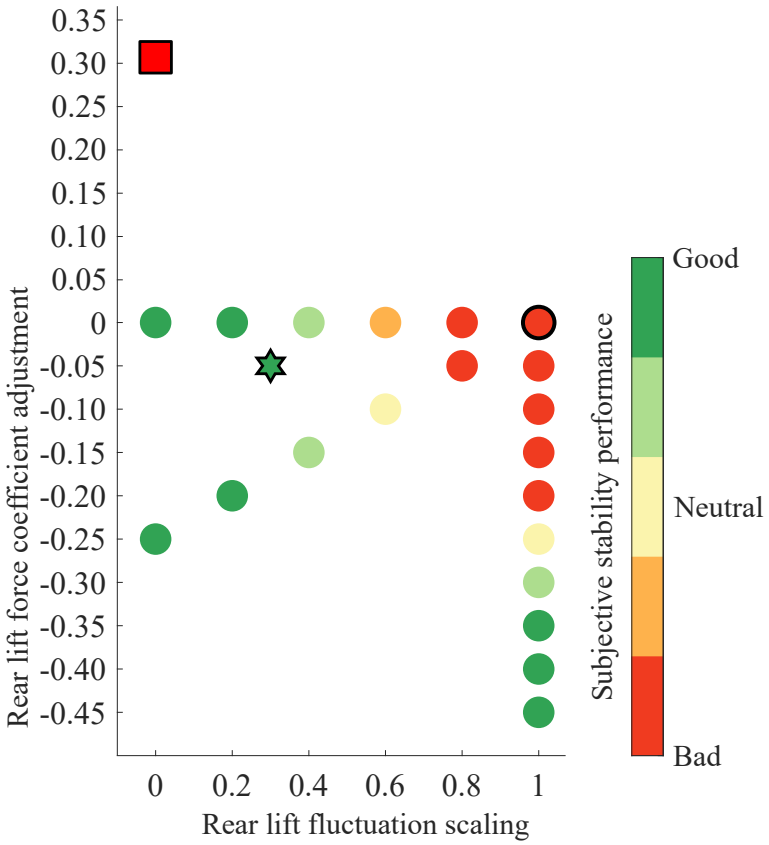

Figure 5.19: *The effects of time-averaged rear lift and rear lift fluctuation amplitude on the subjective high speed stability performance. The circle represents the baseline spoiler (configuration 1.1.), the star is the improved spoiler (configuration 2.2) and the square estimates the required rear lift coefficient making the linear system of the bicycle model unstable.*

6

Concluding remarks

The purpose of this thesis has been threefold. First, to understand the dynamics of the coupled aerodynamic/vehicle dynamic system during straight-line driving at high speeds. Secondly, to find measures for objectively assessing the driving stability performance and, thirdly, to investigate how virtual tools can be used in the assessment. This has been done experimentally on a test track, using a driving simulator and in a wind tunnel, and numerically with coupled simulation methodologies evaluating crosswind sensitivity and high speed stability.

The experimental study on the test track focused on correlating the drivers' subjective assessment of stability issues with wind loads and vehicle motions. To conduct this correlation, the test vehicle was instrumented with a wind probe on the roof, equipment for measuring the vehicle motion response and a subjective trigger button in the cabin. The drivers could press the subjective trigger when stability issues were experienced, generating a time stamp in the measured data. This setup enabled the objective correlation between higher changes in crosswind and worse stability performance, where the performance was already affected at crosswind changes of 5 m/s and above. Furthermore, higher variations in lateral acceleration and yaw velocity of the vehicle body correlated with an increased frequency of trigger events of stability issues. These motions were combined in an objective proxy measure for crosswind sensitivity, used in the numerical study to investigate vehicle parameters. Similar results were found when 38 drivers subjectively evaluated gust sensitivity in the driving simulator. Driver sensitivities to lateral acceleration and yaw velocity differed depending on driving speed, while the path curvature displayed speed-independent sensitivity levels for expert drivers. These measures can therefore be used to objectively rate the vehicles' sensitivities to crosswinds, while the latter can also be used for comparisons across vehicle speeds.

The numerical work developed a quasi-steady aerodynamic modelling approach accounting for the axle delay (QSD) when driving into crosswind conditions. The vehicle dynamic modelling was based on the bicycle model, enhanced by adding roll dynamics, non-linear tyre cornering stiffness and certain suspension characteristics. These models were 1-way coupled, as the 2-way coupling showed negligible differences, and validated before being used for the parametric study. The validation was based on experimental on-track data, where the virtual models accurately predicted the measured vehicle response based on the wind and driver steering response. The parametric study showed that to reduce the lateral motion response to crosswinds, the longitudinal position of CoG should move forward, while the aerodynamic yaw moment should be reduced (equivalent to moving the CP rearward). Other significant parameters were vehicle mass and wheel base, where higher values were found beneficial. However, these primary

parameters affect many other vehicle attributes and may not be realistic solutions to improve driving stability performance. Fortunately, the study also concluded that certain tyre and suspension characteristics could improve the stability performance at high speeds. The balance of the side force steer gradient between the front and rear axle along with the tyre cornering stiffness had a significant effect on the vehicle response, although the effects were much smaller than those of CoG and the aerodynamic yaw moment.

The wake dynamic effects on high speed stability under yawed flow conditions were investigated for two variants of an SUV's roof spoiler: a baseline spoiler known to induce subjective stability issues and an improved spoiler that solved them. The analysis linked the unsteady wake dynamic effects and the low-frequency (<2 Hz) fluctuations of rear axle lift with the vehicle handling characteristics. Professional test drivers could notice the same high speed stability phenomena in the driving simulator as those found on the test track and correctly differentiate the two spoilers based on these fluctuating aerodynamic loads. The CFD and wind tunnel study demonstrated a vertical base pressure gradient indicating bi-stable wake dynamics for the baseline spoiler design. It was further concluded that this coincided with vortex structures occasionally re-attaching on the lower sides of the rear windscreen, creating a vertical bi-stable wake. The up-washed design of the improved spoiler prevented this re-attachment of vortex structures, thus creating a more stable wake and reducing low-frequency lift fluctuations. Alternative diffuser and side spoiler designs evaluated with the baseline further defined the flow dynamics of the bi-stable wake and showed that the out-washed side spoiler design could also create a more stable wake, improving the high speed stability performance. This was later confirmed in the wind tunnel and on the test track, where the out-washed side spoiler was rated on par with the improved spoiler, while having a lower drag penalty. From the above, it can be concluded that the high speed stability performance can be estimated virtually using unsteady CFD simulations (or experimentally in a wind tunnel), by analysing the wake dynamics and rear lift forces. Additionally, the subjective assessment using a driving simulator can complement the on-road testing in early design phases.

The benefit of a higher lift balance between the front and rear axles is well known. Large negative lift balance values applied via the cornering stiffness of the linear bicycle model create a mathematically unstable system at high speeds. This indicates the importance of rear lift, although unrealistic values are needed to make a passenger vehicle mathematically unstable. A study in the driving simulator compared the effects of time-averaged rear axle lift (affecting lift balance) and the impact of the fluctuating wake dynamics. Lower average rear lift values were concluded to improve high speed stability performance, as expected. Moreover, the fluctuation levels of the rear lift were shown to be equally important. Thus, an important conclusion of this work is that high speed stability issues can be solved by either decreasing the averaged rear lift coefficient, or by managing the wake dynamics to reduce the rear lift fluctuations, preferably both.

6.1 Outlook

In this work, the vertical wake dynamics of an SUV equipped with a roof spoiler design was shown to affect the straight-line driving stability performance at high speeds. The numerical and experimental investigations were limited to one vehicle model. Therefore, it is recommended

to investigate other production vehicles known to exhibit bi-stable wake dynamics for their high speed stability performance. Correspondingly, the wakes of vehicles with poor stability performance should be analysed to further explore the effects of unsteady aerodynamics on vehicle handling and stability. This, in combination with further understanding the wakes of streamlined low-drag vehicles, would pose an interesting multi-objective optimisation problem.

The crosswind sensitivity analysis was primarily focused on crosswinds of a single time scale (and length scale). It would be of interest to extend the virtual tools by assessing the aerodynamic admittance (transfer function) at a frequency spectrum and combining the response of the complete system. This would require the development of a suitable human-like driver model to be included in the system. Furthermore, autonomous driver models could be interchanged with the human models to evaluate differences and improve the autonomous algorithms for highway driving in crosswinds. Autonomous steering can also lead to an additional set of design parameters (control algorithms and their parameters), compared to the traditional (mechanical and geometric) vehicle dynamics and aerodynamics design parameters.

7

Summary of papers

7.1 Paper A

Quantitative High Speed Stability Assessment of a Sports Utility Vehicle and Classification of Wind Gust Profiles

This paper is focused on finding realistic aerodynamic load cases for straight-line driving stability at high speed. In addition, the study aimed at correlating the drivers' subjective assessment of poorer stability performance to quantitative objective measures of the vehicle body motion. The experimental work was performed on the high speed track at Hällered Proving Ground using the compact SUV. The vehicle was instrumented with a wind probe, equipment for measuring the vehicle motion and a trigger button for the drivers' to note issues with the driving stability performance. The correlation between the subjective perception of stability issues and the change in lateral acceleration and yaw velocity is shown in the paper. Also, it is shown that crosswinds seldom generate flow angles above 10 deg at high speed driving. Nevertheless, already weaker crosswinds of ± 5 m/s (± 6.4 deg at 160 km/h) deteriorated the driving stability, indicating the importance of studying crosswinds sensitivity. The paper mathematically defines a set of typical crosswind gusts.

7.2 Paper B

High speed driving stability of road vehicles under crosswinds: an aerodynamic and vehicle dynamic parametric sensitivity analysis

Findings of Paper A were used to develop a virtual assessment of driving stability using coupled simulation tools. The crosswind gust profiles were used in the aerodynamic modelling and the correlated vehicle motions were used in a proxy measure for crosswind sensitivity. By comparing three methods of modelling the aerodynamic response, it is shown that the flow delay between the axles when driving into crosswinds is important. The paper presents a quasi-steady model which accounts for this. Furthermore, the level of complexity needed to assess crosswind stability in the vehicle dynamic models is investigated. Finally, the paper includes a parametric study of the coupled simulation model. The study highlights the importance of the longitudinal centre of gravity position and the aerodynamic yaw moment coefficient. Nevertheless, other parameters were also significant, including some tyre and suspension characteristics.

7.3 Paper C

Base wake dynamics and its influence on driving stability of passenger vehicles in crosswind

This paper numerically investigates the base wake dynamics of two roof spoiler variants: a baseline known to cause stability issues and an improved design that resolved them. The performance in terms of time-averaged and unsteady aerodynamics is compared between the spoilers. It is shown that in crosswinds, the baseline spoiler, contrary to the improved spoiler, has bi-stable wake dynamics that induce lift force fluctuations at frequencies close to the 1^{st} natural frequency of the rear suspension. The vortex structure at the windward side of the slanted rear windscreen is shown to influence the wake dynamics strongly. A vehicle dynamic model was used to analyse the unsteady aerodynamic effects on vehicle handling.

7.4 Paper D

Wake dynamics of passenger vehicles and its influence on high speed stability

This paper uses the findings of Paper C to explore alternative design solutions that can break the bi-stable wake dynamics and solve the stability issues. Three diffuser designs and three side spoiler designs are investigated together with the baseline spoiler. The wake balance altered by the diffusers could not limit the large low-frequency rear lift fluctuations, since the windward side vortex structures were still present at the rear windscreen. Similarly, the straight side spoiler exhibited lift fluctuations, and the in-washed side spoiler further increased the vertical wake dynamics by feeding the windward side vortex structure. Interestingly, the out-washed side spoiler stabilised the wake by counteracting the windward side vortex structure. The improvements in high speed driving stability performance were confirmed on the test track. The paper also includes wind tunnel measurements showing the bi-stable vertical wake dynamics of the baseline spoiler and further extends the wake dynamic analysis.

7.5 Paper E

Drivers' perceived sensitivity to crosswinds and to low-frequency aerodynamic lift fluctuations

This paper contains two driving simulator studies on crosswind gust sensitivity and high speed stability. The crosswind sensitivity study included 38 drivers, subjectively evaluating the stability when the vehicle was subjected to gust varying in strength from 1 to 13 m/s, driving at 120, 160 and 200 km/h. It was found that the subjective assessment correlates with the sensory motion response of the vehicle (lateral acceleration and yaw velocity) and with vehicle path curvature (visual feedback). In addition, the latter was shown to be a speed-independent measure. The high speed stability study, with the inclusion of the unsteady wake dynamics, showed that three blind-tested professional drivers could differentiate vehicle configurations in agreement with their on-road subjective ratings. Furthermore, the results highlight the importance of both considering the time-averaged lift forces and the wake dynamics to improve the stability performance.

References

[1] Brandt, A., Sebben, S., Jacobson, B., Preihs, E., and Johansson, I. "Quantitative High Speed Stability Assessment of a Sports Utility Vehicle and Classification of Wind Gust Profiles". *SAE Technical Paper Series*. 2020. DOI: 10.4271/2020-01-0677.

[2] Brandt, A., Jacobson, B., and Sebben, S. "High speed driving stability of road vehicles under crosswinds: an aerodynamic and vehicle dynamic parametric sensitivity analysis". *Vehicle System Dynamics* **60**.7 (2021), 1–24. DOI: 10.1080/00423114.2021.1903516.

[3] Brandt, A., Sebben, S., and Jacobson, B. "Base wake dynamics and its influence on driving stability of passenger vehicles in crosswind". *Journal of Wind Engineering and Industrial Aerodynamics* **230** (2022). DOI: 10.1016/j.jweia.2022.105164.

[4] Brandt, A., Sebben, S., and Jacobson, B. "Wake dynamics of passenger vehicles and its influence on high speed stability". *Submitted for Publication* (2023).

[5] Brandt, A., Jacobson, B., and Sebben, S. "Drivers' perceived sensitivity to crosswinds and to low-frequency aerodynamic lift fluctuations". *Accepted for SAE WCX Conference*. 2023.

[6] Brandt, A. "Driving stability of passenger vehicles under crosswinds". Licentiate thesis. Chalmers University of Technology, 2021.

[7] "Vehicle Aerodynamics Terminology". SAE J1594 JUL2010.

[8] "Road vehicles – Vehicle dynamics and road-holding ability – Vocabulary". ISO 8855:2011.

[9] Baker, C. J. and Reynolds, S. "Wind-induced accidents of road vehicles". *Accident Analysis & Prevention* **24**.6 (1992), 559–575. DOI: 10.1016/0001-4575(92)90009-8.

[10] Sims-Williams, D. "Cross Winds and Transients: Reality, Simulation and Effects". *SAE International Journal of Passenger Cars - Mechanical Systems* **4**.1 (2011), 172–183. DOI: 10.4271/2011-01-0172.

[11] Wordley, S. and Saunders, J. W. "On-road Turbulence". *SAE Int. J. Passeng. Cars – Mech. Syst.* **1**.1 (2008), 341–360. DOI: https://doi.org/10.4271/2008-01-0475.

[12] Wordley, S. and Saunders, J. W. "On-road Turbulence: Part 2". *SAE International Journal of Passenger Cars - Mechanical Systems* **2**.1 (2009), 111–137. DOI: 10.4271/2009-01-0002.

[13] Watkins, S. and Cooper, K. R. "The Unsteady Wind Environment of Road Vehicles, Part Two: Effects on Vehicle Development and Simulation of Turbulence". *SAE Technical Paper Series*. 2007. DOI: 10.4271/2007-01-1237.

[14] Cooper, K. R. and Watkins, S. "The Unsteady Wind Environment of Road Vehicles, Part One: A Review of the On-road Turbulent Wind Environment". *SAE Technical Paper Series*. 2007. DOI: 10.4271/2007-01-1236.

[15] Jessing, C., Wilhelmi, H., Wittmeier, F., Wagner, A., Wiedemann, J., and Dillmann, A. "Investigation of Transient Aerodynamic Effects on Public Roads in Comparison to Individual Driving Situations on a Test Site". *SAE Technical Paper Series*. 2020. DOI: 10.4271/2020-01-0670.

[16] Wilhelmi, H., Jessing, C., Bell, J., Heine, D., Wagner, A., Wiedemann, J., and Wagner, C. "Simulation of Transient On-Road Conditions in a Closed Test Section Wind Tunnel Using a Wing System with Active Flaps". *SAE Technical Paper Series*. 2020. DOI: 10.4271/2020-01-0688.

[17] Fei, X., Kuthada, T., Wagner, A., and Wiedemann, J. "The Effect of Unsteady Incident Flow on Drag Measurements for Different Vehicle Geometries in an Open Jet Wind Tunnel". *SAE Technical Paper Series*. 2022. DOI: 10.4271/2022-01-0894.

[18] MacAdam, C. C., Sayers, M. W., Pointer, J. D., and Gleason, M. "Crosswind Sensitivity of Passenger Cars and the Influence of Chassis and Aerodynamic Properties on Driver Preferences". *Vehicle System Dynamics* **19**.4 (1990), 201–236. DOI: 10.1080/00423119008968942.

[19] Fukagawa, T., Shimokawa, S., Itakura, E., Nakatani, H., and Kitahama, K. "Modeling of Transient Aerodynamic Forces based on Crosswind Test". *SAE Int. J. Passeng. Cars - Mech. Syst.* **9**.2 (2016), 572–582. DOI: https://doi.org/10.4271/2016-01-1577.

[20] Nakasato, K., Tsubokura, M., Ikeda, J., Onishi, K., Ota, S., Takase, H., Akasaka, K., Ihara, H., Oshima, M., and Araki, T. "Coupled 6DoF Motion and Aerodynamic Crosswind Simulation Incorporating Driver Model". *SAE Int. J. Passeng. Cars - Mech. Syst.* **10**.2 (2017), 662–670. DOI: https://doi.org/10.4271/2017-01-1525.

[21] Lewington, N., Ohra-aho, L., Lange, O., and Rudnik, K. "The Application of a One-Way Coupled Aerodynamic and Multi-Body Dynamics Simulation Process to Predict Vehicle Response during a Severe Crosswind Event". *SAE Technical Paper Series*. SAE International, 2017. DOI: https://doi.org/10.4271/2017-01-1515.

[22] Bell, J. R., Wilhelmi, H., Heine, D., Jessing, C., Wagner, A., Wiedemann, J., and Wagner, C. "Aerodynamic Characterization of a Full-Scale Compact Car Exposed to Transient Crosswind". *SAE International Journal of Passenger Cars - Mechanical Systems* **14**.1 (2021). DOI: 10.4271/06-14-01-0001.

[23] "Road vehicles – Sensitivity to lateral wind – Open-loop test method using wind generator input". ISO 12021:2010.

[24] Forbes, D. C., Page, G. J., Passmore, M. A., and Gaylard, A. P. "A Fully Coupled, 6 Degree-of-Freedom, Aerodynamic and Vehicle Handling Crosswind Simulation using the DrivAer Model". *SAE International Journal of Passenger Cars - Mechanical Systems* **9**.2 (2016). DOI: 10.4271/2016-01-1601.

[25] Carbonne, L., Winkler, N., and Efraimsson, G. "Use of Full Coupling of Aerodynamics and Vehicle Dynamics for Numerical Simulation of the Crosswind Stability of Ground Vehicles". *SAE International Journal of Commercial Vehicles* **9**.2 (2016), 359–370. DOI: 10.4271/2016-01-8148.

[26] Li, S. Y., Gu, Z. Q., Huang, T. M., Chen, Z., and Liu, J. "Coupled analysis of vehicle stability in crosswind on low adhesion road". *International Journal of Numerical Methods for Heat & Fluid Flow* **28**.8 (2018), 1956–1972. DOI: 10.1108/hff-01-2018-0013.

[27] Huang, T., Li, S., Wan, Z., and Gu, Z. "Investigation of vehicle stability under crosswind conditions based on coupling methods". *Proceedings of the Institution of Mechanical Engineers, Part D: Journal of Automobile Engineering* (2019). DOI: 10.1177/0954407018822424.

[28] Tunay, T., O'Reilly, C. J., and Drugge, L. "The Significance of Roll on the Dynamics of Ground Vehicles Subjected to Crosswind Gusts by Two-Way Coupled Simulation of Aero- and Vehicle Dynamics". *Advances in Dynamics of Vehicles on Roads and Tracks*. Lecture Notes in Mechanical Engineering. 2020, pp. 1388–1397. DOI: 10.1007/978-3-030-38077-9_160.

[29] Wojciak, J. "Quantitative Analysis of Vehicle Aerodynamics during Crosswind Gusts". PhD thesis. Technical University of Munich, 2012.

[30] Theissen, P. "Unsteady Vehicle Aerodynamics in Gusty Crosswind". PhD thesis. Technical University of Munich, 2012.

[31] Onishi, Y., Ogawa, K., Sawada, J., Suwa, Y., and Nucera, F. "On Road Fuel Economy Impact by the Aerodynamic Specifications under the Natural Wind". *SAE Technical Paper Series*. 2020. DOI: 10.4271/2020-01-0678.

[32] Lawson, A. A., Sims-Williams, D. B., and Dominy, R. G. "Effects of On-Road Turbulence on Vehicle Surface Pressures in the A-Pillar Region". *SAE International Journal of Passenger Cars - Mechanical Systems* **1**.1 (2008), 333–340. DOI: 10.4271/2008-01-0474.

[33] Hucho, W.-H. "Aerodynamics of Road Vehicles". Fourth edition. SAE International, 1998.

[34] Barth, R. "Effect of Unsymmetrical Wind Incidence on Aerodynamic Forces Acting on Vehicle Models and Similar Bodies". SAE International, 1965. DOI: https://doi.org/10.4271/650136.

[35] Favre, T., Näfver, J. J., Jerrelind, J., Trigell, A. S., and Efraimsson, G. "Static coupling between detached-eddy simulations and vehicle dynamic simulations of a generic road vehicle model with different rear configurations in unsteady crosswind". *International Journal of Vehicle Design* **72**.4 (2016). DOI: 10.1504/ijvd.2016.082384.

[36] Pacejka, H. "Tire and Vehicle Dynamics". 2012. ISBN: 9780080970165. DOI: 10.1016/c2010-0-68548-8.

[37] Milliken, W. F., Dell'Amico, F., and Rice, R. S. "The Static Directional Stability and Control of the Automobile". *SAE Technical Paper Series*. 1976. DOI: 10.4271/760712.

[38] Buchheim, R., Maretzke, J., and Piatek, R. "The Control of Aerodynamic Parameters Influencing Vehicle Dynamics". *SAE Paper* (1985), 850279–850279. DOI: 10.4271/850279.

[39] Howell, J. and Le Good, G. "The Influence of Aerodynamic Lift on High Speed Stability". *SAE Technical Paper SeriesTechnial* **01**.0651 (1999), 8–8. DOI: 10.4271/1999-01-0651.

[40] Windsor, S. and Le Good, G. "The Influence of Aerodynamic Lift on High Speed Stability". *Autotech 93*. Vol. 01. 1993, pp. 8–8.

[41] Oraby, W. A. H. and Crolla, D. A. "Passenger Car Stability Under Random Wind Excitation". *SAE Technical Paper Series*. SAE International, 2001. DOI: https://doi.org/10.4271/2001-01-0133.

[42] Juhlin, M. and Eriksson, P. "A Vehicle Parameter Study on Crosswind Sensitivity of Buses". *SAE Technical Paper Series*. 2004. DOI: 10.4271/2004-01-2612.

[43] Howell, J. and Panigrahi, S. "Aerodynamic Side Forces on Passenger Cars at Yaw". *SAE Technical Paper Series*. 2016. DOI: 10.4271/2016-01-1620.

[44] Chadwick, A., Garry, K., and Howell, J. "Transient Aerodynamic Characteristics of Simple Vehicle Shapes by the Measurement of Surface Pressures". *SAE Technical Paper Series* (2000). DOI: https://doi.org/10.4271/2000-01-0876.

[45] Davenport, A. G. "THE APPLICATION OF STATISTICAL CONCEPTS TO THE WIND LOADING OF STRUCTURES". *Proceedings of the Institution of Civil Engineers* (1961).

[46] Schroeck, D., Krantz, W., Widdecke, N., and Wiedemann, J. "Unsteady Aerodynamic Properties of a Vehicle Model and their Effect on Driver and Vehicle under Side Wind Conditions". *SAE Int. J. Passeng. Cars – Mech. Syst.* **4**.1 (2011), 108–119. DOI: https://doi.org/10.4271/2011-01-0154.

[47] Stoll, D. and Wiedemann, J. "Active Crosswind Generation and Its Effect on the Unsteady Aerodynamic Vehicle Properties Determined in an Open Jet Wind Tunnel". SAE International, 2018. DOI: https://doi.org/10.4271/2018-01-0722.

[48] Fuller, J. B. and Passmore, M. "Unsteady Aerodynamics of an Oscillating Fastback Model". *SAE International Journal of Passenger Cars - Mechanical Systems* **6**.1 (2013), 403–413.

[49] Oettle, N., Mankowski, O., Sims-Williams, D., Dominy, R., Freeman, C., and Gaylard, A. "Assessment of a Vehicle's Transient Aerodynamic Response". *SAE Technical Paper Series*. 2012. DOI: 10.4271/2012-01-0449.

[50] Okada, Y., Nouzawa, T., Nakamura, T., and Okamoto, S. "Flow Structures above the Trunk Deck of Sedan-Type Vehicles and Their Influence on High-Speed Vehicle Stability 1st Report: On-Road and Wind-Tunnel Studies on Unsteady Flow Characteristics that Stabilize Vehicle Behavior". *SAE International Journal of Passenger Cars - Mechanical Systems* **2**.1 (2009), 138–156. DOI: 10.4271/2009-01-0004.

[51] Nakashima, T., Tsubokura, M., Nouzawa, T., Nakamura, T., and Ichimiya, M. "Flow Structures above the Trunk Deck of Sedan-Type Vehicles and Their Influence on High-Speed Vehicle Stability 2nd Report: Numerical Investigation on Simplified Vehicle Models using Large-Eddy Simulation". *SAE International Journal of Passenger Cars - Mechanical Systems* **2**.1 (2009), 157–167. DOI: 10.4271/2009-01-0006.

[52] Cheng, S. Y., Tsubokura, M., Nakashima, T., Okada, Y., and Nouzawa, T. "Numerical quantification of aerodynamic damping on pitching of vehicle-inspired bluff body". *Journal of Fluids and Structures* **30** (2012), 188–204. DOI: 10.1016/j.jfluidstructs.2012.01.002.

[53] Cheng, S. Y., Tsubokura, M., Okada, Y., Nouzawa, T., Nakashima, T., and Doh, D. H. "Aerodynamic stability of road vehicles in dynamic pitching motion". *Journal of Wind Engineering and Industrial Aerodynamics* **122** (2013), 146–156. DOI: 10.1016/j.jweia.2013.06.010.

[54] Kawakami, M., Murata, O., and Maeda, K. "Improvement in Vehicle Motion Performance by Suppression of Aerodynamic Load Fluctuations". *SAE International Journal of Passenger Cars - Mechanical Systems* **8**.1 (2015), 205–216. DOI: 10.4271/2015-01-1537.

[55] Matsumoto, D., Nakae, Y., Niedermeier, C., Tanaka, H., and Indinger, T. "Application of Dynamic Mode Decomposition to Influence the Driving Stability of Road Vehicles". *SAE Technical Paper Series*. 2019. DOI: 10.4271/2019-01-0653.

[56] Urquhart, M., Varney, M., Sebben, S., and Passmore, M. "Aerodynamic drag improvements on a square-back vehicle at yaw using a tapered cavity and asymmetric flaps". *International Journal of Heat and Fluid Flow* **86** (2020). DOI: 10.1016/j.ijheatfluidflow.2020.108737.

[57] Grandemange, M., Gohlke, M., and Cadot, O. "Bi-stability in the turbulent wake past parallelepiped bodies with various aspect ratios and wall effects". *Physics of Fluids* **25**.9 (2013). DOI: 10.1063/1.4820372.

[58] Grandemange, M., Cadot, O., Courbois, A., Herbert, V., Ricot, D., Ruiz, T., and Vigneron, R. "A study of wake effects on the drag of Ahmed's squareback model at the industrial scale". *Journal of Wind Engineering and Industrial Aerodynamics* **145** (2015), 282–291. DOI: 10.1016/j.jweia.2015.03.004.

[59] Bonnavion, G., Cadot, O., Herbert, V., Parpais, S., Vigneron, R., and Délery, J. "Asymmetry and global instability of real minivans' wake". *Journal of Wind Engineering and Industrial Aerodynamics* **184** (2019), 77–89. DOI: 10.1016/j.jweia.2018.11.006.

[60] Perry, A.-K., Pavia, G., and Passmore, M. "Influence of short rear end tapers on the wake of a simplified square-back vehicle: wake topology and rear drag". *Experiments in Fluids* **57**.11 (2016). DOI: 10.1007/s00348-016-2260-3.

[61] He, K., Minelli, G., Su, X., Gao, G., and Krajnović, S. "On state instability of the bi-stable flow past a notchback bluff body". *Journal of Fluid Mechanics* **931** (2022). DOI: 10.1017/jfm.2021.1025.

[62] Meile, W., Ladinek, T., Brenn, G., Reppenhagen, A., and Fuchs, A. "Non-symmetric bi-stable flow around the Ahmed body". *International Journal of Heat and Fluid Flow* **57** (2016), 34–47. DOI: 10.1016/j.ijheatfluidflow.2015.11.002.

[63] Rao, A., Minelli, G., Basara, B., and Krajnović, S. "On the two flow states in the wake of a hatchback Ahmed body". *Journal of Wind Engineering and Industrial Aerodynamics* **173** (2018), 262–278. DOI: 10.1016/j.jweia.2017.10.021.

[64] Cheng, S.-Y., Chin, K.-Y., Mansor, S., and Abd Rahman, A. B. "Experimental study of yaw angle effect on the aerodynamic characteristics of a road vehicle fitted with a rear spoiler". *Journal of Wind Engineering and Industrial Aerodynamics* **184** (2019), 305–312. DOI: 10.1016/j.jweia.2018.11.033.

[65] Bonnavion, G., Cadot, O., Évrard, A., Herbert, V., Parpais, S., Vigneron, R., and Délery, J. "On multistabilities of real car's wake". *Journal of Wind Engineering and Industrial Aerodynamics* **164** (2017), 22–33. DOI: 10.1016/j.jweia.2017.02.004.

[66] Cadot, O., Courbois, A., Ricot, D., Ruiz, T., Harambat, F., Herbert, V., Vigneron, R., and Délery, J. "Characterisations of force and pressure fluctuations of real vehicles". *International Journal of Engineering Systems Modelling and Simulation* **8**.2 (2016). DOI: 10.1504/ijesms.2016.075529.

[67] Wagner, A. and Wiedemann, J. "Crosswind Behavior in the Driver 's Perspective". *SAE Technical Paper Series* 724 (2002). DOI: 10.4271/2002-01-0086.

[68] Krantz, W. "An Advanced Approach for Predicting and Assessing the Driver's Response to Natural Crosswind". PhD thesis. University of Stuttgart, 2012.

[69] Song, J., Yoshioka, S., Kato, T., and Kohama, Y. "Characteristics of Flow Behind a Passenger Vehicle". *SAE Technical Paper Series*. 2006. DOI: 10.4271/2006-01-1030.

[70] Willumeit, H. P., Müller, K., Dödlbacher, G., and Matheis, A. "Method to Correlate Vehicular Behaviour and Driver's Judgement under Side Wind Disturbances". *Vehicle System Dynamics* **17** (1988), 508–524. DOI: 10.1080/00423118808969292.

[71] Kumar, A., Sebben, S., Sällström, E., Jacobson, B. J. H., and Broniewicz, A. "Analysis of Subjective Qualitative Judgement of Passenger Vehicle High Speed Drivability due to Aerodynamics". *Energies* **12**.14 (2019). DOI: 10.3390/en12142839.

[72] Nguyen, M.-T., Pitz, J., Krantz, W., Neubeck, J., and Wiedemann, J. "Subjective Perception and Evaluation of Driving Dynamics in the Virtual Test Drive". *SAE International Journal of Vehicle Dynamics, Stability, and NVH* **1**.2 (2017), 247–252. DOI: 10.4271/2017-01-1564.

[73] Kumar, A. "Subjective perception and prediction model of vehicle stability under aerodynamic excitations". Licentiate thesis. Chalmers University of Technology, 2021.

[74] Huemer, J., Stickel, T., Sagan, E., Schwarz, M., and Wall, W. A. "Influence of unsteady aerodynamics on driving dynamics of passenger cars". *Vehicle System Dynamics* **52**.11 (2014), 1470–1488. DOI: 10.1080/00423114.2014.944191.

[75] Menter, F. "Stress-Blended Eddy Simulation (SBES)—A New Paradigm in Hybrid RANS-LES Modeling". *Progress in Hybrid RANS-LES Modelling*. Notes on Numerical Fluid Mechanics and Multidisciplinary Design. Springer International Publishing, 2018. Chap. Chapter 3, pp. 27–37. ISBN: 978-3-319-70031-1. DOI: 10.1007/978-3-319-70031-1_3.

[76] Germano, M., Piomelli, U., Moin, P., and Cabot, W. H. "A dynamic subgrid-scale eddy viscosity model". *Physics of Fluids A: Fluid Dynamics* **3**.7 (1991), 1760–1765. DOI: 10.1063/1.857955.

[77] Ekman, P., Larsson, T., Virdung, T., and Karlsson, M. "Accuracy and Speed for Scale-Resolving Simulations of the DrivAer Reference Model". *SAE Technical Paper Series*. 2019. DOI: 10.4271/2019-01-0639.

[78] Davidson, L. "Large Eddy Simulations: How to evaluate resolution". *International Journal of Heat and Fluid Flow* **30**.5 (2009), 1016–1025. DOI: 10.1016/j.ijheatfluidflow.2009.06.006.

[79] Favre, T. and Efraimsson, G. "An Assessment of Detached-Eddy Simulations of Unsteady Crosswind Aerodynamics of Road Vehicles". *Flow, Turbulence and Combustion* **87**.1 (2011), 133–163. DOI: 10.1007/s10494-011-9333-4.

[80] Kuiper, E. and Van Oosten, J. J. M. "The PAC2002 advanced handling tire model". *Vehicle System Dynamics* **45** (2007), 153–167. DOI: 10.1080/00423110701773893.

[81] VI-grade GmbH. "DiM 250 technical manual no. GS-H-23269a". Catalog. 2018.

[82] Aeroprobe Corporation. "Standard Probe User Manual, Document No. 90001-02-UMN-02". Catalog. 2015.

[83] Schuetz, T. "Aerodynamics of Road Vehicles". Fifth Edition. 2015. ISBN: 978-0-7680-7977-7. DOI: 10.4271/r-430.

[84] Dewesoft GmbH. "DS-IMU/Gyro User Manual". Catalog. 2013.

[85] "Hällered Test track, Sweden - Aerial Shot". Web Page. Accessed: 2020-12-15. URL: https://www.media.volvocars.com/global/en-gb/media/photos/35609.

[86] Sternéus, J., Walker, T., and Bender, T. "Upgrade of the Volvo Cars Aerodynamic Wind Tunnel". *SAE International* **01**.1043 (2007). DOI: 10.4271/2007-01-1043.

[87] Ljungskog, E. "Evaluation and modeling of the flow in a slotted wall wind tunnel". PhD thesis. Chalmers University of Technology, 2019.